

**Understanding the Impact of Post Heat Treatments on the Mechanism of Annealing Twin
Formation in 316L Stainless Steel 3D Printed Components**

by

Yu Zhou

B.S., Department of Materials Science and Engineering, East China University of Science and
Technology, 2011

M.S., Department of Materials Science and Engineering, University of Pittsburgh, 2014

Submitted to the Graduate Faculty of
Swanson School of Engineering in partial fulfillment
of the requirements for the degree of
Doctor of Philosophy

University of Pittsburgh

2020

UNIVERSITY OF PITTSBURGH
SWANSON SCHOOL OF ENGINEERING

This dissertation was presented

by

Yu Zhou

It was defended on

July 24, 2020

and approved by

Qing-Ming Wang, Ph.D., Professor, Department of Mechanical Engineering and Materials
Science

Scott Mao, Ph.D., Professor, Department of Mechanical Engineering and Materials Science

Sung Kwon Cho, Ph.D., Professor, Department of Mechanical Engineering and Materials
Science

Susheng Tan, Ph.D., Associate Professor, Department of Electrical and Computer Engineering

Dissertation Director: C. Isaac Garcia, Ph.D., Professor, Department of Mechanical Engineering
and Materials Science

Copyright © by Yu Zhou

2020

Understanding the Impact of Post Heat Treatments on the Mechanism of Annealing Twin Formation in 316L Stainless Steel 3D Printed Components

Yu Zhou, PhD

University of Pittsburgh, 2020

The fabrication of 316L stainless steel via selective laser melting (SLM) has been developed in the past decade due to the convenience of the complex geometry design, faster manufacturing times and fine microstructure. However, several problems such as porosity, residual internal stresses and anisotropic properties, make it necessary to heat treat the components to modify their microstructure and improve their performance. This post heat treatment leads to the loss of the initial fine microstructure and hence the high strength.

The goal of this dissertation is to provide an alternative approach for the post heat treatments of SLM fabricated 316L stainless steel. One of these approaches is the use of high energy systems, i.e. induction rapid heating. The application of fast heating rate is expected to promote the formation of annealing twin boundaries, which is a strengthening mechanism of this face centered cubic (FCC) materials. 316L stainless steel fabricated via SLM process using gas atomized powders was used as the base material in this study. A continuous induction heating laboratory simulator (CAL-30KW) was used to provide various heating rates during the post heat treatments. The microstructure of both as-fabricated specimens and post heat-treated specimens was characterized. Of particular interest in this study was to examine the role of rapid heating on the formation of annealing twin boundaries (coherent and incoherent) formation and the area density evolution. The influence of processing parameters, such as reheating temperature, heating rate and holding time, on the annealing twin density were investigated. The resulting

microstructures were analyzed using Optical Microscopy (OM), Scanning Electron Microscopy (SEM), Electron Back-scattered Diffraction (EBSD), and Transmission Electron Microscopy (TEM). The formation of twin boundaries during recrystallization was assessed. The mechanism of annealing twin boundaries formation of SLM fabricated SS316L during induction rapid heating is a combination of growth accident and grain boundary dissociation. The results are presented and discussed in this dissertation.

Keywords: Rapid heating, Additive manufacturing, Selective laser melting, Annealing twin boundaries.

Table of Contents

Acknowledgements.....	xiv
1.0 Introduction.....	1
1.1 Problem Statement.....	1
1.2 Hypothesis	3
1.3 Objectives	4
2.0 Background	5
2.1 Metallic Additive Manufacturing (AM) Technologies	5
2.1.1 General Description	5
2.1.2 Powder Material Fabrication.....	6
2.1.3 Brief Overview of BJ Process.....	8
2.1.4 Brief Overview of SLM Process.....	10
2.2 Annealing twin boundary.....	17
2.2.1 General Description of Grain Boundaries.....	17
2.2.2 Annealing Twins in FCC Crystallographic Structure	20
2.2.3 Annealing twin formation theories	22
2.2.4 Effect of Chemical Composition on Annealing Twins	25
3.0 Experimental Procedure	27
3.1 Material Selection and Processing	27
3.2 Microstructural Characterization on OM and SEM	29
3.2.1 Sample Preparation.....	29
3.2.2 Microstructural Observation.....	29

3.2.3 EBSD-OIM Analysis	30
3.3 TEM Analysis	32
3.4 Microhardness Measurements.....	33
4.0 Results.....	34
4.1 General Observation of Microstructure.....	34
4.1.1 Microstructure of As Fabricated Sample	34
4.1.2 Microstructure of Heat Treated Samples.....	35
4.1.3 Summary	45
4.2 Annealing Twin Density Characterization.....	46
4.2.1 Annealing Twin Density Comparison at 1150°C.....	47
4.2.2 Summary	64
4.3 Grain Size Measurements	65
4.4 Microhardness Measurements.....	67
4.4.1 Summary	72
4.5 Result Summary of Best Processing Conditions	72
5.0 Discussions.....	74
5.1 Annealing Twin Formation in Induction Rapid Heating.....	74
5.1.1 Annealing Twin Formation Mechanisms	74
5.1.2 Comparison with Classical Models.....	84
5.1.3 Summary	91
5.2 The Recrystallization Kinetics Analysis	92
5.2.1 Recrystallization Kinetics at Different Processing Conditions	93
5.2.2 Summary	98

5.3 The Effect of Heating Rate.....	98
5.3.1 The Principle of Induction Heating	99
5.3.2 Analysis of Local Thermal Stresses during Rapid Induction Heating	101
5.3.3 Summary	106
5.4 Verification of Hypothesis.....	107
6.0 Conclusions.....	110
7.0 Future Works	113
Bibliography.....	114

List of Tables

Table 1. List of anisotropic tensile properties via SLM process.....	15
Table 2. Chemical composition of gas atomized powder for SLM process.....	27
Table 3. Summary of high annealing twin density processing conditions.....	65
Table 4. VHN value of specimens heat treated at 1150°C	68
Table 5. VHN values of samples heat treated at 1200°C	70
Table 6. VHN values of samples heat treated at 1250°C	71
Table 7. Comparison of grain size and microhardness values between processing conditions with high annealing twin density	73
Table 8. The n values of best processing conditions in chapter 4	98

List of Figures

Figure 1. SEM images showing the morphology of (a) gas atomized powder, and (b) water atomized powder[6].....	8
Figure 2. Schematic of BJ process, figure reproduced from [11].....	9
Figure 3. Schemaitc of SLM Process, figure reproduced from [19].....	11
Figure 4 Microstructure of as-fabricated stainless steel 316L via SLM[35].....	13
Figure 5. 2D appearance of twin boundaries	17
Figure 6. Curve of grain boundary energy versus misorientation angle[53]	19
Figure 7. Schematic of the laboratory induction heating system	28
Figure 8. A schematic of EBSD acquisition inside SEM.....	31
Figure 9. OM images of as-fabricated SLM SS316L at different magnifications.....	34
Figure 10. SEM images of as-fabricatd SS316L samples at various magnifications	35
Figure 11. OM images of SLM SS316L samples heat treated at 1150°C with rapid heating at 200°C/s and held for (a) 12min, (b) 24min, (c) 36min, (d) 48min, (e) 60min; and with furnace heating (~0.1°C/s) and held for (f) 12min, (g) 24min, (h) 36min, (i) 48min, (j) 60min	37
Figure 12. SEM images of SLM SS316L samples heat treated at 1150°C with rapid heating at 200°C/s and 0.1°C/s for 12-60min.....	39
Figure 13. OM images of SLM SS316L samples heat treated at 1150°C and held for 12 min at various heating rates	40

Figure 14. TEM image of SLM SS316L as-fabricatd samples and heat treated samples at 1150°C with 200°C/s holding from 3-12min.....42

Figure 15. OM images of SLM SS316L samples heat treated at 1200°C and 1250°C and held for 12 min at various heating rates44

Figure 16. Relationship between grain size and heating rate for SLM SS316L samples heat treated at different temperatures holding for 12min45

Figure 17. IPF and IQ + Twin boundary results from 500*500µm EBSD scans of 1150°C heat treated samples from 12-60min at slow and fast heating rates.....48

Figure 18. Length twin density vs. holding time at 1150°C49

Figure 19. IQ + GOS + Twin boundary at 1150°C52

Figure 20. GOS < 2° fraction vs. holding time at 1150°C53

Figure 21. Comparison of heating rates at 1150°C holding for 12min using induction rapid heating54

Figure 22. Annealing twin density at different heating rates at 1150°C holding for 12min.54

Figure 23. IPFs of samples heat treated at 1200°C with various heating rates and holding times.....56

Figure 24. IQ + Twin boundaries of samples heat treated at 1200°C with various heating rates and holding times57

Figure 25. GOS + IQ + Twin boundaries of samples heat treated at 1200°C with various heating rates and holding times58

Figure 26. Coherent and incoherent twin density vs. holding time at various heating rates at 1200°C.....59

Figure 27. Recrystallization percentage vs. holding time at various heating rates at 1200°C	60
.....	
Figure 28. IPFs of samples heat treated at 1250°C with various heating rates.....	61
Figure 29. IQ + Twin boundaries of samples heat treated at 1250°C with various heating rates.....	62
Figure 30. GOS + IQ + Twin boundary of samples heat treated at 1250°C with various heating rates	63
Figure 31. Coherent and incoherent twin density vs. holding time at 1250°C with various heating rates	63
Figure 32. GOS < 2° fraction vs. holding time at 1250°C with various heating rates.....	64
Figure 33. Grain size vs. holding time at various temperatures and heating rates.....	67
Figure 34. Microhardness and standard deviation of samples heat treated at 1150°C	69
Figure 35. Microhardness and standard deviation of samples heat treated at 1200°C	70
Figure 36. Microhardness and standard deviation of samples heat treated at 1250°C	71
Figure 37. The relationship between recrystallization fraction and twin density at 1150°C, 200°C/s heating rate.....	76
Figure 38. GOS distribution for samples heat treated at 200°C/s at 1150°C for 6, 12, 24 and 48min	76
Figure 39. Annealing twin density and length fractions of LAGBs and HAGBs vs. holding time for 200°C/s rapid heating at 1150°C.....	77
Figure 40. GND density distribution map with highlighted twin boundaries for samples heat treated at 200°C/s at 1150°C holding from 3-12min	79

Figure 41. GND density distribution map with highlighted annealing twin boundaries at 200°C/s rapid heating at 1150°C holding for 24-48min	81
Figure 42. Illustration of grain boundary dissociation model, the thickness of each boundary represents its interfacial energy. Figure reproduced from Meyers' research[72]	81
Figure 43. TEM images showing the change of microstructure of as-fabricated samples and samples heated at 200°C/s rapid heating at 1150°C	83
Figure 44. Scatter points of the logarithm of converted coherent twin density and grain size compared with Gleiter's model.....	86
Figure 45. Relationship between coherent twin density and grain size in induction rapid heating	88
Figure 46. Curve fitting to Pande's model at different temperatures: (a)1150°C, (b)1200°C, (c)1250°C	90
Figure 47. Relationship between recrystallization fraction and twin density of experimental data at all temperatures and heating rates in induction rapid heating	91
Figure 48. JMAK recrystallization kinetics analysis for samples heat treated at 1150°C....	94
Figure 49. JMAK recrystallization kinetics analysis for samples heat treated at 1200°C....	95
Figure 50. JMAK recrystallization kinetics analysis for samples heat treated at 1250°C....	96
Figure 51. Relationship between twin density increase and recrystallization rate (n value)	97

Acknowledgements

First of all, I would like to thank my advisor, Dr. C. Isaac Garcia, for his support and guidance during my graduate studies. Dr. Garcia kept giving me challenging works and useful suggestions during my study, and this made me go straight beyond my limits. I learned how to keep a broader view while conducting a project and how to catch the important points while solving a real problem. It's my honor and pleasure to be your student and work under your supervision.

I would also like to thank my entire committee members, Dr. Qingming Wang, Dr. Scott Mao, Dr. Susheng Tan, and Dr. Sung Kwon Cho, for spending their time to review and giving feedbacks of my dissertation.

I would like to thank Dr. Chris Schade in Hoeganaes Corporation for providing the SLM fabricated materials and necessary data for this research.

I would like to acknowledge my colleagues, Gregorio Solis, Tiffany Juan, Rafael Landa, Zhanfang Wu, Luis Felliipe, Pedro Ciacco and Yuankang Wang, for their helps in my research. Most times we worked in different projects, fields and materials, and our cross-linked discussions could always bring me new ideas and improve my understandings. I also want to thank to all the staffs, students and visiting scholars who have been working in our group.

Especially thank to Dr. Bo Jiang, who was a visiting scholar in our group for 6 months. He is kind-hearted and has rich experience in metallurgy and steel alloys. He was my roommate during he stayed in Pittsburgh. We worked together from morning to evening, and sometimes midnight if necessary. We did body recreation and sports together. He provided lots of suggestions on my research and paper writing, and we also overcame several troubles in our daily life. He was not only a good colleague in research, but also a good friend after work.

I want to thank all the faculty members, staffs and students in MEMS department, machine shop and NCF for advice and support in my PhD career, including trainings to learn a new equipment, administrative registration and financial issues, useful comments in their research fields which I was not familiar with. Thank you!

I want to thank my landlords, current and previous roommates for their patience and helps on various problems in my life. I stayed in the same address ever since I arrived Pittsburgh, because I felt happy and warm to live with them.

Finally, I would like to acknowledge my parents for their patience and support as well. I can discuss everything with them and get useful suggestions. I can release my pressure during our facetime interviews. I can always get their encouragements every time I feel upset. Thank you!

Yu Zhou

1.0 Introduction

Stainless steel 316L (SS316L) is widely applied to chemical, marine and biomedical fields due to its excellent ductility, corrosion and oxidation resistance. Recently, additive manufacturing (AM), also well-known as 3-D printing, has attracted much interest from industries as a new approach to fabricate SS316L components, as it provides a number of advantages such as energy cost reduction, faster manufacturing periods and complex geometry control. This new approach allows one to manufacture components from free digital 3-D model designs and build up the parts layer by layer. The use of AM techniques not only allows for component designs that use less materials and provide improved structural strength, but also can be used to process alloy chemistries difficult to or not typically produced in the wrought or cast form.

1.1 Problem Statement

AM technology has a great potential in fabricating parts with complicate geometry due to lower materials and energy cost and shorter producing period compared to traditional manufacturing. However, AM fabricated metallic components are also facing challenges in internal defects and anisotropic mechanical properties, which are introduced from its manufacturing processes. Porosity takes place during AM process since inherent pores would be trapped in between the powder particles due to lack of mechanical pressure, and these pores become weak points when the parts are under load, limiting their high strength performance. Anisotropic mechanical properties usually occur in high-energy based AM techniques, such as

selective laser melting (SLM) and laser engineered net shaping (LENS). The uniaxial heat source and cooling direction control the growth of microstructure into a certain direction, causing a variation of mechanical properties in different dimensions of the fabricated parts. Thus, to reduce the variability in performance of these parts, it is necessary to heat treat the components. The post-heat treatments modify their microstructure, and eliminate internal defects and hence reduce their anisotropy.

The microstructure of conventionally produced metallic components can be changed by the single or combined application of mechanical deformation and heat treatments. Changes in the microstructure of 3D fabricated metallic components, by deformation is difficult due to their complex geometry and not cost-effective. Therefore, heat treatment is usually the major way to achieve changes in the microstructure, lower the porosity and reduce residual stresses of AM fabricated metallic parts. However, the application of heat treatments often leads to a loss of strength due to changes in the ultrafine microstructure obtained from rapid melting and cooling during AM fabrication. The loss of strength is more critical in metallic systems where the strengthening mechanisms are limited to solid solution and grain size, such as 316L austenitic stainless steels. This grade of steel cannot be strengthened by phase transformation or precipitation during heat treatment and subsequent cooling. The strengthening mechanisms in 316L stainless steel are solid solution, fine grain and dislocation density.

Based on the current understanding and modifications to standard grades of austenitic stainless steels, i.e. 316L, increases in yield strength have been obtained by solid solution strengthening with nitrogen or by cold or warm deformations. A possible approach to increase the strength of heat treated 316L AM components is to produce special twin boundaries (incoherent and coherent twin boundaries). These twin boundaries can act as obstacles to dislocation motion.

Using this idea, it is considered that by using high energy heating it is possible to introduce high local stresses in the matrix of austenitic stainless steels. These local thermal stresses will be equivalent to small deformations, hence increasing local strengthening. It is expected that the introduction of thermal stresses would reduce the loss of strength by producing more twin boundaries (incoherent and coherent) which provide stronger obstacles to dislocation motion than line defects (i.e. dislocations) and point defects (i.e. solute atoms). A surface such as a boundary impedes the motion of a dislocation along its slip plane length. Another benefit of using fast heating, it reduces processing times. These ideas provide the goal of this study, which is to study the impact of applying high energy through rapid heating to SS316L AM parts to optimize the microstructure and mechanical properties. Of particular interest of this study is the formation and response of annealing twin boundaries during rapid heating treatments.

1.2 Hypothesis

In traditional manufacturing, deformation + post annealing is the most common way to form annealing twin boundaries in systems with low stacking fault energy. Austenitic stainless steels is one of this systems. The formation of annealing twin boundaries is a consequence of changes in the microstructure due to the overall reduction of energy of the system. It is hypothesized that rapid heating will form more twins since it increases the amount of the energy of the system and also induces local thermal stresses. More specifically, as the heating rate increases, the twin density will increase due to higher energy input and larger thermal stress. This is a consequence that heat conduction on austenitic stainless steels is not efficient. Therefore,

various heating rates at different temperatures will be applied to test this hypothesis. This hypothesis will be revisited during discussions of the results.

1.3 Objectives

The primary objective of this research is to understand the effect of rapid heating on the annealing twin boundary formation and distribution during post heat treatments of AM fabricated SS316L components. The secondary objective is to provide a processing map as a guidance of post heat treatment of AM fabricated components. More specifically, this research aims to answer several research questions: 1) at what point in the post heat treatment will the AM specimens be able to form annealing twin boundaries? 2) Is this mechanism similar as conventional polycrystalline recrystallization and grain growth behavior? 3) Is there any preference of the annealing twin boundary formation to some specific grain boundaries? 4) How will the annealing twin density be related to the processing parameters of the post heat treatment? To answer these questions, SS316L specimens fabricated through SLM process were used and studied. Various heating rates, heating temperatures and isothermal heating times were applied. Optical microscopy (OM) and scanning electron microscopy (SEM) has been used for the microstructural overview. Electron back-scattered diffraction orientation imaging microscopy (EBSD-OIM) has been applied for twin boundary identification and twin density measurements. Transmission electron microscopy (TEM) has been used to study the change of microstructure and the formation of twin boundaries. The results will be discussed in the following chapters.

2.0 Background

2.1 Metallic Additive Manufacturing (AM) Technologies

2.1.1 General Description

Additive manufacturing process, developed from rapid prototyping over three decades ago, was designed for non-structural components. AM process aims to build up three-dimensional components layer by layer with addition of materials following the geometry of pre-designed 3D digital models. This approach gives one the freedom of materials composition selection and complex geometry design, which is difficult to achieve through conventional manufacturing. Moreover, AM process gets rid of the need for special tools such as casting molds or dies with specific forms compared to conventional manufacturing due to its unique one-step fabrication directly from digital designs to final parts, and therefore leads to significant improvements in cost saving and capability in industrial applications. Consequently, metallurgical differences such as mechanical anisotropy, residual stress and internal defects (porosity) occur in AM products and these become critical challenges that needs to be overcome[1].

According to ASTM Standard F2792[2], metallic AM processes can be divided into the following categories: 1) Directed energy deposition, which focused thermal energy is applied to melt materials during deposition onto a substrate(such as laser engineered net-shaping (LENS) technology); 2) Binder jetting (BJ), which applies a liquid bonding agent to selected areas to join powder particles between the deposition of current layer and the next layer; and 3) Powder bed fusion, which thermal energy fuses selected regions of a powder bed of materials (such as direct

metal laser sintering (DMLS) and SLM process). This research primarily focuses on components fabricated through SLM process. These components represent the starting condition of the samples used in this investigation.

2.1.2 Powder Material Fabrication

In metallic AM processes, the feedstock materials can be powders, wires or sheets depending on the selected approach. For BJ process and SLM process, pre-alloyed powders are applied as feedstock materials during fabrication. Powder atomization is the most productive and popular route to manufacture pre-alloyed powders with desired particle size, distribution and particle shape. The basic idea of atomization technique is to deliver energy by a certain fluid to a stream of molten alloy, dispersing the liquid alloy into droplets and then solidify to form powder particles. Based on the difference in fluid selection, atomization technique can be divided into gas atomization and water atomization, which can fit well in different applications and are always put together for comparison. There are also special technologies for fabrication of specific alloys, such as electrode induction gas atomization and plasma atomization for fabricating Ti and Ti alloy powders[3].

In gas atomization, molten alloys pass through nozzles and are dispersed into droplets by high pressure gas (air or inert gas), and then solidify while falling into a collecting chamber. Since the temperature of the section containing molten alloys is much higher, those liquid alloys would not solidify in the nozzles and be able to form spherical shape to release surface energy before solidification. Thus, gas atomization produces spherical shape powders with good packing and flowing alloy powders with a size distribution in 15-300 μ m. The final particle size depends on various factors, such as metal flow rate, gas energy (performing as gas pressure and flow rate),

type of gas, nozzle dimensions and liquid metal temperature. Among these above, the flow rate of metal and gas play the most important role. The final particle size D is proportional to the ratio metal/gas flow rate, and the relationship between them can be approximately expressed in Equation (2-1):

$$D = \alpha \frac{dM_M/dt}{dM_G/dt} \quad (2-1)$$

where M_M is the metal mass and dM_M/dt is the metal mass flow rate, and M_G is the mass of gas and dM_G/dt is the gas flow rate. The coefficient α represents other factors which will influence the final particle size, including liquid steel temperature, nozzle dimensions, etc[4].

In water atomization, high pressure water jets are applied to separate the stream of molten alloys. The particle shape of water atomized powders is irregular with rough surface condition since heat is extracted much faster during dispersion and the droplets solidify more rapidly due to higher thermo-conductivity of water than gas. The induction of water can also cause partial oxidation of the powder particles during water atomization due to the reaction between metal and water. In some cases, other liquid fluids have been applied as an alternative of water to reduce oxidation[5]. Similar as gas atomization, the major factors controlling the final particle size are metal flow rate and water flow rate. Water atomization produces irregular shape powders with lower packing density and flowing ability compared to gas atomization, but the cost is much lower than gas atomization due to higher cost of compressed inert gas and vacuum environment protection.

In metallic AM process, gas atomized powder is the preferred feedstock material due to its uniform size distribution, good packing and flowing ability and smooth surface condition to provide uninterrupted feeding of materials during fabrication. However, water atomized powder

has much lower cost than gas atomized powder, and has higher surface energy to release due to its irregular shape, requiring lower energy input during fabrication. The selection of powder depends on the process requirement balanced with cost. Figure 1 shows the morphology of gas atomized powder and water atomized powder.

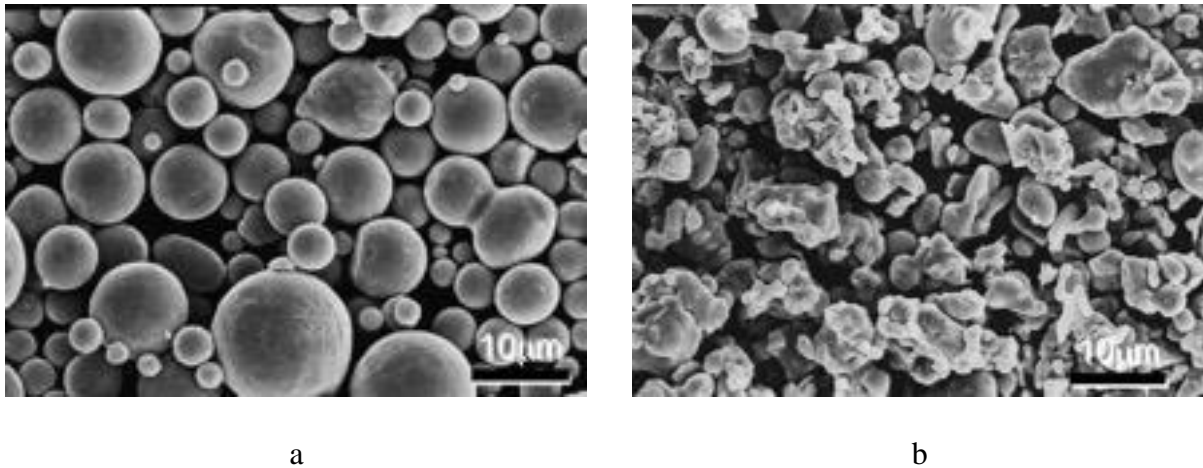


Figure 1. SEM images showing the morphology of (a) gas atomized powder, and (b) water atomized powder[6]

2.1.3 Brief Overview of BJ Process

BJ process is an AM process to join powder particles using a liquid binder. It was originally developed at Massachusetts Institute of Technology (MIT) in the 1990s and became commercialized in 2010[7]. In this process, the system would analyze the pre-designed digital 3D model and slice them into horizontal layers with fixed thickness. When the process starts, the recoater will deposit a thin layer of powder material with pre-set thickness into the working zone. Then a printhead passes through the powder bed and jets the binder to selected areas according to the corresponding cross-section of horizontal layer. The binder is then dried by a heater and the recoater deposits the next layer of powder. The green part is built up by repeating the previous

steps. After printing, the green parts sit inside the powder bed need to be cured at elevated temperature to evaporate the solvent in the binder, to obtain certain strength to be picked up from the powder bed. The green parts are then ready for the following high temperature densification process such as sintering and hot isostatic pressing (HIP) to gain high density and strength. Figure 2 shows the schematic of a BJ process. In this process, the key factors are the selection of powder, the size and distribution of powder[8], binder saturation[9] and the sintering cycle (temperature and holding time)[10].

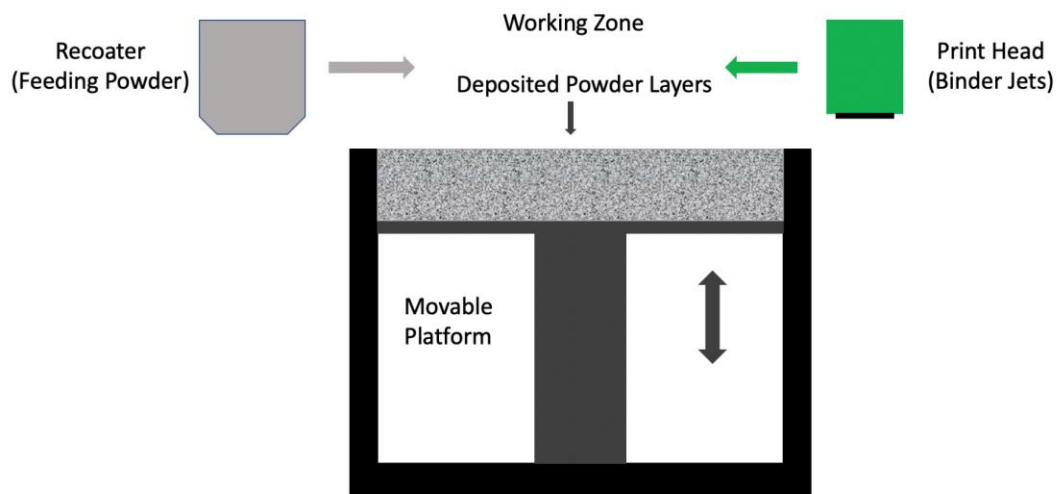


Figure 2. Schematic of BJ process, figure reproduced from [11]

BJ process can be applied to fabricate both metallic[12-14] and non-metallic (ceramics[15-17]) materials fabrication. The advantage of BJ process is that it can accept coarse particle size of powder, which significantly reduces the cost of fine powder fabrication, and makes BJ process the most cost-effective AM technique. Since no heating is applied during the printing process, and the densification is achieved through sintering, the final components are expected to have no residual stress. One disadvantages in BJ process is the post high temperature treatments which can take

much longer than the printing process, increasing the period of fabrication. However, this can be overcome by stacking large batches of parts together in the entire building volume in one printing route, since the parts printed in BJ process can lay in a loose powder bed without additional support. The main limitation of BJ process is the porosity resulting from the sintering of the green parts with low density, since no compacting pressure is applied during printing. Several studies have been exploring various approaches to increase the density of the sintered parts such as using bimodal powder mixtures[8] and applying hot isostatic pressing (HIP) after sintering[18]. However, achieving full density is still a major challenge on BJ components. The microstructure of BJ printed parts is coarse, leading to low mechanical strength. Hence, BJ process is suitable for situations if the printed parts are applied in functional fields, where strength is not a major concern and porosity might be beneficial.

2.1.4 Brief Overview of SLM Process

SLM is one of the most popular powder bed fusion AM techniques to fabricate metallic parts. Similar as the BJ process, it starts from analysis of a pre-designed 3D digital model to thin horizontal layers. Figure 3 shows a brief schematic about how SLM process works. In this process, the initial powder layers need to be fused on a substrate to level the build platform. A mirror-guide laser beam then melts the metal powders in selected area of the powder bed, and the next layer of powder is deposited over the previous deposited layer. Since a high energy laser beam is applied and melting takes place during the printing process, the working chamber requires inert gas protection to prevent from oxidation, which limits the size of working chamber in SLM process. SLM process can fabricate a wide range of metallic materials such as Al-based alloys[19, 20], Fe-based alloys[21, 22], Ti-based alloys[23, 24] and Ni-based alloys[25, 26]. The key processing

parameters of SLM process includes laser power, laser scan speed, hatch spacing distance, hatch styles, layer thickness, contour style, hatch overlap, etc. More commonly, a generated parameter, energy density, E (J/mm^3), is used to describe the energy input of SLM process:

$$E = \frac{P}{v \cdot h \cdot t} \quad (2-2)[27]$$

Where P (W) is the laser power, v (mm/s) is the laser scanning speed, h (μm) is the hatch spacing distance between the scanning tracks, and t (μm) is the set value of layer thickness. The energy density varies according to the type of material due to different thermal responses for those materials, and by adjusting these processing parameters. SLM process can fabricate a wide range of desired properties.

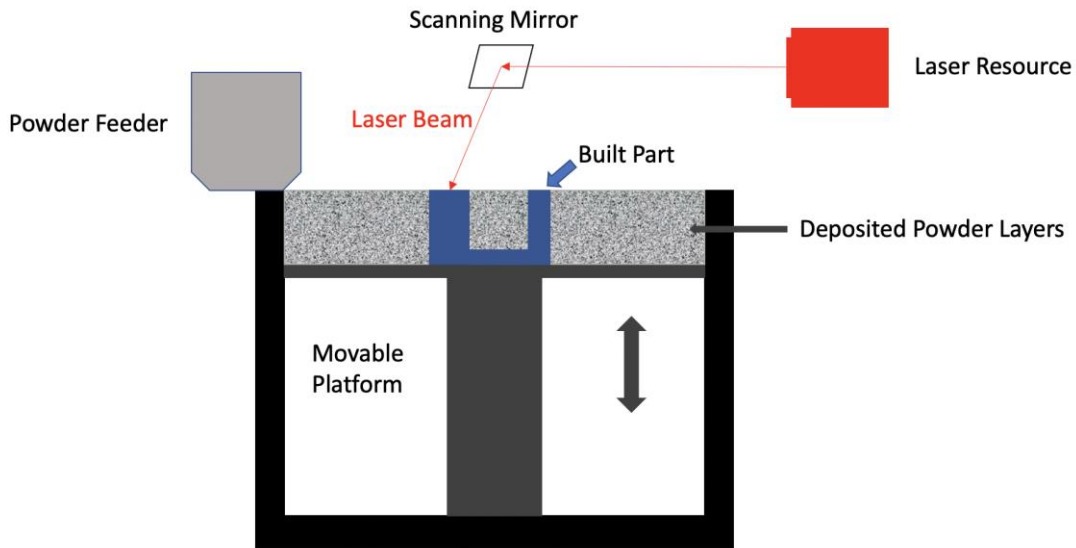


Figure 3. Schemaitc of SLM Process, figure reproduced from [19]

Even though SLM process has flexibility in materials selection and control of properties, it still has severe issues which may influence the build quality of the components. Residual stress is a main concern, since it may lead to thermal deformations, cracks and distortions. The residual

stresses are induced by the large temperature gradient due to rapid melting and cooling in printing process. During printing, the previous solidified layer under the molten layer is heated up rapidly, but its expansion is restricted by the solidified cold part underneath. This introduces a local residual compressive stress leading to possible deformations and cracks if the stress exceeds the yield strength of the material. On the other hand, the molten layer is rapidly cooled down and solidified, but its shrinkage is restricted by the hot layer underneath, resulting in local tensile stresses. Studies have been addressed to solve the problems caused by residual stress in SLM. M. Shiomi, etc. [28] have investigated the residual stress distribution and development in SLM fabricated chrome molybdenum steel mixed with copper phosphate and nickel components, and found that the largest value of residual stress is in the top layer of the components. They also suggested three different ways to reduce the residual stress: post stress relieving heat treatment, rescanning at each layer, and heating up the base substrate. Liu, etc. studied the effect of energy input, scanning track length and scanning strategy to residual stress, and suggested that stronger supports are necessary at both ends of SLM fabricated parts to prevent warps and cracks due to peak values of residual stress occurring onset of the scanning tracks[29]. There are also many other studies related to the effect of residual stresses in various materials regarding stress prediction and processing refinements can be found in the literature[30-34].

Anisotropy of microstructure and mechanical properties is another issue of SLM products which influences their performance. Due to the application of rapid melting and solidification in build-up process, the growth of microstructure is highly dependent on the building direction and the scan strategy, leading to anisotropic mechanical properties. Figure 4 shows an example of as-fabricated SS316L microstructure in OM and SEM images via SLM process, and the black arrow indicates the building direction. As shown in the OM picture, the melt pools are overlapped parallel

to the building direction, whereas the grains grow mostly perpendicular to the boundaries of the melt pools following the heat flow direction. In the SEM image, sub-structures such as equiaxed cellular grains and columnar grains growing parallel to the building direction can be observed. Wakshum M. Tucho, etc. indicates that the formation of the sub-grains can be the consequence of dislocation motion and segregation of heavy elements[35]. The formation of this grain morphology can be explained using the G/V ratio in compositional fluctuation and super cooling theory, where G is the liquid thermal gradient at solid/liquid interface of the melt pool, and V represents the growth velocity of the solid/liquid interface. The increase of G and decrease of V prefer to form more equiaxed cellular grains, and the inverse trend prefers to form more columnar grains[36, 37]. Thus, the G/V ratio can be used to predict the as-fabricated grain structure.

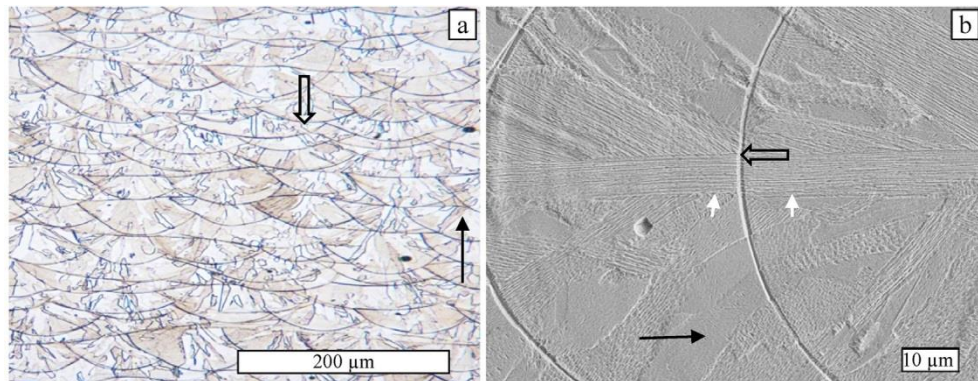


Figure 4 Microstructure of as-fabricated stainless steel 316L via SLM[35]

The SLM produced metallic parts show higher strength compared to conventional manufactured parts due to the ultra-fine microstructure via rapid melting and high cooling rate ($\sim 10^6\text{K/s}$)[38]. Qiu C. etc. summarized a comparison of mechanical properties of stainless steel in between conventional manufacturing and SLM process using various fabrication strategies[39]. They indicated that the as-fabricated components were dominated by clusters of nano-sized γ needles or cells, within which nano-twinning and high dislocation generation would be revealed

during deformation. However, the oriented microstructure from the SLM fabrication results in anisotropic mechanical properties, which has been reported by many researchers. For instance, Im. Y. D. etc. reported anisotropic tensile properties of SS316L fabricated via SLM process[40]. In their research, the yield strength and tensile strength in the vertical direction were 521MPa and 617MPa, respectively, with 56.4% elongation. In the horizontal direction, the yield strength and tensile strength were 583MPa (+12%) and 685MPa (+11%), respectively, with 50.2% (-11%) elongation compared to vertical direction. Other reports of tensile properties anisotropy in SLM process of various materials from previous researchers are listed in Table 1.

Table 1. List of anisotropic tensile properties via SLM process

Material	Yield Strength (MPa)	Ultimate Tensile Strength (MPa)	Elongation(%)	Ref.
Ti-6Al-4V	1093(h)	1279(h)	6(h)	[41]
	1125(v)	1216(v)	6(v)	
Ti-6Al-4V	1195(h)	1269(h)	5(h)	[42]
	1143(v)	1219(v)	4.89(v)	
Ti-6Al-4V	1137(h)	1206(h)	7.6(h)	[43]
	962(v)	1166(v)	1.7(v)	
Ti-6Al-4V(stress relieved)	1145(h)	1187(h)	7(h)	[41]
	1132(v)	1156(v)	8(v)	
IN718	816(h)	1085(h)	19.1(h)	[44]
	737(v)	1010(v)	20.6(v)	
Al-Si-10Mg	169(h)	272.8(h)	8.2(h)	[45]
	168.8(v)	267(v)	9.1(v)	
SS316L	584(h)	667(h)	49(h)	[46]
	588(v)	622(v)	77(v)	

Note: h = horizontal direction, v = vertical direction.

The anisotropy in microstructure and mechanical properties of SLM fabricated components will severely influence their performance in special applications, and several studies have been investigating how to reduce and eliminate the anisotropic properties. Proper adjustment of processing parameters and scanning strategy for more homogeneous residual stress distribution

and microstructure could reduce but not eliminate the anisotropy. Post heat treatment of the SLM fabricated parts can effectively eliminate the anisotropy of microstructure and mechanical properties, but it shows a delay in recrystallization and grain coarsening. For example, the recrystallization temperature of SS316L deformed via conventional process is about 800°C[47], but the SLM fabricated SS316L would not recrystallized and form equiaxed microstructure at this temperature. Yan F. etc. reported that the as-built microstructure of SS316L via SLM process was not removed at 800°C holding for 1h, and it started to be removed after heat treated at 1100°C for 1h[48]. Saeidi K. etc. reported that the as-built SLM fabricated SS316L microstructure became equiaxed after heat treatment at 1400°C for 6min, and pointed out the unique annealing twin formation which should occur in deformed parts prior to annealing[49]. Shamsujjoha Md. etc. reported that evidence of recrystallization and grain growth of SLM fabricated SS316L was observed after 13h annealing at 1100°C[46]. However, researchers also indicate that the post heat treatments would lead to a decrease in strength.

In summary, SLM process is capable in most situation of metallic AM fabrication due to its flexibility of material composition selection and the wide range control of mechanical properties. Processing variables need to be carefully selected to prevent from residual stress generation and formation of defects during fabrication. The as-built microstructure and mechanical properties may be anisotropic due to the metallurgy of rapid melting and solidification. It can be improved via post heat treatments, but needs cautious control in sacrifice of strength.

2.2 Annealing twin boundary

The typical microstructure of SS316L which has low Stacking Fault Energy (SFE) and a face center cubic (FCC) crystal structure is twin boundaries. Twinning occurs when two crystals share part of the same crystal lattice points symmetrically, and the twin boundary separates these two crystals. A 2D appearance of twin boundaries is shown in Figure 5. For AM produced components, the twin boundaries formed in the post heat treatments are annealing twins, since the parts are free of deformation. These special boundaries with low interfacial energy make contribution to strength and ductility by acting as barriers of dislocation motion. Thus, it is important to understand the mechanism of annealing twin formation in AM fabricated SS316L parts.

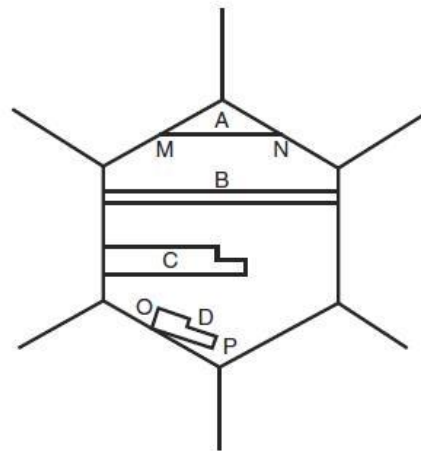


Figure 5. 2D appearance of twin boundaries

2.2.1 General Description of Grain Boundaries

Most AM fabricated metallic parts are polycrystalline microstructures with grains in various orientations, sizes and morphology. Grain boundary, defined as the interface of two

crystals with different orientations, can significantly influence the properties of materials, such as the occurrence of order and disorder, different energy levels, defects, segregations and precipitations, interactions with dislocations at the grain boundaries.

A grain boundary can be characterized using 9 geometrical degrees of freedom[50], and they can be divided into 5 macroscopic degrees of freedom and 4 microscopic degrees of freedom. The 5 macroscopic degrees of freedom are one for the rotation angle θ between the two crystals, two for the rotation axis $[uvw]$ defined by its direction cosines, and two for the orientation of the grain boundary plane defined by its normal vector. The 4 microscopic degrees of freedom are three for the translation of one crystal to the other (the rigid body translation vector) and one for the normal vector to the grain boundary plane that indicates the position of the plane along its normal. The 4 microscopic parameters are not independent of the macroscopic parameters, thus 5 macroscopic degrees of freedom are sufficient to characterize a grain boundary.

A simple way to describe the grain boundaries is to divided them into low angle grain boundaries (LAGB) and high angle grain boundaries (HAGB) according to their misorientation angle θ . Generally the grain boundaries with $\theta < 10^\circ$ are regarded as LAGBs, including interfaces between two slightly misoriented grains and sub-grain boundaries formed within the grains due to work hardening an heat treatment. Grain boundaries with $\theta > 15^\circ$ are regarded as HAGBs. The presence of grain boundaries increases the system total energy from a single crystal, and generally LAGBs contain lower energy than HAGBs. The interfacial energy of LAGBs is highly related to the misorientation angle θ . In 1950, Read and Shockley developed a model to describe the energy of low angle symmetrical tilt grain boundaries γ_θ in function of misorientation angle θ using equation (2-3) to (2-5)[51]:

$$\gamma_\theta = \gamma_0 \theta (A - \ln \theta) \quad (2-3)$$

$$\gamma_0 = \frac{\mu b}{4\pi(1-\nu)} \quad (2-4)$$

$$A = \frac{b}{2\pi r_0} \quad (2-5)$$

where μ is the shear modulus, b is the Burger's vector, ν is the Poisson coefficient and r_0 is the dislocation core radius. For HAGBs, the situation for grain boundary energy is more complicated. In 1989, Wolf expanded this model to HAGBs by substituting θ by $\sin\theta$ [52]. Figure 6 shows the trend of how the grain boundary energy changes with the misorientation angle.

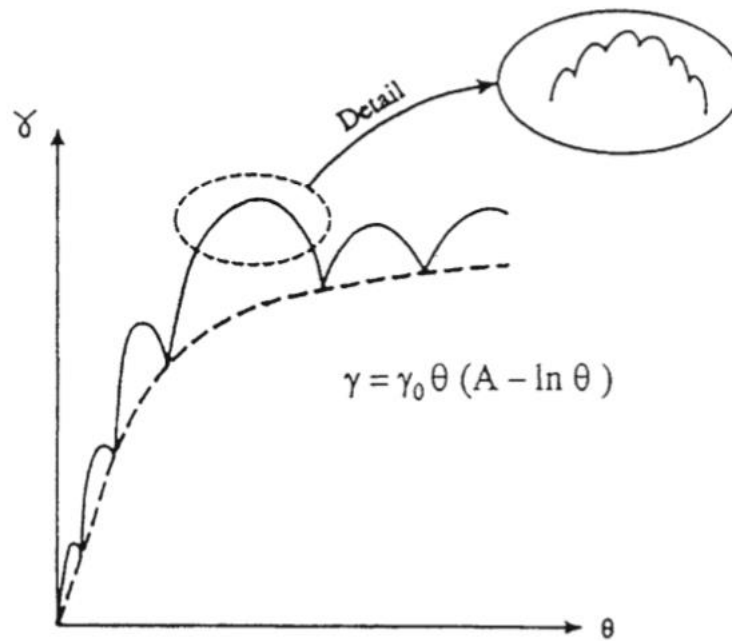


Figure 6. Curve of grain boundary energy versus misorientation angle[53]

W. Bollmann raised up another approach to describe grain boundaries, which is well known as the coincidence site lattice (CSL) theory[54-56]. The coincidence site lattice occurs at specific misorientation angles where some lattice points of one crystal coincide with some lattice points of its neighbor crystal. An integer Σ is used to characterize the CSL named as the coincidence index defined by equation (2-6):

$$\Sigma = \frac{\text{Coincidence unit cell volume}}{\text{Crystal primitive unit cell volume}} = \frac{1}{\rho} \quad (2-6)$$

where ρ is the ratio of the coincidence sites to the total number of sites. Since CSL only occurs at special misorientation angles, the Σ value varies discontinuously with the misorientation angle around a given axis. Thus, a lower Σ value represents a higher degree of coincidence between two crystal, and the boundary is expected to have a lower energy. However, it is necessary to know that the Σ value is not exactly proportional with the grain boundary energy, and the energy depends on the grain boundary plane for the same Σ value[57].

2.2.2 Annealing Twins in FCC Crystallographic Structure

Annealing twins form in deformed and subsequently annealed FCC materials with intermediate ($\sim 70\text{mJ/mm}^2$) or low ($\sim 20\text{mJ/mm}^2$) stacking fault energy, and they were first observed by Carpenter and Tamura in 1926[58]. In FCC crystal structure, the misorientation of the twin boundary satisfies a $\Sigma 3$ relationship in CSL theory, which is 60° about a rotation axis in $\langle 111 \rangle$ direction. More specifically, if the twin boundary plane is parallel to $\{111\}$ plane, it is called a coherent twin boundary (CTB); otherwise it is called an incoherent twin boundary (ITB).

The special twin boundary is also a strengthening mechanism of FCC materials by inducing high strain hardening rates, acting as both barriers to dislocation motion and source for dislocation generation. In 1957, Blewitt found twinning as a mode of deformation mechanism in copper single crystals subjected to tension at low temperature[59], and there have been many studies about various FCC materials and various models of twinning deformation mechanism ever since then. Venables proposed that the prismatic glide source could dissociate into a Frank-type pole dislocation and Shockley type twinning partial, and rotating twinning partial caused the generation

of jogs[60]. Majahan and Chin proposed that two coplanar glide dislocations with different Burgers vectors dissociated into Shockley partials and finally evolved into the dislocation configuration of three-layer twinning[61]. Other sources of twinning nucleation during deformation have also been reported, such as $1/6\langle 411 \rangle$ -type pole dislocation[62], faulted Frank dipole[63] and double cross-slip[64]. T.H. Lee et. al investigated the twinning in deformation in high nitrogen austenitic stainless steel, showing that their results supported Majahan and Chin's three-layer twinning theory[65]. Pei Gu et. al studied the role of slip and slip transfer in FCC materials at nanoscale growth and deformation twinning in strengthening, and provided quantified simulation results of the influence of slip as well as slip transfer to the formation and growth of nanoscale twin boundaries[66]. Jiangwei Wang et. al studied the twinning dominated deformation in nanoscale bcc tungsten using in-situ atomic-scale observation with the help of high resolution transmission electron microscopy, showing that twinning could also be a deformation dominant in body center cubic (BCC) materials[67]. S.H. Joo et. al. studied the twinning contribution to the strain hardening in high entropy alloy using tensile interrupted EBSD and TEM[68].

Annealing twins can form during recovery, recrystallization and grain growth, and they make contributions not only in mechanical properties by acting as barriers of dislocation motion, but also in corrosion and fatigue resistance. There are a lot of studies about controlling the grain boundary character distribution (GBCD) to improve the properties by maximizing the amount of special boundaries such as $\Sigma 3$ twin boundaries via thermomechanical processing, which is also well known as Grain Boundary Engineering[69, 70]. However, it is still controversial in annealing twin boundary formation, and there are several theories about the formation mechanism of annealing twins.

2.2.3 Annealing twin formation theories

Previous researchers have been investigating the role of annealing twin formation, and they have proposed several theories to explain the mechanism. Generally, grain size, temperature, isothermal heating time, velocity of grain boundary migration, grain boundary energy and twin boundary energy can be considered as important factors determining twin boundary frequency. Texture, pre-strain or prior deformation and inclusions are considered as factors but usually not being analyzed carefully.

Some researchers suggested that the annealing twins are formed by growth accidents. Gleiter suggested that annealing twin formation is the result of grain growth accidents[71]. He considered that the atoms transferring to a growing grain at a grain boundary are deposited on the {111} facets during grain boundary migration, and this will lead to the formation of stacking faults. He also suggested that the twin generation probability, R, depends on the activation enthalpy for migration (Q), and the grain boundary migration driving force, which is equal to the difference in Gibbs free energy (ΔG) across the recrystallization front. R can be represented by equation (2-7):

$$R = \exp \left\{ \frac{-Q}{\left(\left(\frac{\pi \varepsilon^2 h^2}{Q \gamma_t} \right) - 1 \right) kT} \right\} \exp \left\{ \frac{\ln \frac{\Delta G}{kT}}{\left(\frac{\pi \varepsilon^2 h^2}{Q \gamma_t} \right) - 1} \right\} \quad (2-7)$$

where ε is the energy of a step on the {111} plane, h is the height of a twin nucleus, γ_t is the surface energy of a coherent twin boundary, k is the Boltzmann's constant and T is the absolute temperature. Meyers and Murr proposed that annealing twins form from grain boundary ledges and diffuse by the migration of non-coherent twin boundaries with Shockley partials[72]. Mahajan and his colleagues suggested that slip-induced damage during grain boundary migration increases

the density of annealing twin boundaries, and different types of twins can be formed according to the angle between the {111} facets and the corresponding grain boundary habit planes[73]. In summary, they all agreed that the essential condition of annealing twin formation is grain boundary migration, and this will lead to stacking faults. The grain boundary migration distance and velocity are two key factors promoting the generation of twin boundaries.

Pande provided another growth accident model for annealing twin formation[74]. His model is derived from the assumption that the increment of annealing twin boundary number per grain, is proportional to the grain boundary migration driving force and the increase in grain size. Since the twin density P is equal to N/D , the twin density decreases when number of twins per grain (N) increases less rapidly than the grain size (D). The twin density P can be described as a function of the arithmetic mean of grain size $\langle D \rangle$ in equation (2-8), by assuming that the driving force only depends on the average grain boundary curvature:

$$P = \frac{1}{\langle D \rangle} K \gamma_g \ln \frac{\langle D \rangle}{D_0} \quad (2-8)$$

where γ_g is the grain boundary energy, D_0 is the minimum critical grain size for the formation on the initial annealing twin boundary, and K is a constant determined by fitting to experimental data. The difference between Gleiter and Pande's models is that Gleiter regarded that twin nucleation occurs at a small angle to the migrating boundary, whereas Pande assumed twin formation almost at right angle to the migrating boundary. According to the growth accident model, there should be more annealing twin formation as the temperature increases.

There are also some studies stating that the annealing twin formation is the requirement of the reduction of grain boundary energy. Fullman and his colleagues suggested that annealing twin formation is the requirement of a reduction in the grain boundary free energy[75]. In this

consideration, annealing twin boundaries could form at the corner of a growing grain when the free energy of grain boundaries between the grain's neighbors and its twin grain is less than it of the boundaries between the neighbors and itself. The interaction with existing twin boundaries during grain growth could stop the boundary migration due to the existence of a minimum free energy position on the boundary. Twin boundaries which end within grains might also disappear if the free energy at the end of a twin boundary is higher than it of the adjacent grain boundary. In summary, they explained the initialization and disappearance of annealing twin boundaries during grain growth from an energy view.

Randle and his colleagues investigated annealing twin formation in nickel and the relationship with grain growth[76]. They proposed that twin boundary formation could be independent of grain growth, because their results showed that once a certain twin density is reached, it will not change by further grain growth. However, in the research of Song et al.[77], they found evidence that annealing twin formation involves grain boundary migration, leading to grain growth. Sumantra Mandal et al. studied the annealing twins and grain boundary character distribution during anomalous grain growth in titanium modified austenitic stainless steel[78]. They found that the proportion of $\Sigma 3$ boundaries increases during annealing due to the formation of the new twin boundaries during grain growth, and these are mainly coherent twins. They also found that the fraction of $\Sigma 9$ boundaries increases at higher annealing temperature, while the fraction of $\Sigma 27$ boundaries remain constant, which indicates that only a few interactions occur between twin boundaries during grain growth. Y. Jin et al. studied annealing twin formation during recrystallization and grain growth in pure nickel[79]. They found that the average twin density increases during recrystallization and decreases during grain growth. Higher migration velocity and the inverse curvature of migrating boundaries prefer annealing twin formation. When grain

growth decelerates, the formation of annealing twins decelerates more sharply due to the reduced annealing twin boundary propagation. They also proposed that during grain growth, large grains consume small grains and their twin boundaries but without producing new twin boundaries, and curvature driven boundary migration is not sufficient to generate annealing twins. B. Lin et al. have observed annealing twin nucleation at triple junctions of grain boundaries during grain growth in nickel[80]. Their results showed that the twin nucleation at triple junctions of grain boundaries reduces the total grain boundary energy, and the selection criteria for the triple points should combine geometric and energetic factors.

2.2.4 Effect of Chemical Composition on Annealing Twins

Considering from both growth accidents and the reduction of overall grain boundary energy, high density of annealing twin boundaries could be expected in materials with low stacking fault energy (high possibility of stacking faults) and high energy grain boundaries. Since stacking fault energy is sensitive to alloying addition, various equations about calculating stacking fault energy of austenitic stainless steel from chemical composition have been proposed, and the effects of different alloy elements have been discussed[81-85]. In austenitic grade stainless steel, the content of carbon is insensitive to stacking fault energy[86]. The increase of silicon, chromium, aluminum and titanium will decrease the stacking fault energy, and the increase of nickel, molybdenum and niobium will increase the stacking fault energy. The stacking fault energy decreases and then increases with the increase of manganese and nitrogen. Several equations and models for stacking fault energy calculation based on chemical composition have been proposed[87-90].

From the view of grain boundary energy, Vynokur indicated that the conventional grain boundary energy can be calculated through the surface energy of austenite and the temperature coefficient of free energy[91]. He applied the inter-polational model to analyze austenitic grain boundary energy and proposed that the conventional boundary energy decreases as temperature increases due to the decrease in surface energy of iron for almost all alloying schemes. Therefore, the influence of alloying elements to grain boundary energy can be characterized by analyzing the changes in its temperature coefficient. According to his calculation in Cr-Mn-Mo austenitic steel, the addition of Ni, V, Ce and Cu would not change the free boundary energy much; the addition of Cr, Ti and Al would increase the free energy of grain boundary from 1000-1300°C; the addition of Mo would increase the free energy of boundary at 1000°C but not change the energy from 1100-1300°C.

In summary, the addition of Si, Cr, Mn, Al and Ti can be considered for the decrease of stacking fault energy to increase the possibility of annealing twin formation, and the addition of Cr, Ti and Al is considerable to increase the amount of high energy grain boundary with high mobility to fit the requirement in reduction of boundary energy during grain boundary migration.

The impact of high energy (ultra-fast heating rates) heat treatments on the annealing twin formation of low SFE materials has not received considerable attention in the literature. In addition, the effect of low heat conductivity in austenitic stainless steels in terms of high local stresses has not been published in the open literature. These two major points were the central drivers for this work. The results were documented, discussed and presented in support of the original hypothesis.

3.0 Experimental Procedure

3.1 Material Selection and Processing

The base material used in this research is SS316L, and there are several reasons for selecting SS316L in this research. On one hand, SS316L is an austenitic stainless steel with FCC crystallographic structure and low stacking fault energy. These characteristics promote annealing twin formation, which fits the goal of this research. On the other hand, from the marketing view of industries, SS316L is one of the most popular materials applied in additive manufacturing due to its good mechanical properties at elevated temperature and corrosion resistance.

In this study, gas atomized powder was applied according to the requirement of the SLM 3D printing system. Samples with dimensions of around 20*8*5mm were fabricated via EOS 3D printing system. The chemical composition of the applied powder is shown in Table 2.

Table 2. Chemical composition of gas atomized powder for SLM process

Element	C	O	S	N	Cr	Mo	Si	Ni	Mn	Cu	Fe
wt%	0.011	0.041	0.006	0.10	16.829	2.326	0.632	10.911	1.226	0.034	Bal.

To study the effect of heating rate on annealing twin boundary formation, the fabricated samples were then post-heat treated with various heating rate by using a high frequency laboratory induction heating system. The system applies high frequency alternative current to a cyclic conduct to produce flux, and the printed material is put in the coiling area to make the flux run through. Eddy current will be generated in the direction of self-capturing with the rotary current, then the

induced current generates heat. Figure 7 shows a schematic of the induction heating system, and theoretically it is supposed to provide a heating rate as high as $700^{\circ}\text{C}/\text{s}$. The application of this system can shorten the processing period. By applying this fast heating approach, the effect of heating rate was investigated.

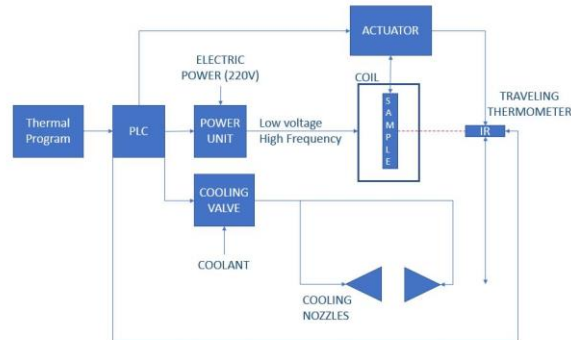


Figure 7. Schematic of the laboratory induction heating system

In this study, three temperatures (1150°C , 1200°C , 1250°C) and three heating rates ($10^{\circ}\text{C}/\text{s}$, $100^{\circ}\text{C}/\text{s}$, $200^{\circ}\text{C}/\text{s}$) were applied using induction heating system with isothermal heating time range of 3-60min. In addition, for comparison purposes, a control set of experiments were done at 1150°C using conventional slow heating rates. After the heat treatments, all samples were quenched using ice brine.

3.2 Microstructural Characterization on OM and SEM

3.2.1 Sample Preparation

All samples were prepared via conventional sample preparation procedures. First of all, the specimens were cut using an IsoMet precision diamond saw to prepare the samples for observation and analysis of the cut cross-section interface. Then the samples were mounted with copper-based conductive mounting powder at elevated temperature ($\sim 150^{\circ}\text{C}$) and pressure ($\sim 4200\text{psi}$) for about 10 min by a compression mounting machine, to form cylinders with specimens at the center position. The mounted samples were then ground with silicon carbide fine sand paper step by step, starting from 400 grit to 1200 grit, and then polished with $0.05\mu\text{m}$ aluminum oxide mixed in DI water to eliminate the scratches created from previous grinding. Finally, the samples were vibratory polished with $0.05\mu\text{m}$ aluminum oxide suspension on a VibroMetTM for 3 hours to prepare fresh and even surfaces.

3.2.2 Microstructural Observation

After preparation, samples were etched using a mixture of acid ($\text{HNO}_3:\text{HCl}:\text{H}_2\text{O} = 1:1:1$) to reveal the general microstructure for observation in OM and SEM.

For OM observation, a ZEISS Smartzoom 5 Digital Microscope was applied in this study. It provides various magnifications from 10x to 2020x, with a maximum resolution of $\sim 0.56\mu\text{m}$.

For SEM observation, a ZEISS Sigma 500 VP SEM with Oxford Aztec X-EDS attachment was applied. It is a field-emission SEM with a wide range of accelerating voltage (0.2-30kV) and

can provide high resolution (1.5nm at 15kV). The attached energy dispersive X-ray analysis spectrum can also provide information of elemental composition.

3.2.3 EBSD-OIM Analysis

Electron backscatter diffraction (EBSD) technique is for microstructural-crystallographic characterization based on the acquisition of diffraction pattern from a bulk sample in an SEM. It can provide information about crystal orientation, misorientation distribution, grain boundary characters, textures, etc. The EBSD acquisition system consists of a phosphor screen, a compact lens and a CCD camera. In SEM, a specimen is highly tilted ($\sim 70^\circ$) from the horizontal towards the diffraction camera to increase the contrast of the diffraction pattern. Samples for EBSD analysis need to be flat. Figure 8 shows a simple schematic of EBSD analysis.

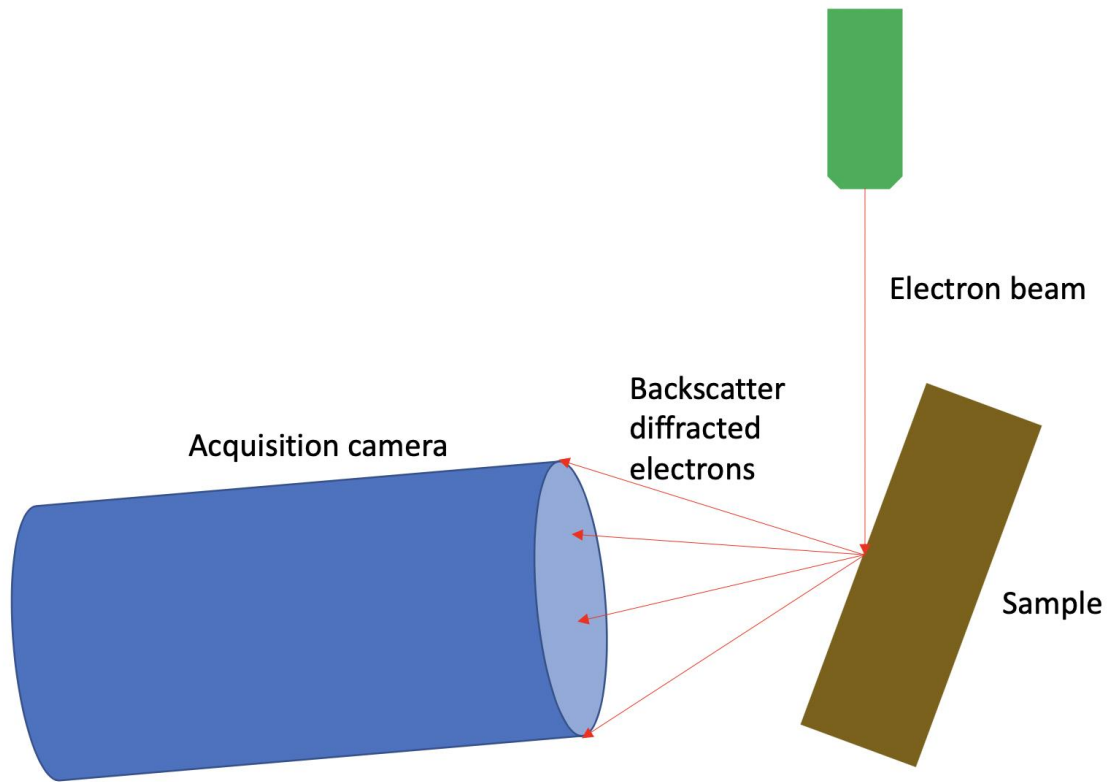


Figure 8. A schematic of EBSD acquisition inside SEM

All samples were prepared via the same sample preparation procedure in section 3.2.1 to obtain fresh and even surfaces for further EBSD analysis in order to acquire information about misorientation distribution and grain boundary characters for twin boundary analysis. The characterization was done using an FEI Scios FIB/SEM Dual Beam system with EDAX EDS/EBSD microanalysis attachment.

For each EBSD scan, an area of $500\mu\text{m} * 500\mu\text{m}$ was scanned with a hexagonal grid at the step size of $1\mu\text{m}$ at 200X magnification to include sufficient grains for analysis. After scanning, 4 steps of clean-up methods were applied to eliminate the erroneous data before further analysis: grain dilation, grain CI standardization, neighbor CI correlation, neighbor orientation correlation. Grain dilation method is an iterative clean-up method acting on points which does not belong to

any grains. These points can be lack of indexing or belonging to a grain group with fewer members than the minimum grain size, and they will be changed to match the orientation of the majority grain which their major neighbors belong to. Grain CI standardization method is to change the confidence index (CI) value of all points in a grain to the maximum CI found among these points. This enables a point with low CI value but a similar orientation as that of its surrounding points to be distinguished correctly in following data analysis. Neighbor CI correlation method performs on data points with CI values less than the user defined minimum CI value, and changes their CI values to the neighbors with maximum CI values. Neighbor orientation correlation method exams the data points with CI values less than the user defined minimum CI value. It checks if the orientation of the point is different from its immediate neighbors than a given grain tolerance angle, and if the required number of nearest neighbors is different, it checks the number of nearest neighbors which represent like orientations to within the given tolerance angle. If all conditions are satisfied, the orientation of the point will be changed to one of the neighbors satisfying the previous conditions. For all clean-up methods, the grain tolerance angle was set at 5 degrees, the minimum grain size was set at 2 pixels and the minimum CI value was set at 0.1.

3.3 TEM Analysis

Nanoscale crystallographic information about the twin boundaries and microstructure were analyzed using a field emission gun TEM (JEOL JEM2100F) with accelerating voltage at 200kV, vacuum level below 1.5×10^{-5} Pa, spot size = 1 and alpha = 3. For TEM observation, thin foils of specimens with thickness smaller than 100nm were prepared through the following steps: 1) cut a thin piece of sample with around 0.5mm thickness using an Isomet diamond saw cutter; 2)

mechanically grind the thin piece via different grades of sand papers (starting from 240, and then following 320, 400, 600, 800 and 1200) to a final thickness less than 60 microns (thickness was measured using a screw micrometer during grinding); 3) use a mechanical punch to produce disk specimens with a diameter of 3mm from the ground thin piece of sample; 4) use twin-jet electrolytic polishing technology to penetrate a hole near the center of the 3mm disk specimens (5% Perchloric acid dissolved in ethanol was used as the electrolyte solution); 5) if necessary, use Argon ion milling (Model 1050 TEM Mill) to clean the sample surface and to expand the thin area around the hole after twin-jet polishing. In order to prevent the change of microstructure due to the heat during twin-jet polishing and ion milling, the twin-jet polishing was done at a temperature below -20°C and the ion milling was done at a temperature below -120°C.

3.4 Microhardness Measurements

The microhardness of a material represents its ability to resist plastic deformation, and therefore it can be used to evaluate the ultimate tensile strength. In this study, the Vicker's criterion was applied to evaluate the microhardness, and a LECO LM digital Vicker's microhardness tester was used for measurements with 300gf load and 10s dwell time. According to ASTM E92-82[92], the Vicker's hardness number (VHN) is defined by equation (3-1):

$$VHN = \pi r^2 \frac{F}{A} \approx \frac{1.8544F}{d^2} \quad (3-1)$$

where F is the load in kgf and d is the average diagonal length of indentation in mm.

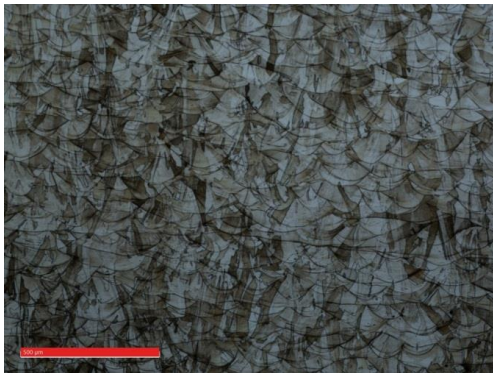
4.0 Results

4.1 General Observation of Microstructure

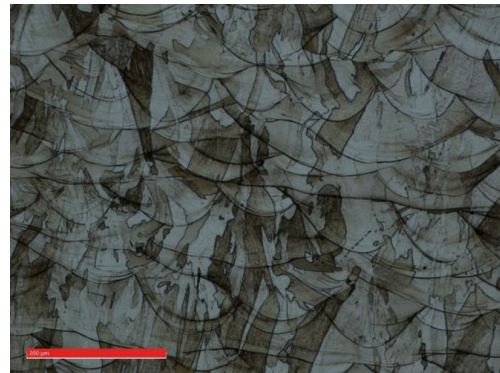
As mentioned in the previous chapter, the printed SLM SS316L specimens were heat treated at various temperatures from 1150°C to 1250°C and held for 3-60 min, via heating rates of 10°C/s, 100°C/s and 200°C/s. The results of these experiments will be presented in this session.

4.1.1 Microstructure of As Fabricated Sample

First of all, the as-fabricated sample via SLM process was analyzed. Figure 9 shows the OM images of the as-fabricated SLM SS316L. From the images, we can clearly see the built-up layers of SLM process. The morphology of the melt pools overlapping parallel to the building direction indicates that the fusion of the powder was sufficient during fabrication and the bonding between the layers is strong.



200x



500x

Figure 9. OM images of as-fabricated SLM SS316L at different magnifications

Figure 10 shows SEM images at higher magnifications of the microstructure of as-fabricated SLM SS316L with a dendritic arm spacing of 1-2 μ m. The SEM images show the columnar grains growing from the melt pool boundary and growing further into the melt pool. The growth direction of the grains is influenced by the competition between the preferred crystal orientation and the preferred heat flux direction, the Marangoni flow [93] may cause changes in heat transfer direction and the fluid flow in a melt pool. This explains why not all the columnar grains grew along the direction perpendicular to the boundary of the melt pool.

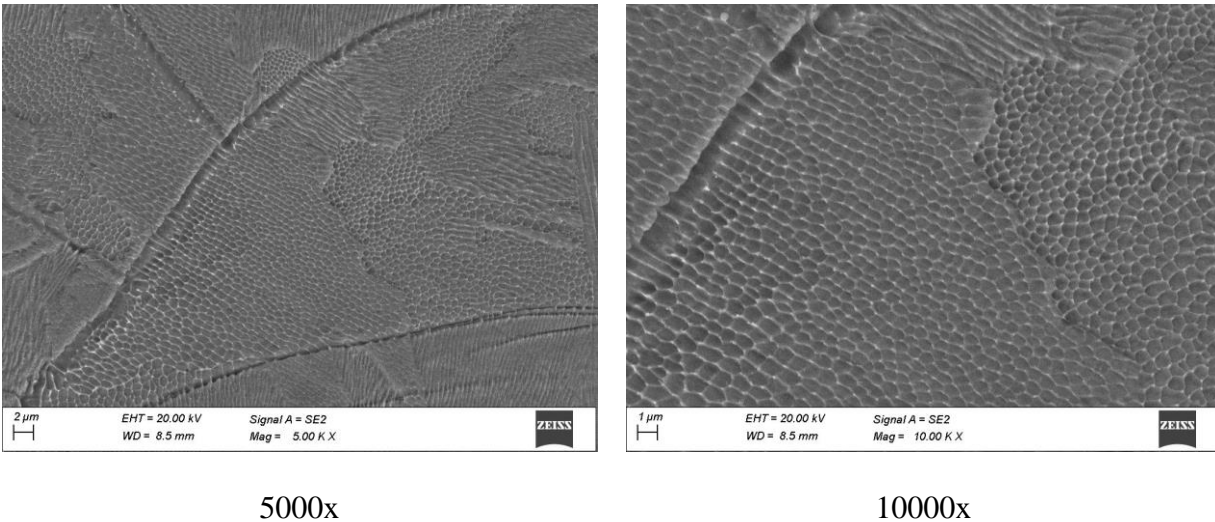


Figure 10. SEM images of as-fabricated SS316L samples at various magnifications

4.1.2 Microstructure of Heat Treated Samples

The first set of heat treatments were done at 1150°C holding from 12 min to 60 min, with rapid heating (200°C/s) (figure 11a-e) and furnace heating (~0.1°C/s) (figure 11f-j), respectively, to reveal and compare the change of microstructure during heating with conventional slow heating rate and rapid heating rate. Figure 11 includes the OM images showing the microstructure of SLM SS316L samples after these heat treatments. For heat treatment at 1150°C, the overlapping melt

pool structure disappeared after 12 min for both heating rates compared to figure 9. As the holding time increased, the grains with irregular shape started to change to equiaxed morphology, and the formation of new small grains indicated that recrystallization was taking place. Annealing twin boundaries started to form and the amount increased as the holding time increased. After holding for 48 min, the initial printing structure was almost completely removed with most of the grains becoming equiaxed and increasing amount of annealing twin formation. Under this time interval (12min) at 1150°C, even though it is difficult to observe big differences about the change of microstructure and the time when annealing twin formation started to occur between rapid heating and conventional furnace heating only via OM images, the rapid heating process has rapidly shortened the processing period to get similar microstructure. Thus, the rapid heating technique can achieve similar microstructure as conventional heat treatment with much less time.

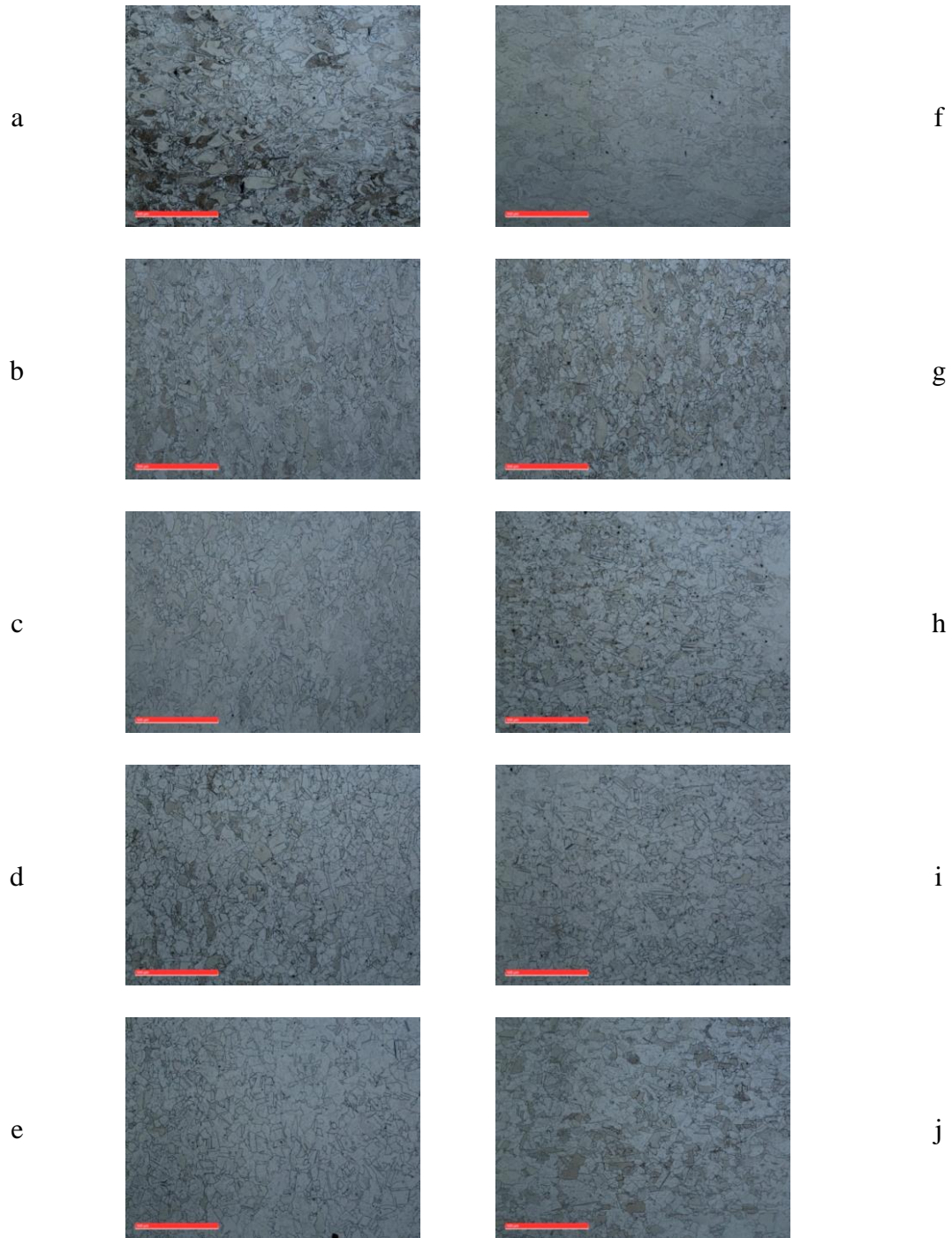


Figure 11. OM images of SLM SS316L samples heat treated at 1150°C with rapid heating at 200°C/s and held for (a) 12min, (b) 24min, (c) 36min, (d) 48min, (e) 60min; and with furnace heating (~0.1°C/s) and held for (f) 12min, (g) 24min, (h) 36min, (i) 48min, (j) 60min

Figure 12 shows the SEM images of the same series of samples as figure 11 shows. The images show similar microstructural evolution as the OM images. In comparison with figure 10, the initial sub-columnar grain structure disappears at the beginning of heat treatment. After holding 12min, annealing twin boundaries appear at both heating rates. The microstructure continuously changes from irregular to equiaxed geometry. The microstructure of 200°C/s series samples are finer than that of 0.1°C/s series samples. It is also found during sample preparation that the anti-corrosion ability of SLM SS316L increases after heat treatments for both heating rates. Using a mixed acid ($\text{HCl} : \text{HNO}_3 : \text{H}_2\text{O} = 1:1:1$), it takes about 30s to reveal the microstructure for as-fabricated specimen. After heat treatments for 12-36min, the samples take about 60s to reveal the microstructure, and the samples heat treated for 48-60min take more than 120s to reveal the microstructure using the same reagent. The increasing in anti-corrosion ability after heat treatment due to the appearance of annealing twin boundaries is consistent with Chen's research, that the best anti-corrosion ability of heat treated gas-metal arc additive manufactured (GMA-AM) stainless steel 316L is the specimen heat treated at 1200°C for 4hrs which annealing twin boundaries occur[94].

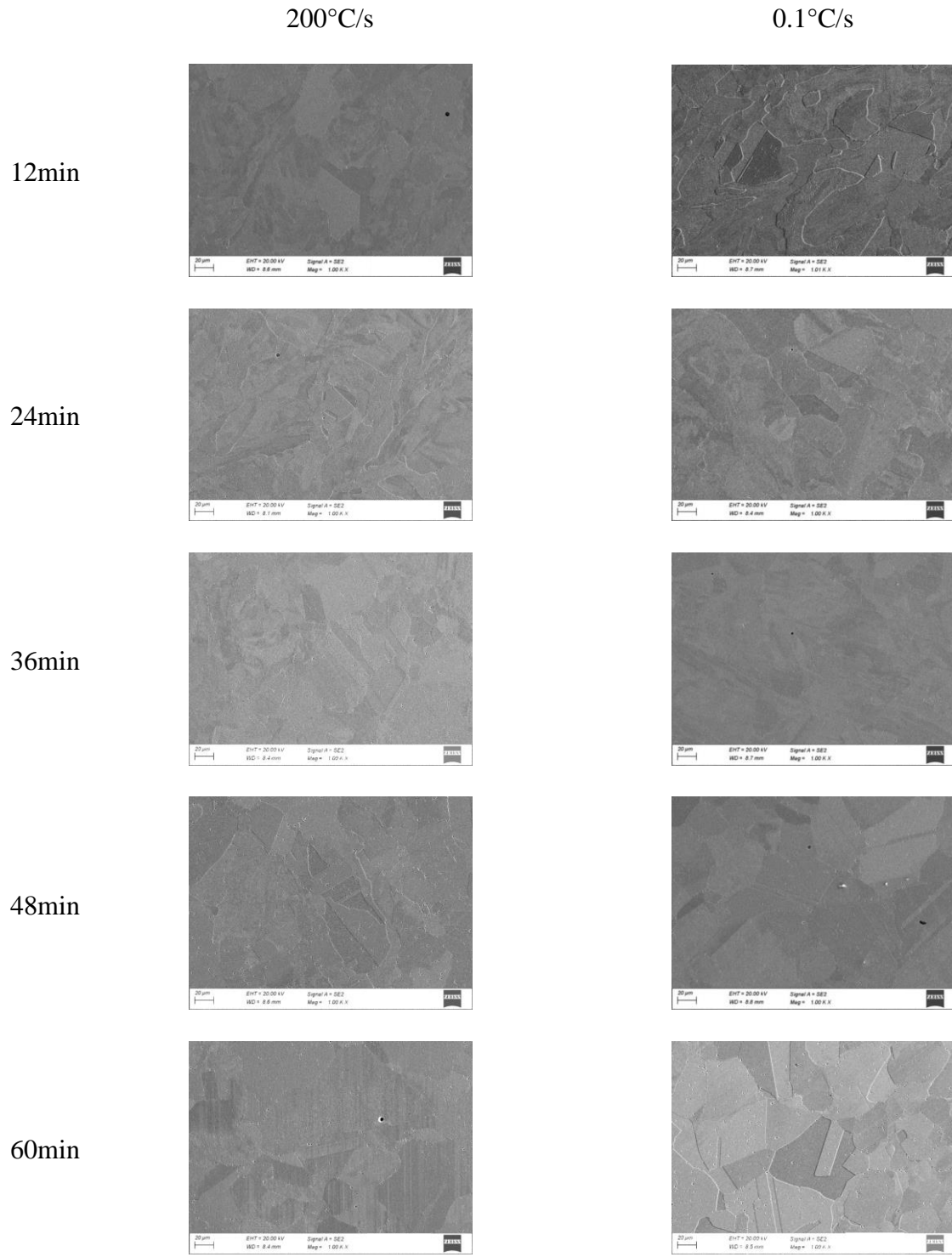
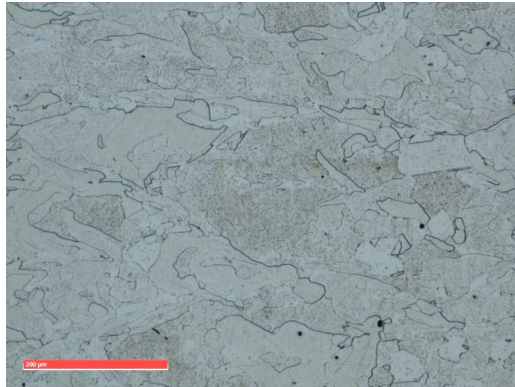
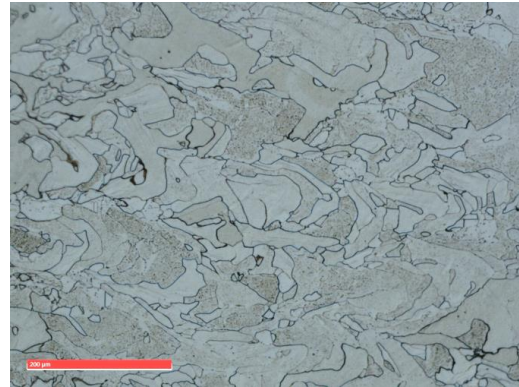


Figure 12. SEM images of SLM SS316L samples heat treated at 1150°C with rapid heating at 200°C/s and 0.1°C/s for 12-60min

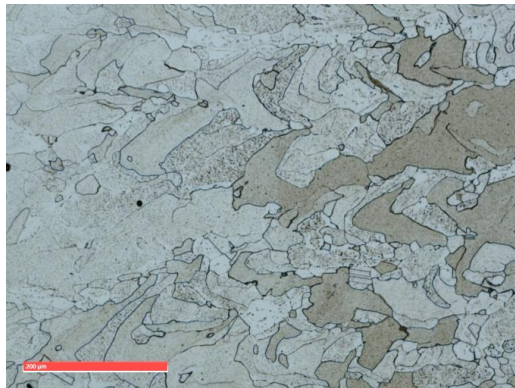
Based on the results obtained after holding 12min at 1150°C twin boundaries were observed from the previous sets of samples, various heating rates were applied at same temperature and holding time to see the effect of heating rate. Figure 13 shows the OM images of SLM SS316L samples heat treated at 1150°C holding for 12min at various heating rates. The results showed that holding for 12 minutes for a given heating rate, the initial melt pools disappeared. A comparison of the images, the microstructure got finer and more twinning structure were observed as the heating rate increased.



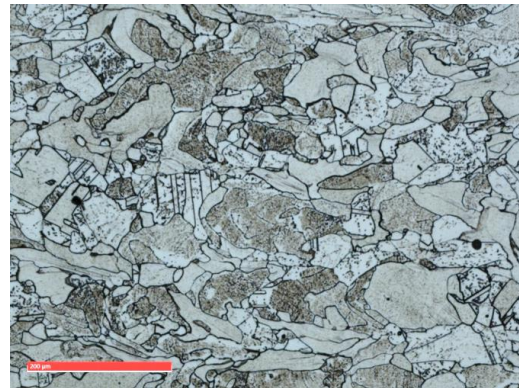
~0.1°C/s



10°C/s



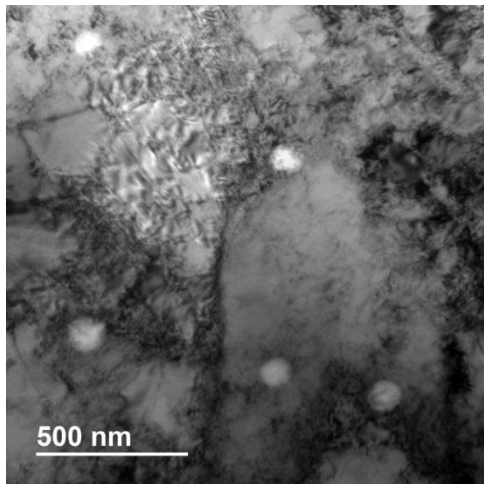
100°C/s



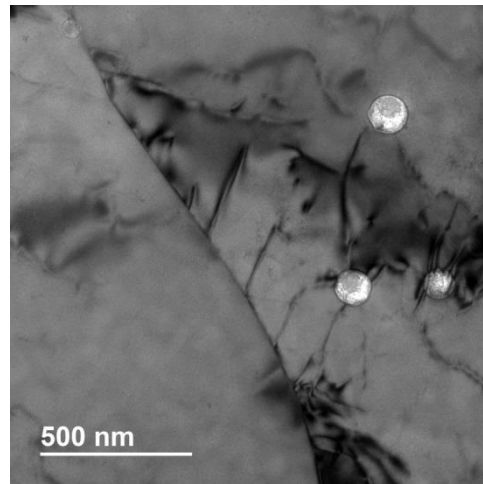
200°C/s

Figure 13. OM images of SLM SS316L samples heat treated at 1150°C and held for 12 min at various heating rates

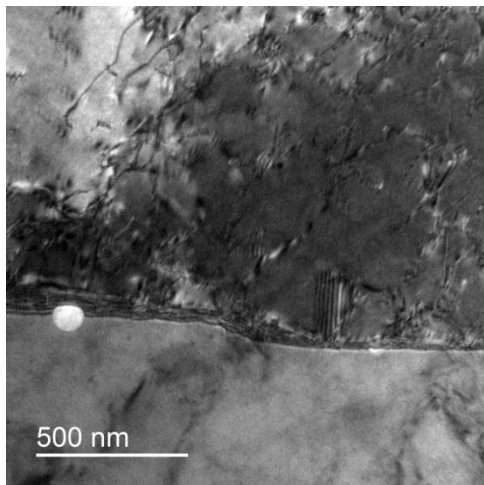
Figure 14 shows the TEM images of as-fabricated samples and heat treated samples holding from 3-12min at 1150°C with 200°C/s heating rate. Si-Mn-O inclusions were observed in both as-fabricated samples and heat treated samples. These inclusions distributed in the sub-structure in as-fabricated samples. During heat treatment, the inclusions were distributed in the grains first (at 3min), and then interacted with grain boundaries in boundary migration (at 6min), finally they were left behind the grain boundaries. The Mn-O inclusion can be from the powder fabrication. It has been reported that Mn is easy to oxide on stainless steel 316L powder surface[95]. The Si-O inclusion can be due to the most negative Gibbs free energy and hence the highest oxygen affinity during SLM process[96].



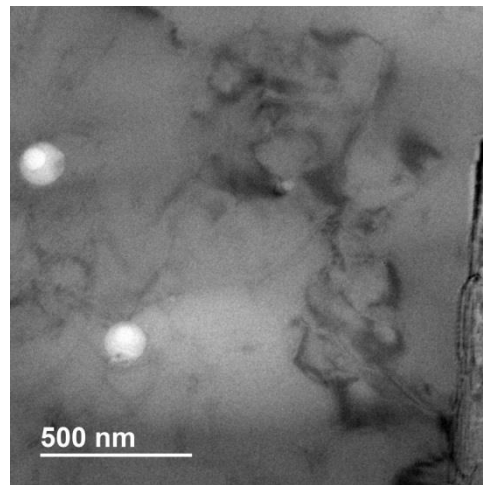
As-fabricated



3min



6min



12min

Figure 14. TEM image of SLM SS316L as-fabricatd samples and heat treated samples at 1150°C with 200°C/s holding from 3-12min

Heat treatments were also done at 1200°C and 1250°C with $\sim 0.1^\circ\text{C/s}$, 100°C/s and 200°C/s heating rates and 12min holding times to obtain a broader map about the effect of processing parameters. Figure 15 shows the OM images of SLM SS316L samples heat treated at 1200°C and 1250°C for 12min with various heating rates. Compared with figure 13, the microstructure became more equiaxed as the temperature increased at all heating rates. For microstructures at 1200°C,

there were a few areas of un-equiaxed grains, while grains were equiaxed in almost all over the area at 1250°C. By comparing the level of equiaxed microstructure in figure 15 and it in figure 11e and figure 11j, it is clear that the transformation of microstructure from as-fabricated type to most of equiaxed type takes around or less than 12min at 1200°C and 1250°C, while it needs to take almost 60min at 1150°C. As expected the rate of static recrystallization was influenced dramatically by temperature. Abnormal grain growth was observed at 100°C/s and 200°C/s rapid heat treatments at 1200°C and 1250°C. The results seem to indicate that faster heating rates leads to grain growth at higher reheating temperatures, as figure 16 shows. While at lower heating temperatures, i.e., 1150°C, faster heating rates produces an uniform grain size. It is difficult to tell that faster heating rate leads to finer microstructure at 1200°C and 1250°C, which is different from the trend at 1150°C.

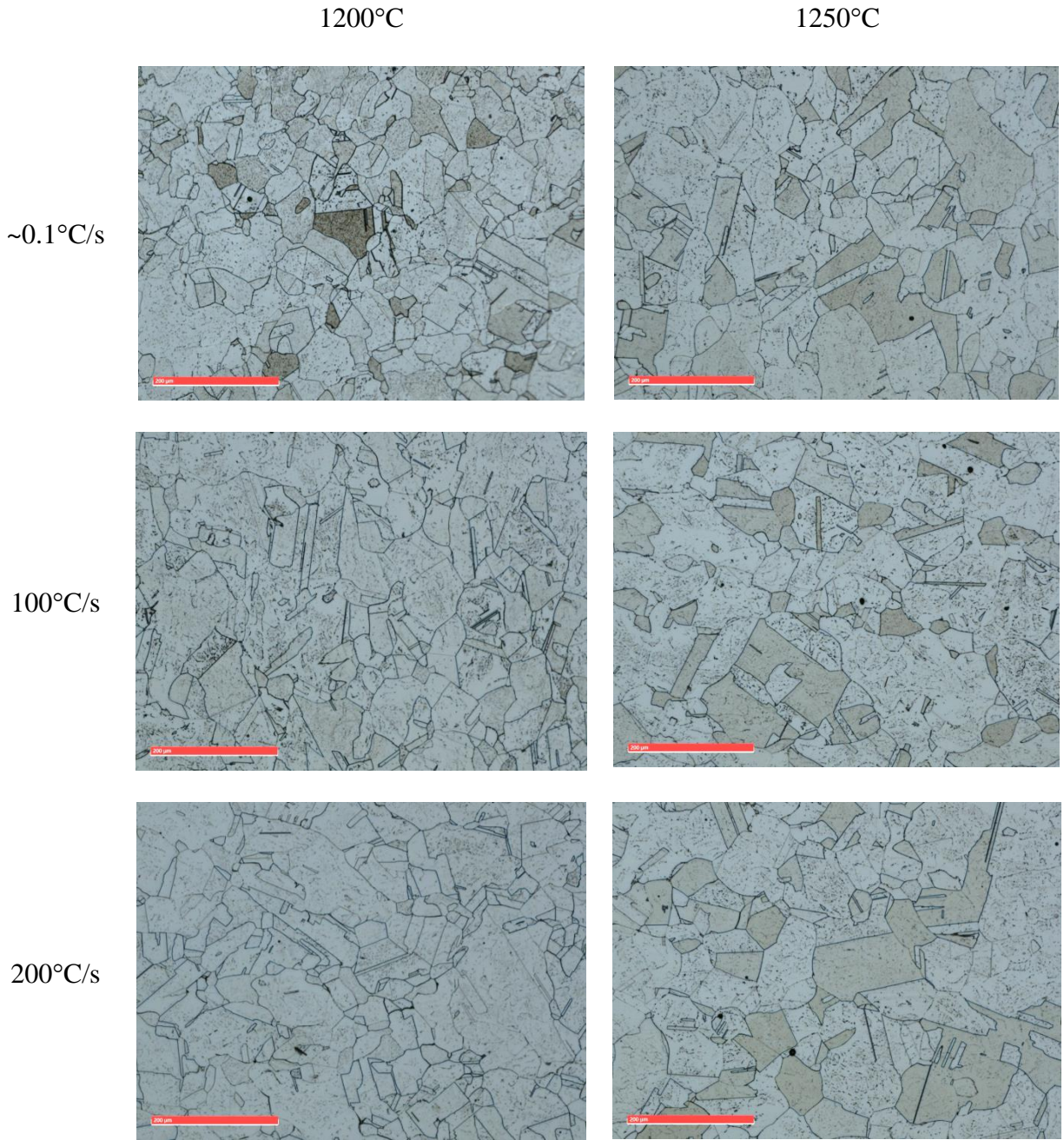


Figure 15. OM images of SLM SS316L samples heat treated at 1200°C and 1250°C and held for 12 min at various heating rates

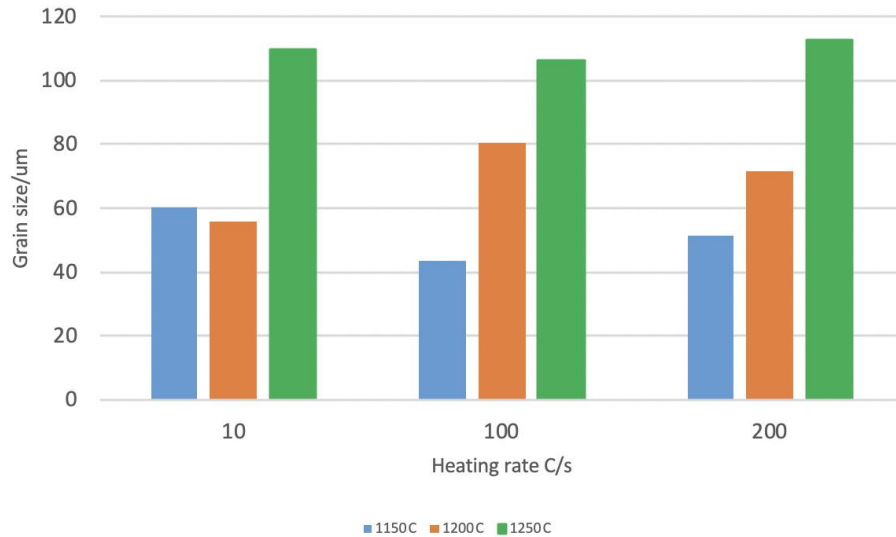


Figure 16. Relationship between grain size and heating rate for SLM SS316L samples heat treated at different temperatures holding for 12min

4.1.3 Summary

In this section, it has been presented the following microstructural changes as function of reheating temperature for a given heating rate: 1) the progressive change of microstructure from a rapid solidified or weld-like structure with overlapping melt pools to a microstructure containing equiaxed grains and twin boundaries; 2) the kinetics of static recrystallization increased as function of heating rate and reheating temperature; 3) at lower reheating temperatures the impact of increasing heating rates resulted in finer microstructures; 4) after the microstructure changed from a dendritic-like to a fully equiaxed grains, increasing reheating temperatures and heating rates led to grain growth. These results are in good agreement with classical grain coarsening theories.

4.2 Annealing Twin Density Characterization

In this section, it will be discussed the formation and development of annealing twin boundaries during heat treatment. The annealing twin density observed and measured using the EBSD technique is presented. Since the crystal structure of SS316L is FCC type, boundaries which satisfied $\Sigma 3$ relationship (60° misorientation angle at $\langle 111 \rangle$ direction) were regarded as the total amount of twin boundaries in EBSD analysis in this study. The $\Sigma 3$ boundaries were characterized with a CSL misorientation tolerance according to Brandon's criteria [97] shown in equation (4-1):

$$Tolerance = \frac{K}{\Sigma^n} \quad (4-1)$$

Where $K = 15$, $n = 0.5$, and Σ is the coincidence index. Based on this twin misorientation tolerance, a $\Sigma 3$ boundary was considered a coherent twin boundary when its boundary plane coincides with the twinning plane, which means the $\{111\}$ plane of the crystals on either side of the boundary must be aligned with the grain boundary plane. Theoretically, EBSD-OIM technique is not able to process this 3-D criteria with only one scan on each sample since it provides 2-D scans. However, based on Randle's research[98], the boundary plane and the twinning plane are aligned. The check of trace alignment can be provided by EBSD. Thus, coherent twin boundaries were identified through this method via EBSD-OIM analysis in this study. The difference between the total twin boundaries and the coherent twin boundaries was regarded as incoherent twin boundaries.

4.2.1 Annealing Twin Density Comparison at 1150°C

Figure 17 includes a set of comparisons from EBSD scan results between rapid heating rates and conventional low heating rates heat treatments at 1150°C. The soaking time at this reheating temperature varied from 12-60 minutes. The first and third columns shown in figure 17 are the Inverse Pole Figures (IPF) of the conventional slow heating and induction fast heating treatments. From the IPF's, both slow heating and fast heating specimens show random preference in crystallographic orientation. The second and fourth columns show the overall change in annealing twin boundaries with increasing soaking time at slow and fast heating rates. The black line represents high angle grain boundaries with misorientation $> 15^\circ$. The red line, blue line and yellow line represent $\Sigma 3$, $\Sigma 9$ and $\Sigma 27$ boundaries, respectively. The amount of twin boundaries increases as the soaking time increases, and most of the twin boundaries appear in equiaxed grains. Both of the heat treatments conditions show low amount of the so called 'twin variants' $\Sigma 3^n$ boundaries (in this case $\Sigma 9$ and $\Sigma 27$ boundaries). An interesting observation is that at low heating rates the nature of the as-solidified microstructure changes to a more equiaxed microstructure at lower reheating temperatures and shorter times compared to the faster heating rates at the same temperature. This is an interesting point because the thermal conductivity of an austenitic stainless steel matrix (non-magnetic) seems to retard the heat transfer through the whole specimen when high heating rates and short holding times are applied. To obtain similar microstructures the holding time needs to be increased to at least 48 min, compared to 12 minutes during conventional low heating rates.

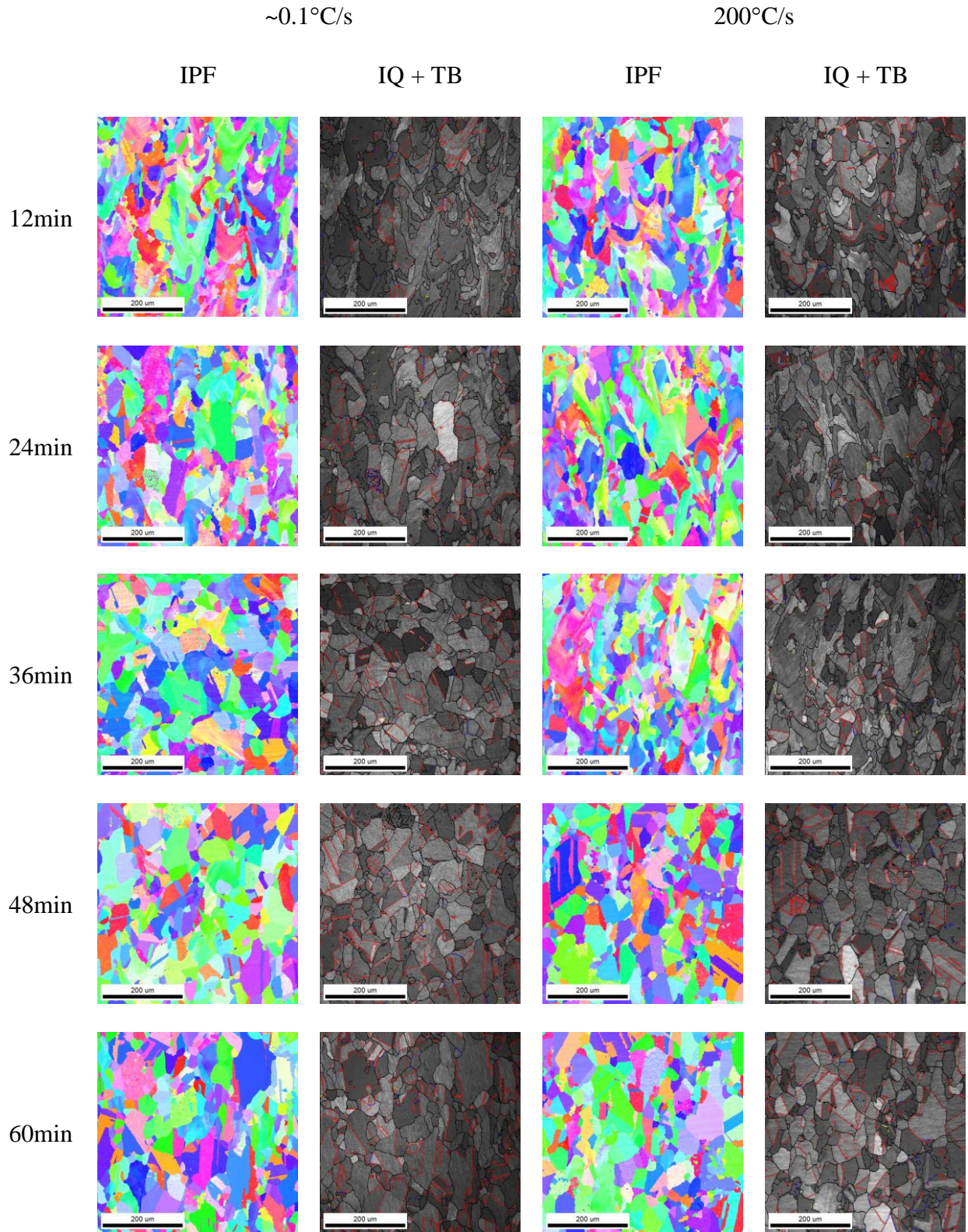


Figure 17. IPF and IQ + Twin boundary results from 500*500 μm EBSD scans of 1150 $^\circ\text{C}$ heat treated samples from 12-60min at slow and fast heating rates

Figure 18 shows the change of the coherent twin density and incoherent twin density with holding time at 1150°C. The length twin density was calculated using the total length of the twin boundaries divided by the scanned area. Both coherent and incoherent twin density increase as holding time gets longer at both 0.1°C/s and 200°C/s heating rates at 1150°C. The curves of coherent twin density in figure 18 show two steps of increase through the holding time. The coherent twin density first increases to 4-6mm⁻¹ after holding for 10-25min, and then dramatically increases above 10mm⁻¹ after holding for 40min at both heating rates. The first increasing step of coherent twin density in 200°C/s heating rate appears earlier than it in 0.1°C/s heating rate, indicating that fast heating rate initiates the twin boundary formation faster than slow heating rate. The coherent twin density of 0.1°C/s is higher than it of 200°C/s after the second increasing step, but they are still comparable. The difference may be related to the lower thermal conductivity of the austenitic matrix when fast heating rates are employed. Incoherent twin density shows similar trend as coherent twin density.

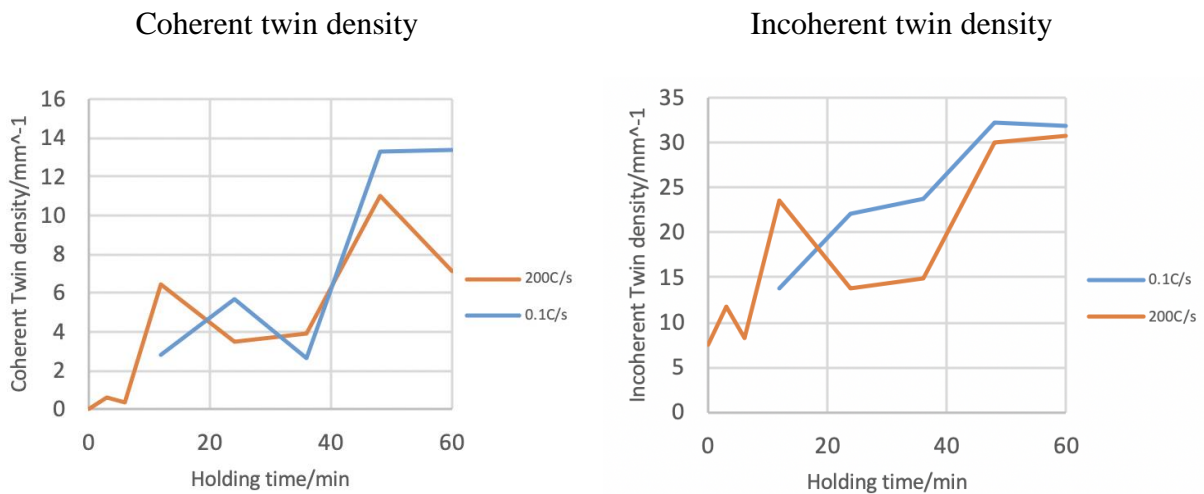


Figure 18. Length twin density vs. holding time at 1150°C

Combining the twin density curves from figure 18 and the microstructure from figure 17, it is clear that the increase of annealing twin density is highly related to the recrystallization process that changes the microstructure from overlapping melt pool type to equiaxed grain type. EBSD can provide information about grain orientation spread (GOS), which can be applied to measure the percentage of recrystallization. In the GOS calculation in EBSD analysis, the difference of misorientation angle between a point inside a grain and the mean misorientation angle of the grain is calculated for every point in this grain, and the average value of this misorientation difference is defined as the GOS value. It represents the degree of distortion of a grain, and recrystallized grains are deformation-free, therefore it can be used to measure the degree of recrystallization. Usually for grains with $GOS < 3^\circ$ can be considered as recrystallized grains[99], some researchers may use the criteria $GOS < 1^\circ$ [100]. In this study, $GOS < 2^\circ$ was applied as the criteria of recrystallization.

Figure 19 shows the results of EBSD analysis related to GOS at 1150°C . The red area represents the area with $GOS < 2^\circ$. The yellow line highlights the total $\Sigma 3$ boundaries, while the blue line only highlights the coherent twin boundaries. For both heating rates, most of the coherent twin boundaries are distributed in recrystallized areas. Figure 20 shows the relationship between the recrystallization percentage and the holding time at 1150°C . The recrystallization percentage of the blue curve, which represents the conventional slow heating process, continuously increases as holding time increases, indicating a steady recrystallization process. In comparison, the recrystallization percentage of fast heating process (the orange curve in figure 20) shows a decrease after 12min, and then a dramatic increase after 36min, indicating an increase in the kinetics of static recrystallization process. The recrystallization rate of 200°C/s heat treatment is faster between 0 and 10min than that of 0.1°C/s at the reheating temperature of 1150°C , and this provides

the driving force to the initial increase of annealing twin density. The synchronous trend at the beginning of the curves in figure 20 and figure 18 indicates that the initiation of the annealing twin boundary is highly related to the beginning of recrystallization. By comparing the curves in these two figures, the second increasing step of annealing twin density takes place when the recrystallization percentage increases higher than about 65%.

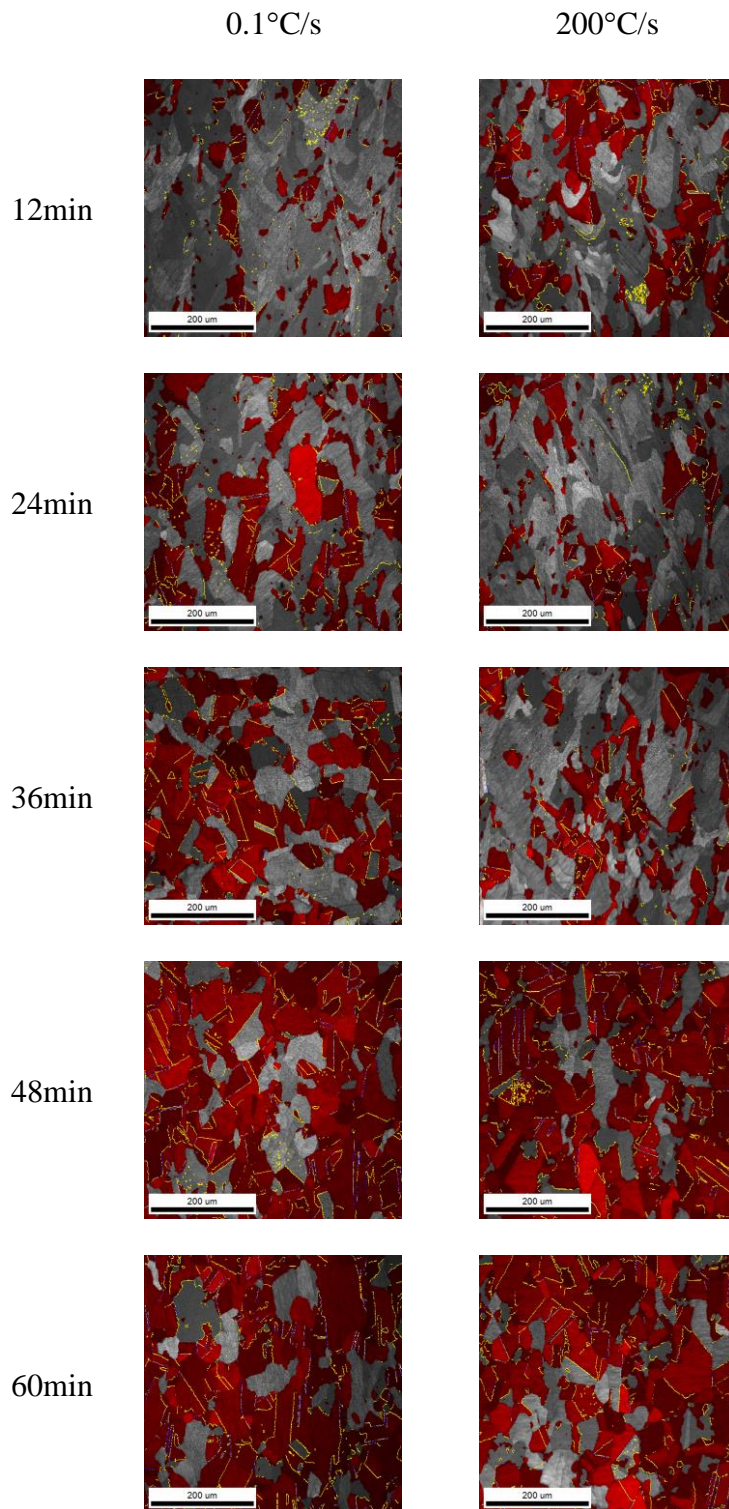


Figure 19. IQ + GOS + Twin boundary at 1150°C

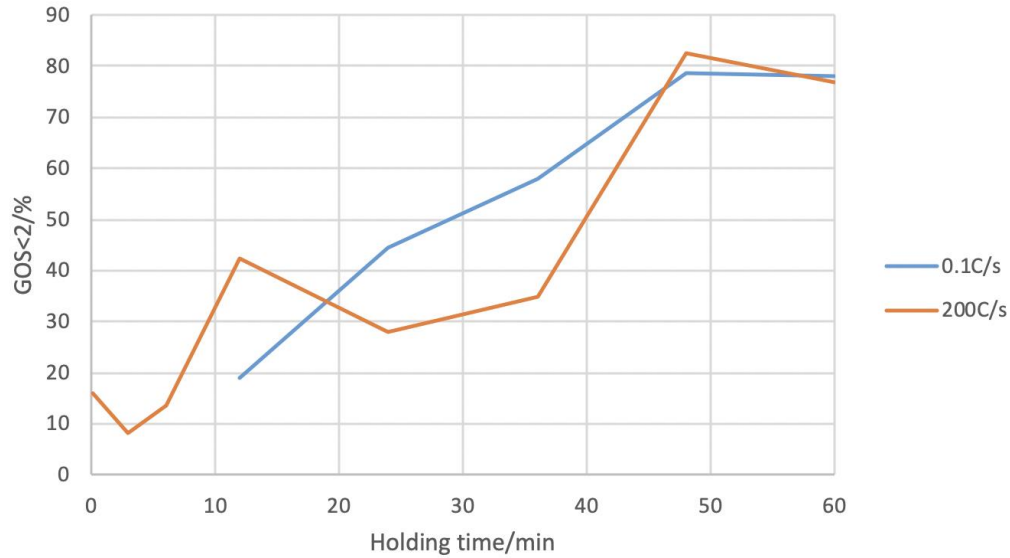


Figure 20. GOS < 2° fraction vs. holding time at 1150°C

In order to investigate the effect of heating rate, 10°C/s and 100°C/s heating rates were also applied at 1150°C holding 12 min. Figure 21 shows the corresponding EBSD results using the same legends as figure 17 and figure 19, and figure 22 shows the comparison of annealing twin density at various heating rates. The results show that faster heating rate leads to finer and more equiaxed microstructure and higher annealing twin density, at the condition of 1150°C reheating temperature and 12 min holding time.

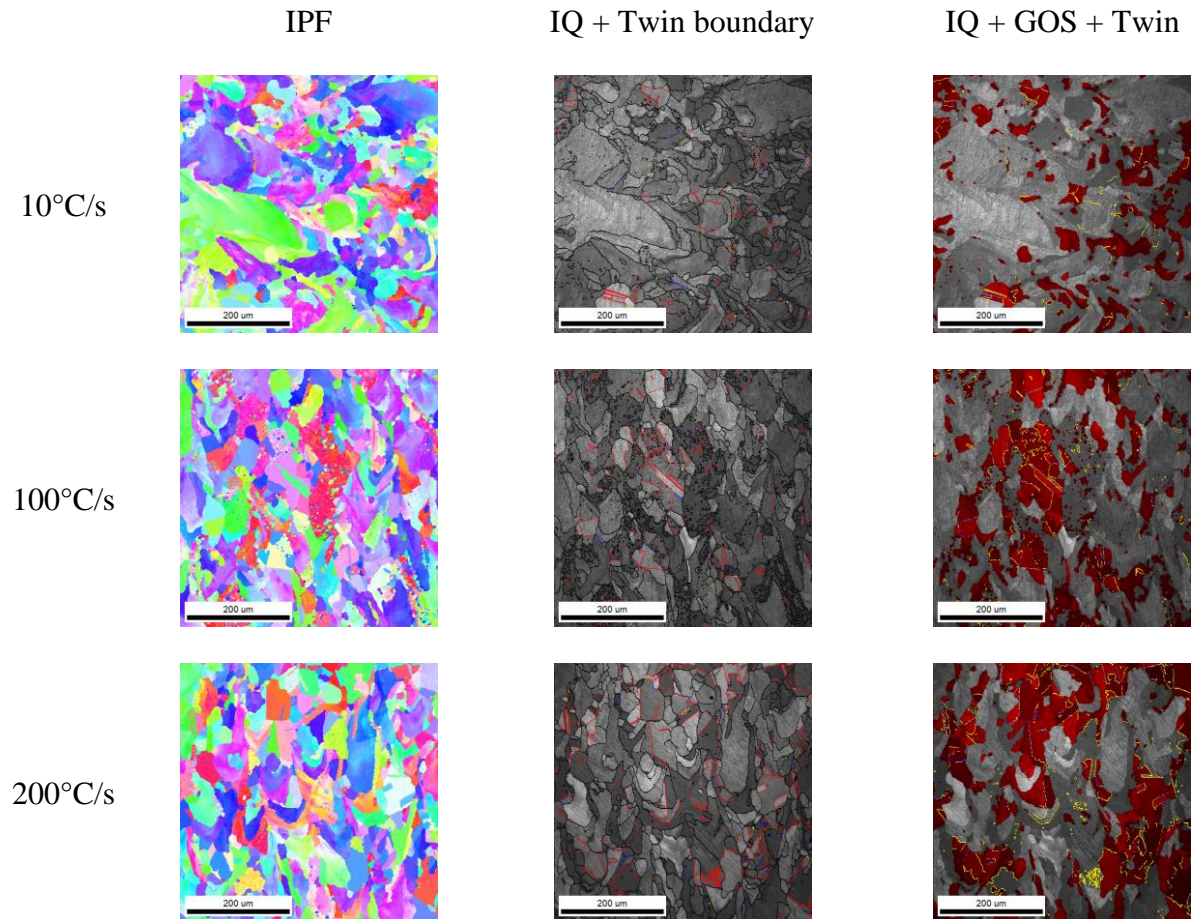


Figure 21. Comparison of heating rates at 1150°C holding for 12min using induction rapid heating

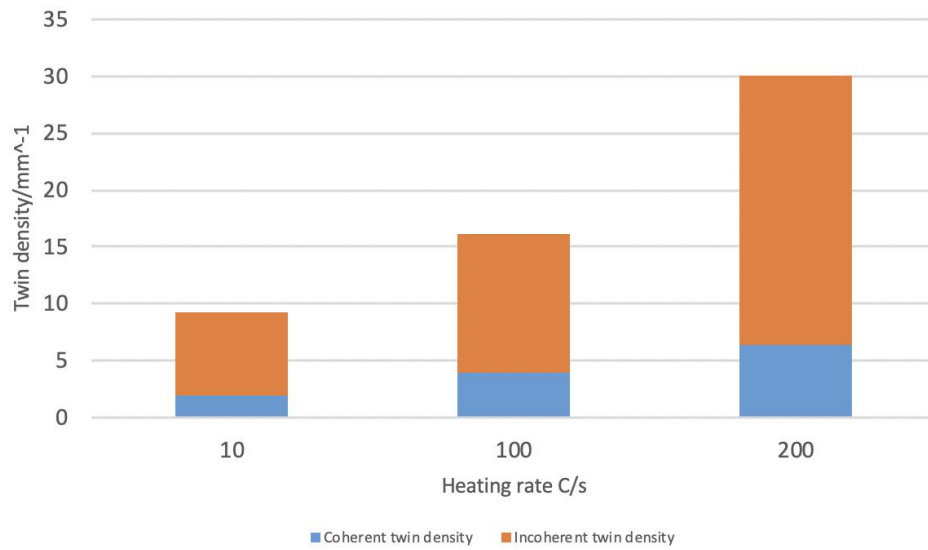


Figure 22. Annealing twin density at different heating rates at 1150°C holding for 12min

In order to investigate the effect of temperature and heating rate, a series of experiments using heating rates of 10°C/s, 100°C/s and 200°C/s were done at 1200°C and 1250°C holding from 3-12min. Figure 23-25 show the IPFs, IQ + Twin boundaries and GOS + IQ + Twin boundaries at 1200°C, respectively. The IPFs in figure 23 showed random crystallographic orientations for all conditions. In figure 24, the black line represents high angle grain boundaries with misorientation > 15°, while the red line, blue line and yellow line highlight $\Sigma 3$, $\Sigma 9$ and $\Sigma 27$ boundaries, respectively. The initiation amount of annealing twin boundaries is higher at higher heating rate, as shown in the first row of figure 24. The amount of annealing twins after 12min holding at 1200°C also increases as the heating rate increases, as shown in the last row of figure 24. This is an interesting result since it seems that at high temperatures and fast heating rates the holding times to obtain an equiaxed (recrystallized) grain size can be reduced. Compared microstructures figure 17 (200°C/s and 60 min at 1150°C) and figure 24 (200°C/s and 12 min at 1200°C). It seems that the thermal conductivity in austenitic stainless steels increases with the reheating temperature. This implies that the diffusion of heat is faster through the cross-section of the sample. In figure 25, the red area represents the area with GOS < 2°. The yellow line highlights the total $\Sigma 3$ boundaries, while the blue line only highlights the coherent twin boundaries. Figure 25 shows that faster heating rate can result in faster recrystallization kinetics, which is consistent with the observations after 1150°C heat treatments. However, abnormal grain growth starts to take place at 1200°C for 12min holding time at 100°C/s and 200°C/s. This can be due to higher grain boundary mobility from elevated temperature and higher thermal stress induced by faster heating rates.

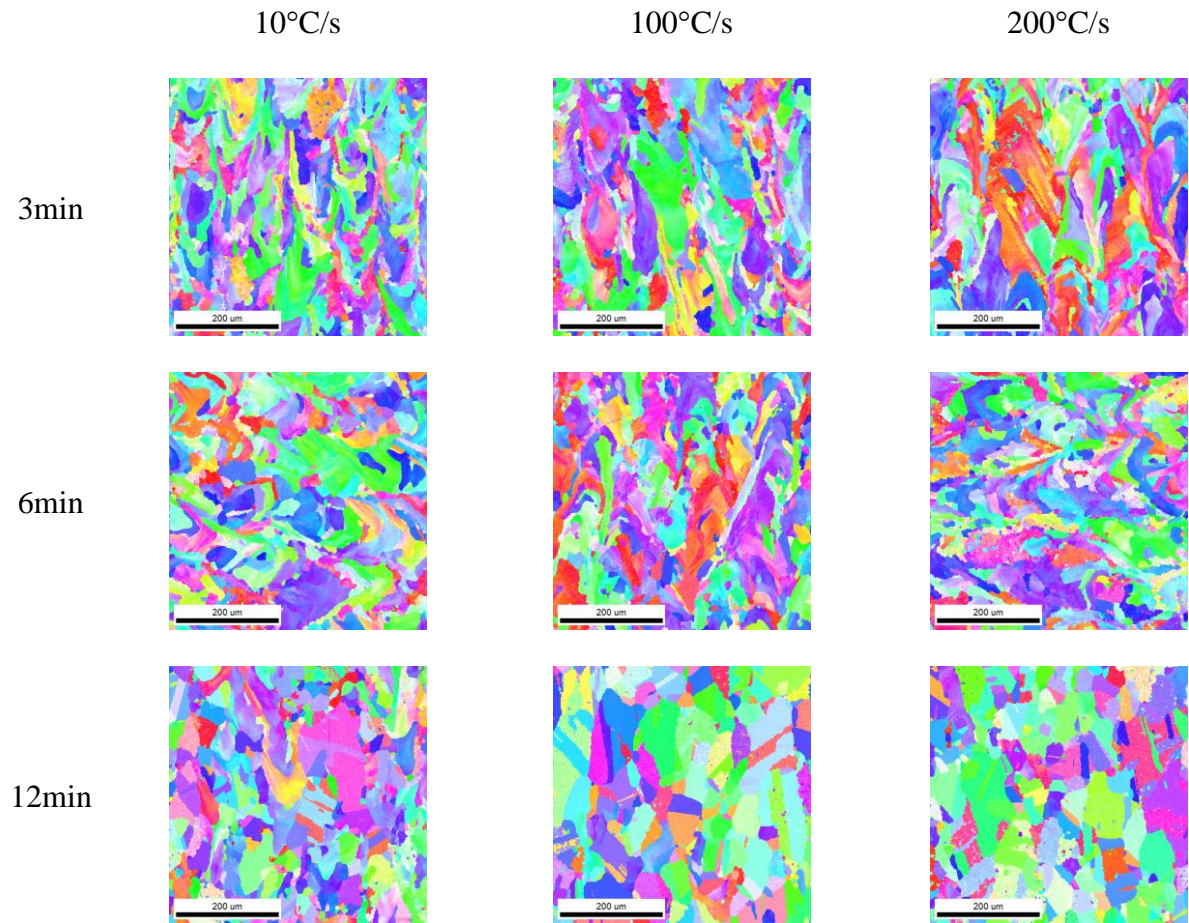


Figure 23. IPFs of samples heat treated at 1200°C with various heating rates and holding times

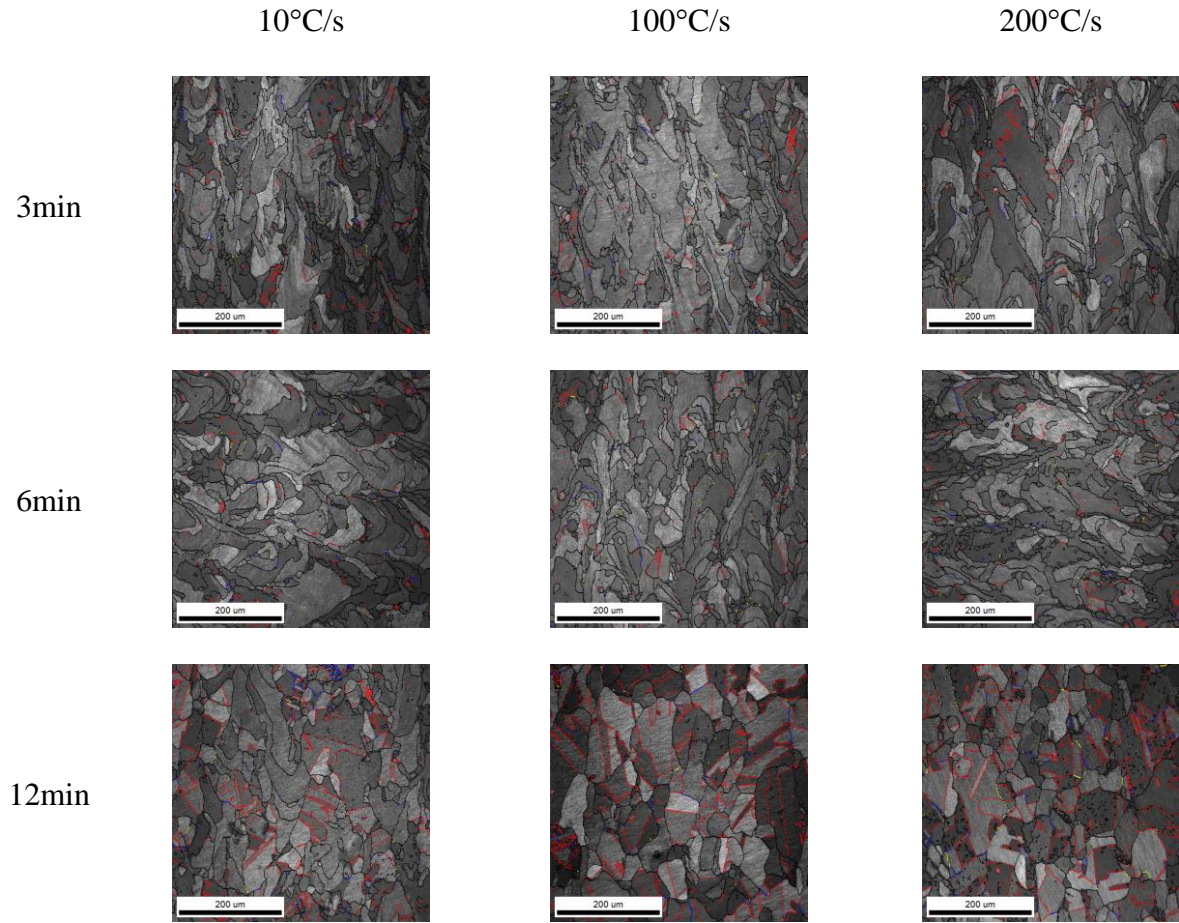


Figure 24. IQ + Twin boundaries of samples heat treated at 1200°C with various heating rates and holding times

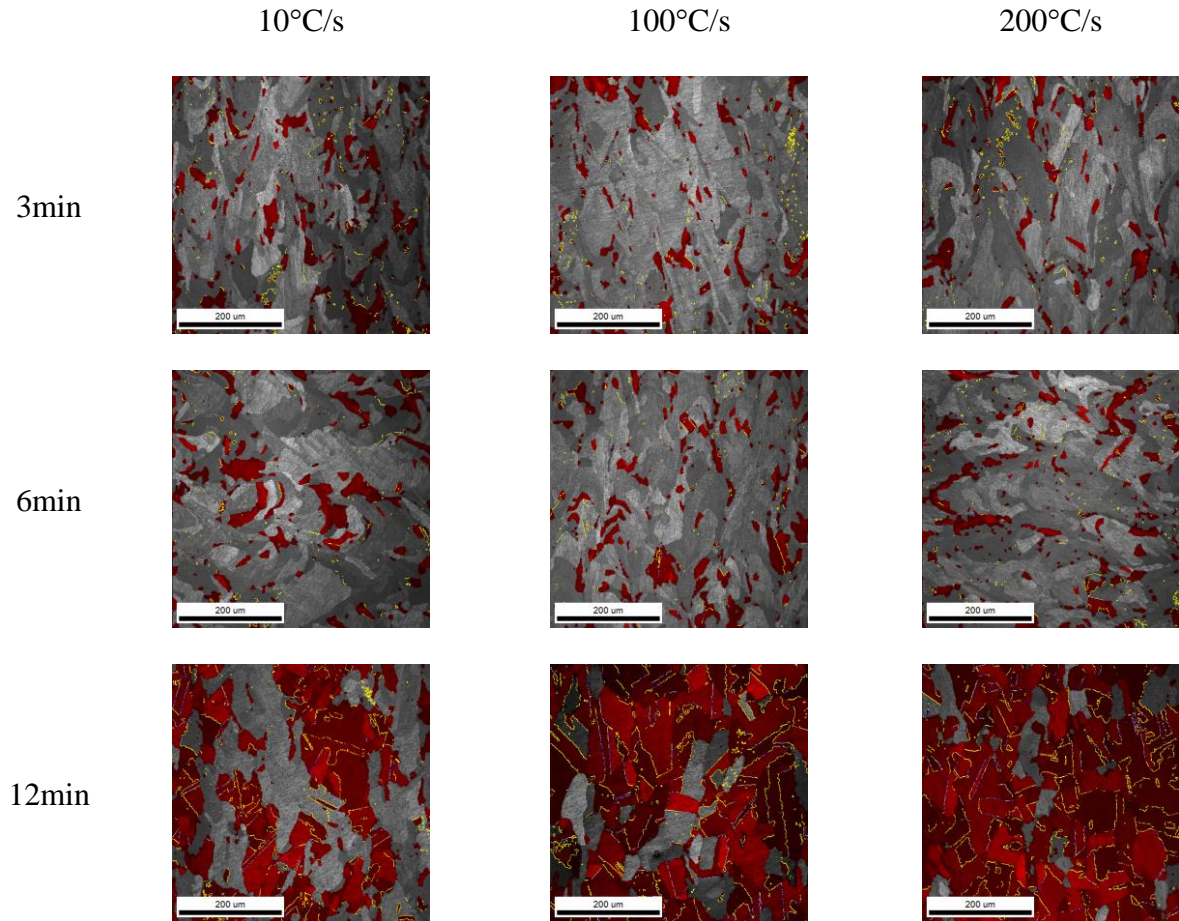


Figure 25. GOS + IQ + Twin boundaries of samples heat treated at 1200°C with various heating rates and holding times

Figure 26 shows the change of coherent and incoherent twin density along holding time at 1200°C at various heating rates. The twin density, i.e. more annealing twin boundaries, as the holding time increases, and faster heating rates (100°C/s and 200°C/s) compared to slower heating rates (10°C/s). However, the total annealing twin density does not show much difference between 100°C/s and 200°C/s heating rates.

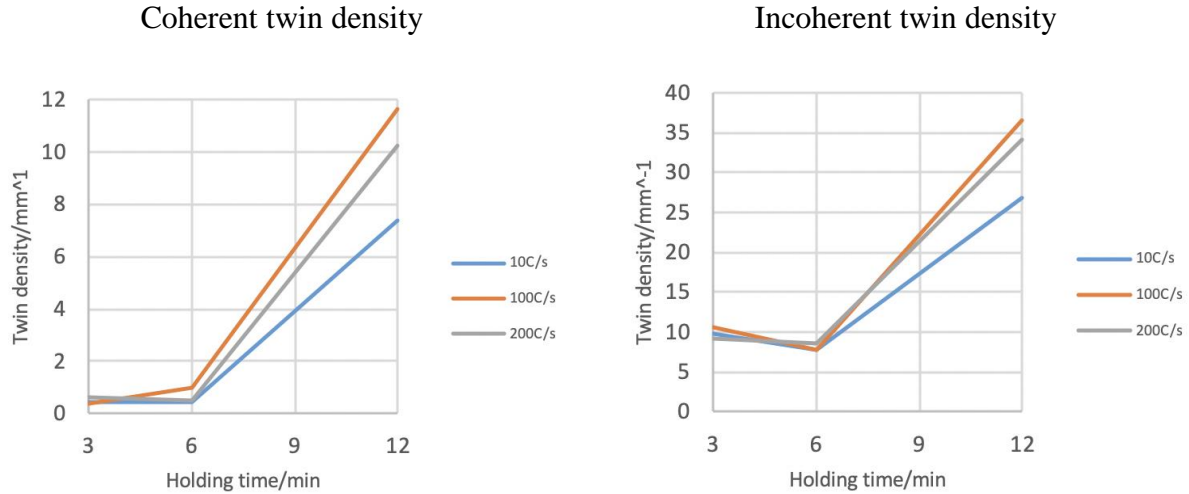


Figure 26. Coherent and incoherent twin density vs. holding time at various heating rates at 1200°C

Figure 27 shows the relationship between the recrystallization percentage ($\text{GOS} < 2^\circ$) and holding time at various heating rates at 1200°C. Similar to the results at 1150°C, faster heating rate results in higher recrystallization rate. The recrystallization percentage is similar between 100°C/s and 200°C/s, and this corresponds to the twin density behavior. Comparing the three curves in figure 27, there is a large increase in recrystallization rate when the heating rate increases from 10°C/s to 100°C/s, but the increase in recrystallization rate is much smaller when the heating rate increases from 100°C/s to 200°C/s. It seems that the effect of the increase of heating rate decreases progressively, hence increasing the heating rate higher than 200°C/s is less efficiency.

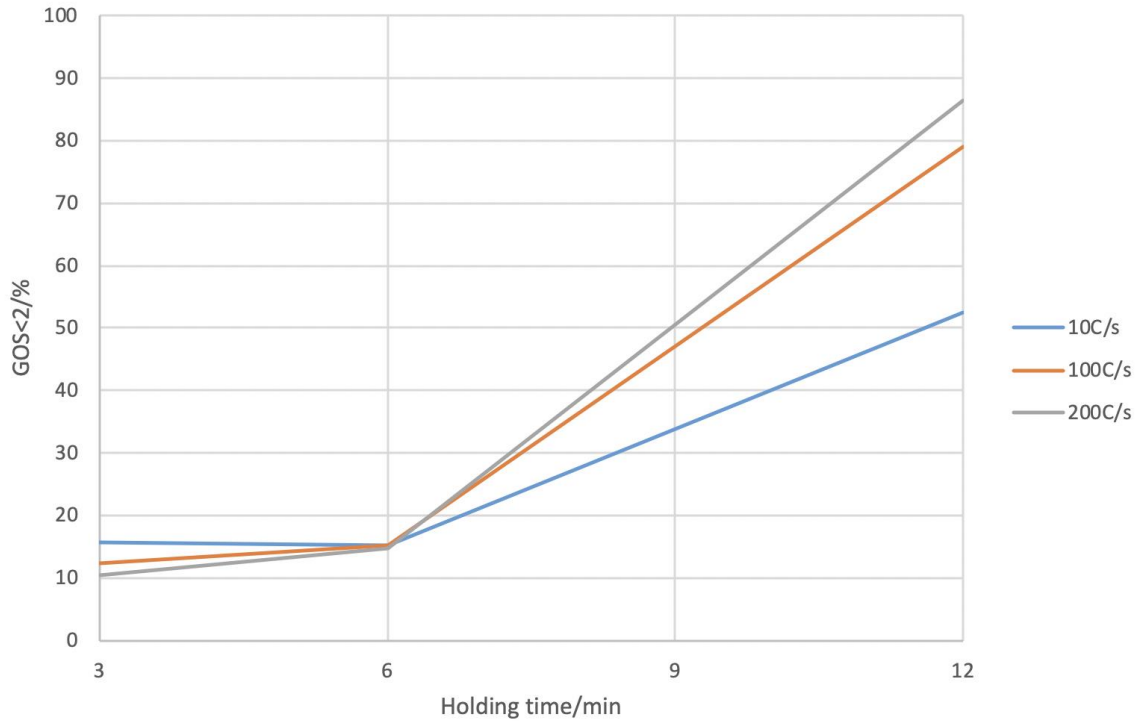


Figure 27. Recrystallization percentage vs. holding time at various heating rates at 1200°C

Figures 28-32 show the same series of results from EBSD scans of samples heat treated at 1250°C holding for 3-12min at various heating rates, as shown in figures 23-27. Being different from 1200°C heat treatments, 200°C/s heating rate showed the highest increase in annealing twin density and recrystallization fraction compared with 100°C/s and 10°C/s. The reason of this behavior is that the process kinetics of recrystallization and grain coarsening is much faster due to the increase of temperature. For example, to reach similar percentage of recrystallization, i.e. 86%, at 1200°C it took 12min while at 1250°C took less than 3min. Thus, using the same time scale at 1200°C and 1250°C does not represent the same stage of the kinetics of the recrystallization process. For example, the recrystallization results at 1150°C in figure 20 are taken as the basis to represent the whole recrystallization process, then the curves at 1200°C in figure 27 show similar trends in the 10-50min at 1150°C, while the curves at 1250°C in figure 32 show the similar trend

as 25-50min at 1150°C. Therefore, the curves at 1250°C are consistent with the trends showing in them at 1150°C and 1200°C, even though they look less regular. The non-monotonically increasing in recrystallization rate with holding time proves again that the rapid heating process using induction heating system is a dynamic process. The microstructure after 6min and 200°C/s heating rate looks finer than it of both 3min and 100°C/s, and 3min and 10°C/s. After 12min holding, the 200°C/s has the coarsest microstructure. This indicates that faster heating rate can provide finer initial recrystallized microstructure, but these finer grains will grow faster if soaking for a longer time. This is also consistent with the observations at 1150°C.

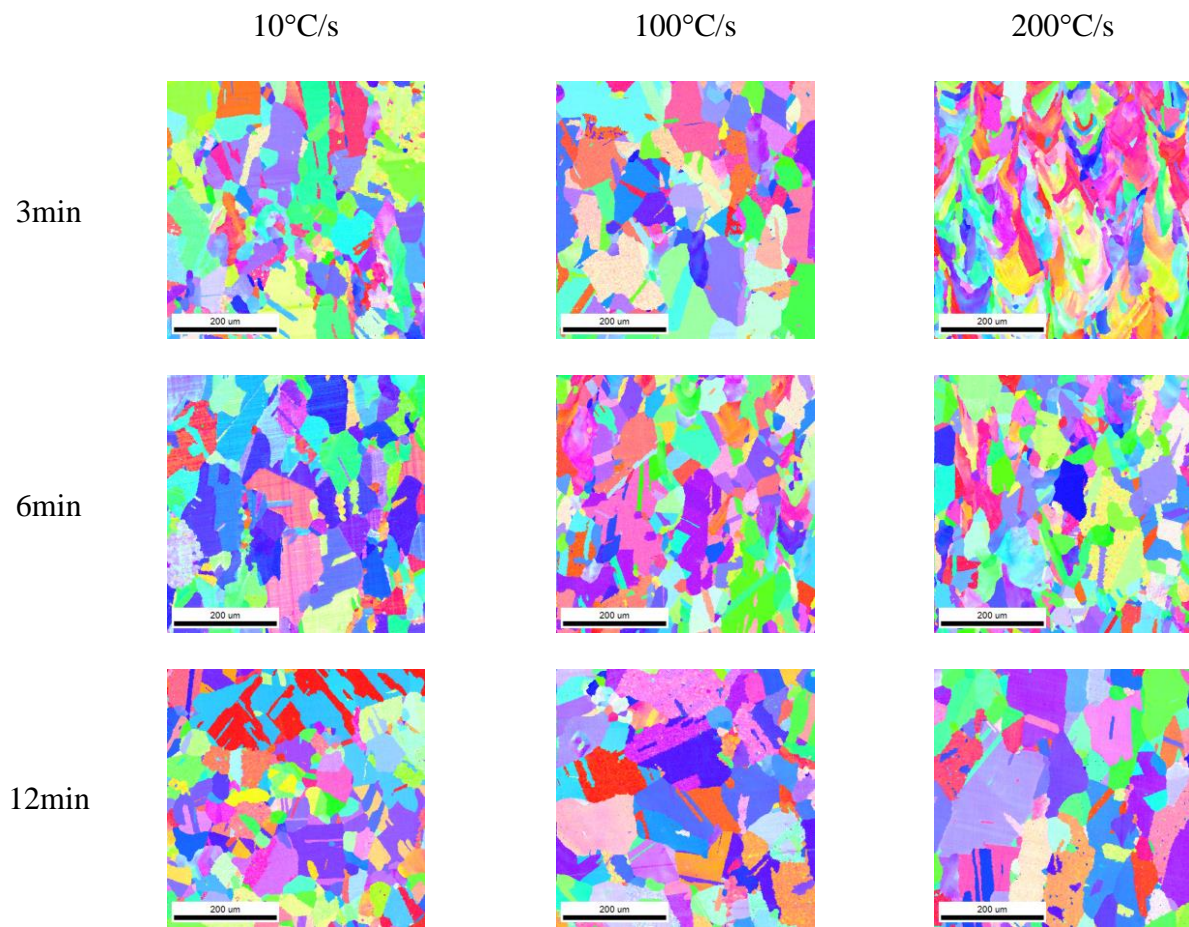


Figure 28. IPFs of samples heat treated at 1250°C with various heating rates

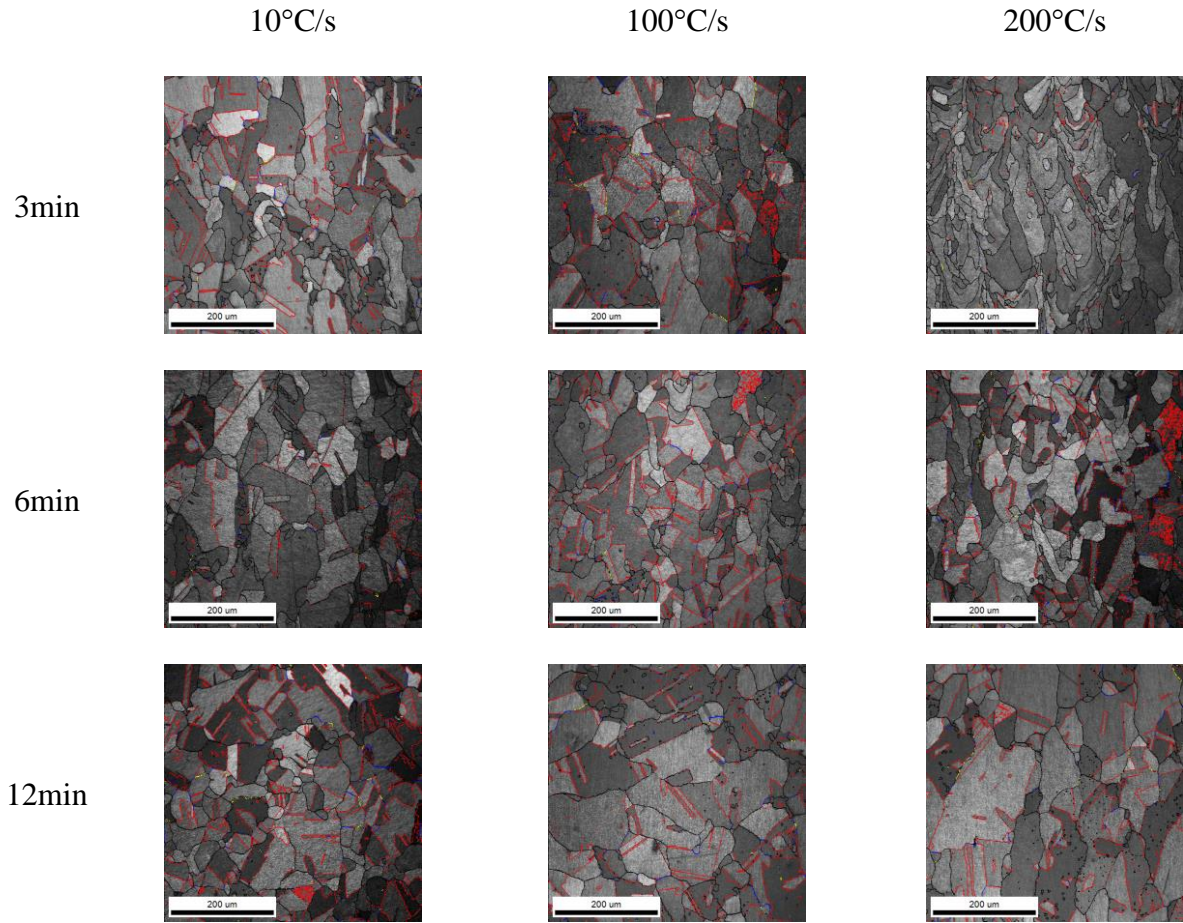


Figure 29. IQ + Twin boundaries of samples heat treated at 1250°C with various heating rates

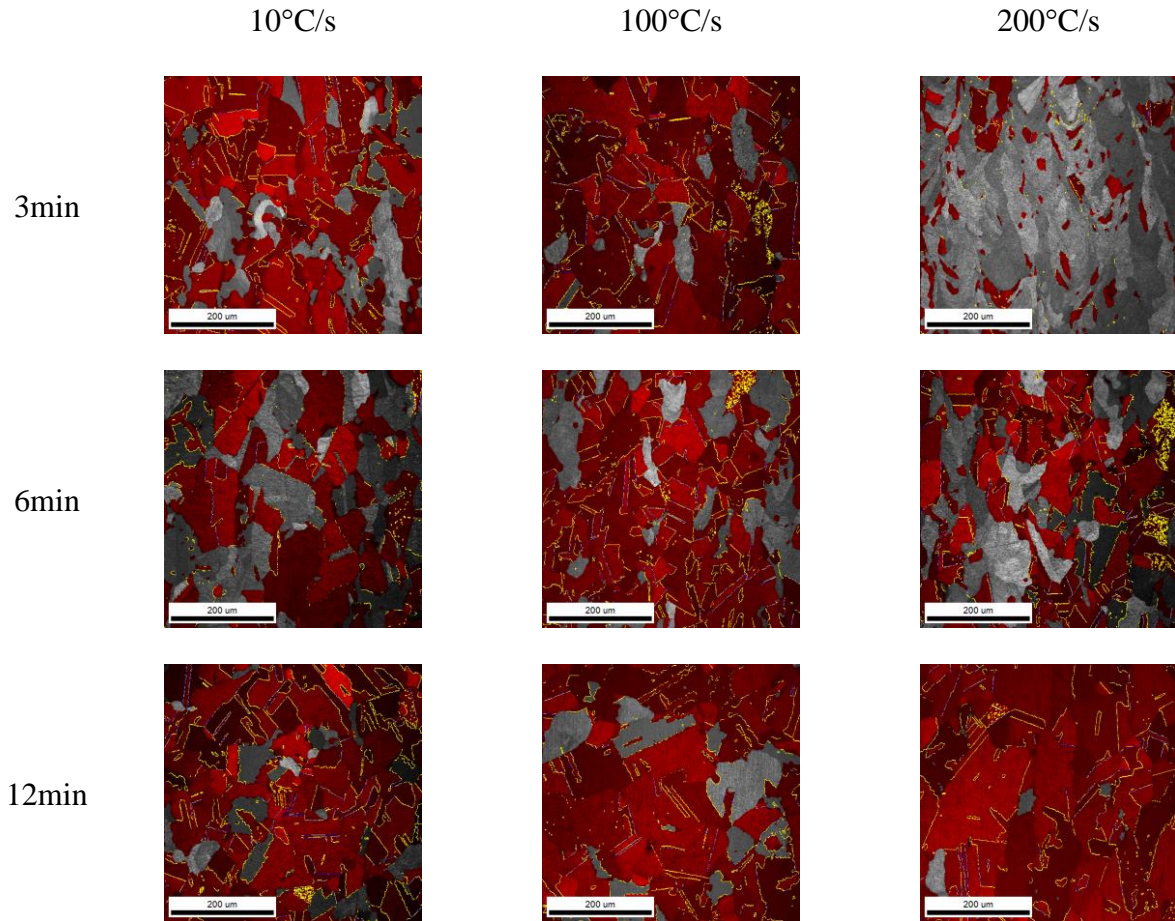


Figure 30. GOS + IQ + Twin boundary of samples heat treated at 1250°C with various heating rates

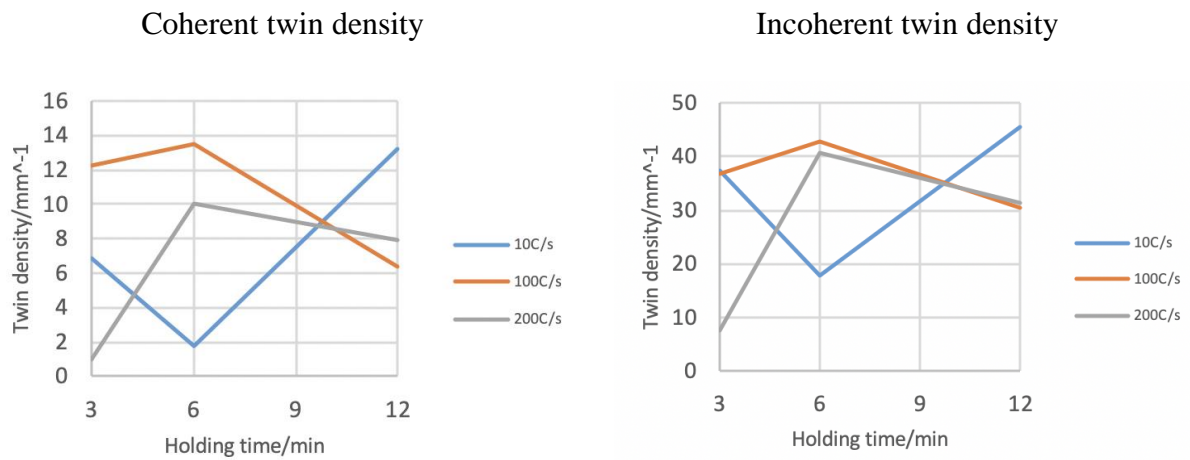


Figure 31. Coherent and incoherent twin density vs. holding time at 1250°C with various heating rates

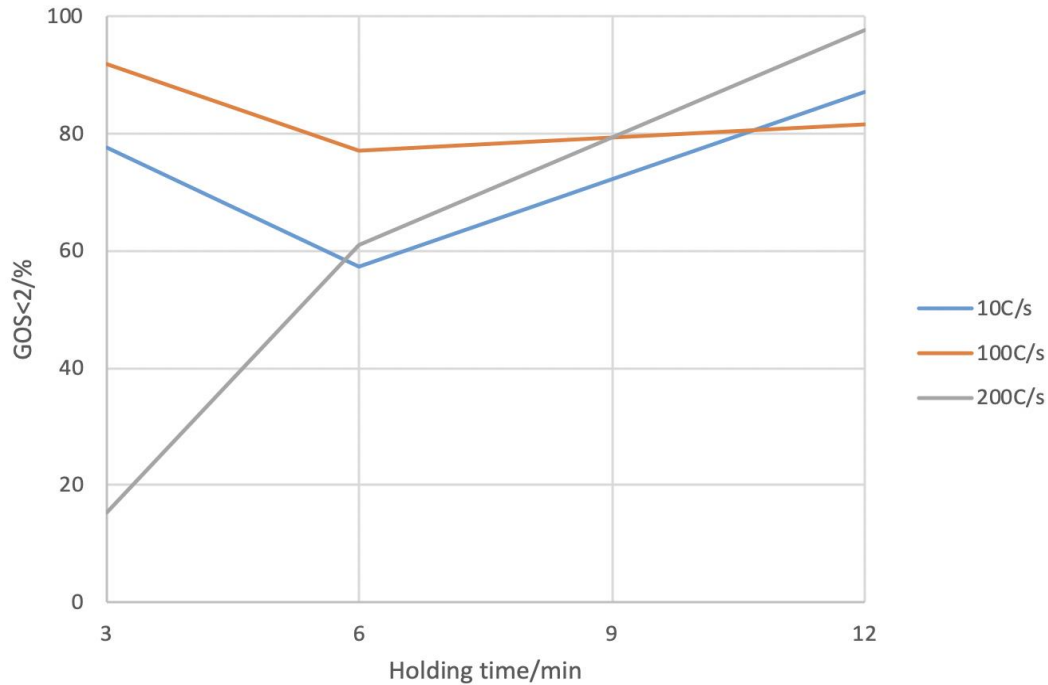


Figure 32. GOS < 2° fraction vs. holding time at 1250°C with various heating rates

4.2.2 Summary

In general, the annealing twin density is highly related to the evolution of microstructure. At 1150°C and 1200°C, the annealing twin density and the recrystallization percentage increase as heating rate increases, while at 1250°C they do not show the same trends. The coherent twin density and incoherent twin density show similar responses to the change of processing parameters.

In all induction rapid heating treatments, the highest coherent twin density is 13.54/mm obtained at 1250°C and 100°C/s holding 6min, and the highest incoherent twin density is 45.59/mm obtained at 1250°C and 10°C/s holding 12min. The highest recrystallization percentage is 97.7% obtained at 1250°C and 200°C/s holding 12min. There are other processing conditions

which also obtain high annealing twin density comparable to the maximum value (higher than 70% of the maximum value), and these conditions are listed in table 3 (where T is the reheating temperature, T' is the heating rate, t is the holding time, CTD is coherent twin density, ITD is incoherent twin density, RXN is recrystallization percentage).

Table 3. Summary of high annealing twin density processing conditions

T (°C)	T' (°C/s)	t (min)	CTD (mm ⁻¹)	ITD (mm ⁻¹)	RXN (%)
1150	200	48	10.99	30.11	82.4
1200	100	12	11.65	36.57	78.9
1200	200	12	10.24	34.06	86.4
1250	10	12	13.26	45.59	87.1
1250	100	3	12.29	36.68	91.8
1250	100	6	13.54	42.85	77.2
1250	200	6	10.08	40.75	60.9

4.3 Grain Size Measurements

Grain size represents the average scale of a microstructure, and it is highly related to the strength of a material, such as the relationship between the yield strength and grain size described by the Hall-Petch equation[101]:

$$\sigma_y = \sigma_0 + \frac{k_y}{\sqrt{d}} \quad (4-2)$$

where σ_y is the yield strength, σ_0 is a material constant for starting stress of dislocation movement, k_y is the strengthening coefficient, and d is the average grain size.

In this study, the size of a grain is defined as its equivalent diameter of a circle with the same area as the grain. Since the specimens cover various stages in recrystallization process, the size of the grains in one sample could be a bi-modal distribution with a few of large grains and a lot of small grains, and the average value of grain size is no longer proper to represent the scale of microstructure. In order to make the grain size value representative to the corresponding microstructure, the grain size was calculated according to area average method with the consideration of the 'area weight' of each grain. It means to multiply the diameter of each grain by the area of the grain, and then sum them together and divided by the total areas of all grains. In this way, the calculated grain size should be the average of a total consideration of all grains, and it should be close to the grains occupying the highest area fraction, which should be representative enough. For each sample, more than 100 grains were measured in this study. Coherent twin boundaries were not considered as grain boundaries in this measurement since they are stable and less likely to move due to their low energy state.

Figure 33 shows the relationship of grain size and holding time at various temperatures and heating rates. The 200°C/s fast heating treatment results in a smaller grain size than conventional slow heating treatment at 1150°C, indicating the ability of induction rapid heating to refine the microstructure. For all induction fast heating treatments, generally grain size increases as holding time and temperature increases. Some small decreasing trends at short holding times in the curves shows that the process is dynamic, and the decrease can be due to formation of new grains. Faster heating rates can provide finer grain size during the early stage of recrystallization, but the grain size is sensitive to holding time. Once the holding time gets too long, the finer grains formed

through faster heating rates will rapidly become coarser, which will decrease the strength of the material.

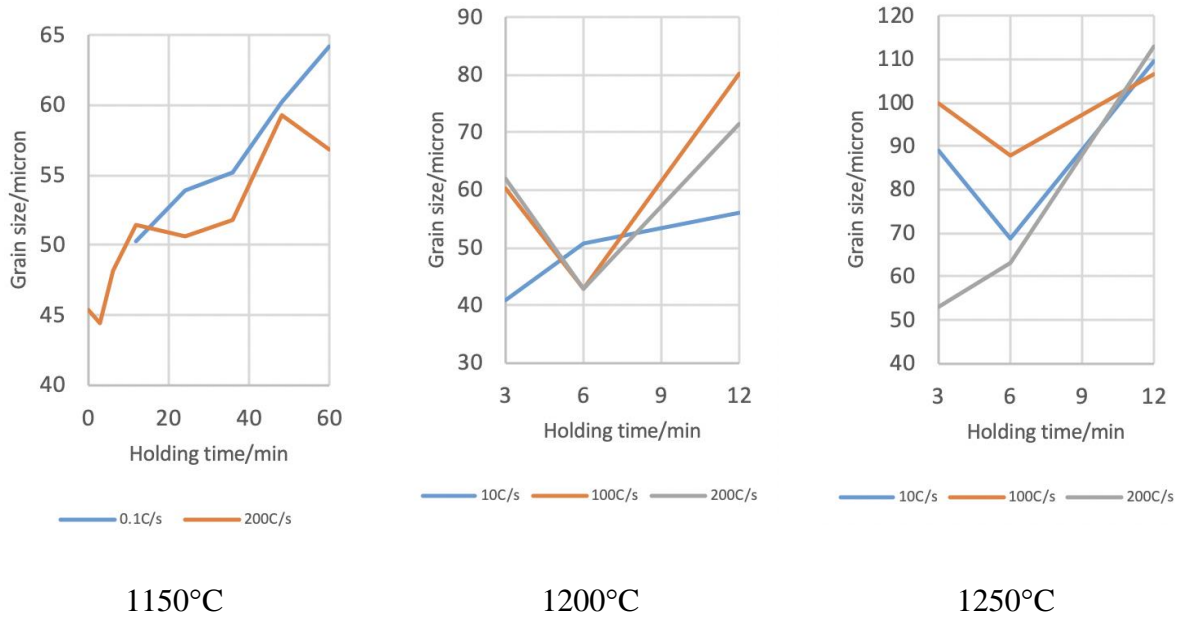


Figure 33. Grain size vs. holding time at various temperatures and heating rates

4.4 Microhardness Measurements

Microhardness was also measured in Vicker’s criterion for each sample to evaluate the influence of microstructure to strength. For each sample, 12-15 points were measured, and the average value of VHN and standard deviation were calculated the results. The VHN of as-fabricated SLM SS316L specimen is 221.38, with a standard deviation of 7.8.

Table 4 and figure 34 show the microhardness results of samples heat treated at 1150°C. The Δ VHN means the difference between the as-fabricated specimen and the heat treated specimens. For both heating rates, the microhardness shows a decreasing trend as holding time increases, which makes sense since the microstructure releases the residual stress and transforms

from a stress-residual structure to a stress-free structure during heat treatment. In addition, the microstructure is undergoing recrystallization and the grains getting coarser. However, this microstructure will exhibit less anisotropy than the as-deposited microstructure. For the samples reheated at 0.1°C/s using a conventional furnace heat treatment, there is an increase of microhardness at 48min, while for the 200°C/s induction rapid heating there are two places of increasing of microhardness at 12min and 48min. By comparing the hardness results with the twin density results in figure 18, the increases in microhardness are found to correspond to the increases of annealing twin boundaries density. This indicates the contribution of annealing twin formation and development to strength of the material. In general, 200°C/s rapid heating provides higher microhardness values than the conventional furnace heat treatment with slow heating rate (0.1°C/s). This is due to the combination of finer grain size and higher twin boundary density.

Table 4. VHN value of specimens heat treated at 1150°C

	As fabricated	3min	6min	12min	24min	36min	48min	60min
0.1°C/s	221.38			201.38	178.81	170.60	180.57	170.26
Δ VHN				20.00	42.57	50.78	40.81	51.12
200°C/s		198.56	193.94	197.42	186.44	176.43	188.60	171.15
Δ VHN		22.82	27.44	23.96	34.94	44.95	32.78	50.23

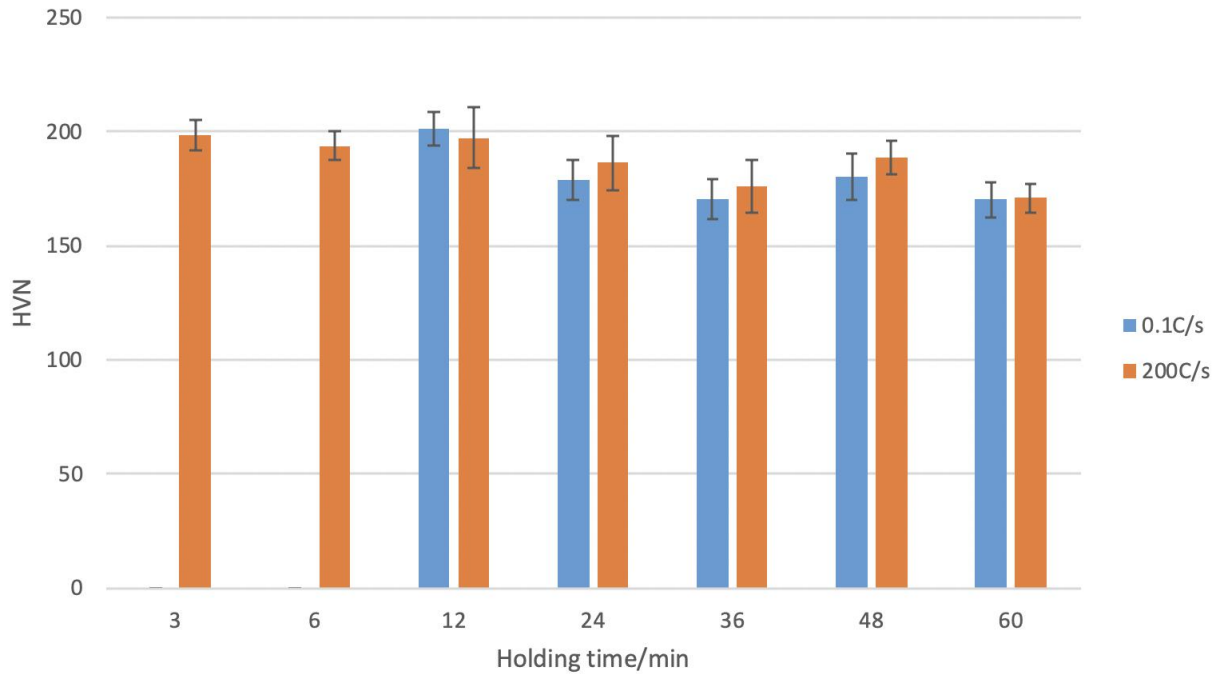


Figure 34. Microhardness and standard deviation of samples heat treated at 1150°C

Table 5 and figure 35 show the microhardness results of samples heat treated at 1200°C via induction heating system with different heating rates. The Δ VHN means the difference between the as-fabricated specimen and the heat treated specimens. At this temperature, 200°C/s heating rate provides the highest microhardness at the beginning of heat treatment and also after recrystallization at 12min. The 100°C/s heating rate has a sudden drop of microhardness at 12min. There is a strong correlation between twin boundary density and grain size. That is, when full recrystallization takes place, the grain size starts to coarsen and the twin boundary density starts to decrease. These metallurgical events are well understood in the literature, what is not well-known is the effect of heating rate on recrystallization and twin boundary density. The understanding of these reactions is essential to decrease the anisotropy and improve the performance of 3D printed metallic materials.

Table 5. VHN values of samples heat treated at 1200°C

	As fabricated	3min	6min	12min
10°C/s	221.38	197.32	195.28	184.60
Δ VHN		24.06	26.10	36.78
100°C/s		195.43	196.26	163.76
Δ VHN		25.95	25.12	57.62
200°C/s		201.85	194.51	186.14
Δ VHN		19.53	26.87	35.24

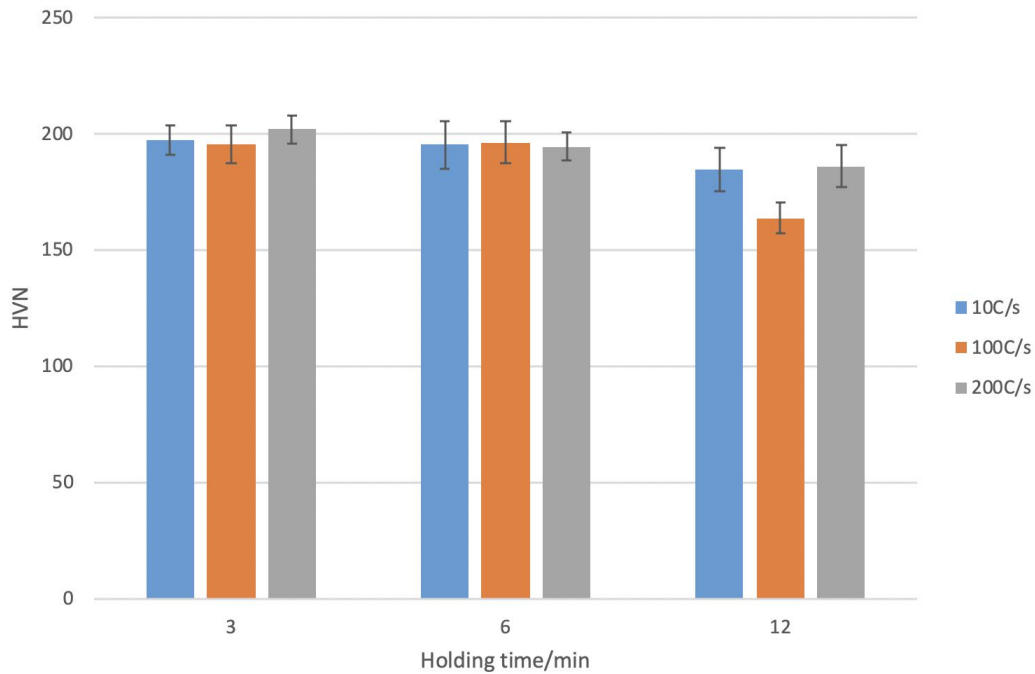


Figure 35. Microhardness and standard deviation of samples heat treated at 1200°C

Table 6 and figure 36 show the microhardness results of samples heat treated at 1250°C.

The Δ VHN means the difference between the as-fabricated specimen and the heat treated specimens. At this temperature, the microhardness value is lower than the previous two

temperatures. Even though the structures are most recrystallized and generated high annealing twin density, grain coarsening starts after 3min short holding time, and this leads to the decrease of microhardness.

Table 6. VHN values of samples heat treated at 1250°C

	As fabricated	3min	6min	12min
10°C/s	221.38	173.93	168.52	165.57
Δ VHN		47.45	52.86	55.81
100°C/s		167.16	164.29	160.51
Δ VHN		54.22	57.09	60.87
200°C/s		184.49	180.90	161.34
Δ VHN		36.89	40.48	60.04

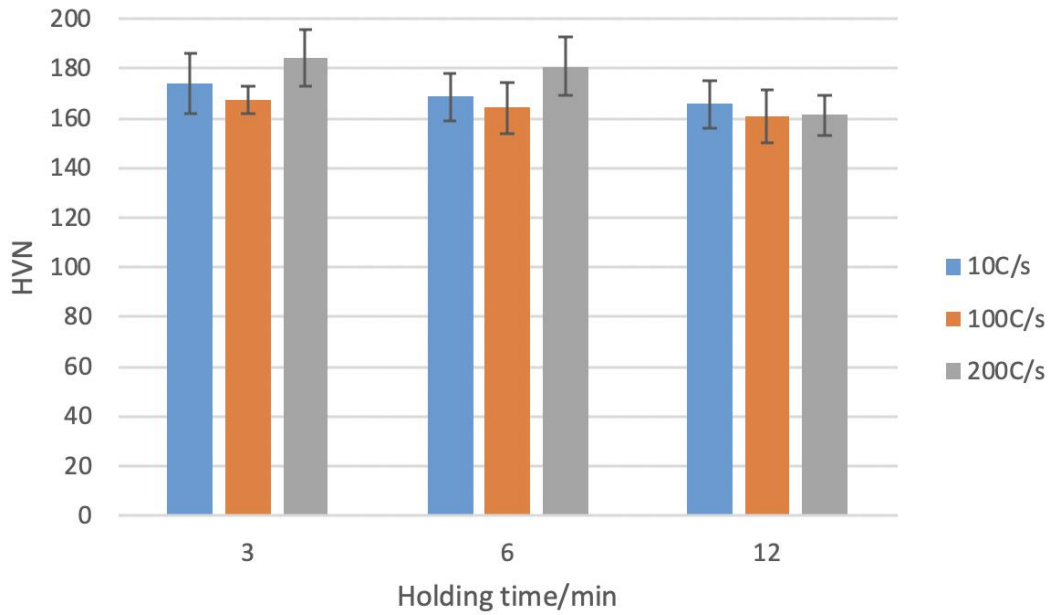


Figure 36. Microhardness and standard deviation of samples heat treated at 1250°C

4.4.1 Summary

In general, as-expected microhardness decreases as temperature and holding time increases during heat treatments. The microhardness value is an overall reflection of the influence from both the annealing twin boundaries and the grain size. Grain coarsening can severely decrease the microhardness, and in this situation high annealing twin density will not help to maintain the strength of the material.

4.5 Result Summary of Best Processing Conditions

This summary is trying to provide a general consideration of microstructure consisting of annealing twin density, grain size and microhardness. In table 3 in section 4.2.2, seven optimal conditions with high annealing twin densities were listed. Table 5 shows a comparison of grain size and microhardness values between these conditions, where GS is short for grain size, and VHN represents the Vicker's microhardness number.

Table 7. Comparison of grain size and microhardness values between processing conditions with high annealing twin density

Condition No.	T(°C)	T'(°C/s)	t(min)	CTD(mm ⁻¹)	ITD(mm ⁻¹)	GS(μm)	VHN
1	1150	200	48	10.99	30.11	59.24	188.60
2	1200	100	12	11.65	36.57	80.24	163.76
3	1200	200	12	10.24	34.06	71.40	186.14
4	1250	10	12	13.26	45.59	109.56	165.57
5	1250	100	3	12.29	36.68	99.75	167.16
6	1250	100	6	13.54	42.85	87.99	164.29
7	1250	200	6	10.08	40.75	63.12	180.90

From table 7, it is clear that both grain size and annealing twin density contribute to the strength of the specimen. For example, condition 2 has a higher twin density than condition 1, but it also has a much larger grain size than condition 1 which leads to a lower hardness. Condition 4 has a larger grain size than condition 2, but it also has a larger annealing twin density than condition 2, and their hardness values are comparable. Condition 1, 3 and 7 show the highest microhardness values in the seven conditions with high annealing twin density, and the corresponded processing parameters are highlighted in red color in table 7. All three best conditions are at the maximum heating rate (200°C/s) applied in this study, and this clearly shows the contribution of fast heating rate to obtain good annealing twin density and good strength.

5.0 Discussions

5.1 Annealing Twin Formation in Induction Rapid Heating

According to the results listed in chapter 4, annealing twin boundaries make contribution to the strength of the material. Thus, it is important to understand the impact of induction heating on annealing twin formation and its development. As described in the literature review in chapter 2, annealing twin formation can be related to many factors, such as temperature, grain boundary migration velocity, boundary energy, etc., and these twin boundaries can be formed during recovery, recrystallization and grain growth. The formation of the annealing twin boundaries is a result of grain boundary migration and the preference of the system to stay at a low energy status.

5.1.1 Annealing Twin Formation Mechanisms

As shown in chapter 4, the increasing of annealing twin density seems to be strongly related to the kinetics of recrystallization. This observation is illustrated in figure 37. The blue and orange curves in figure 37 represents the relationship between the recrystallization fraction and the length density of coherent twin density and incoherent twin density, respectively. The green curve represents the relationship between the recrystallization fraction and the number of coherent twin boundaries per grain (N_G). This relationship was calculated using the following equation:

$$N_G = \frac{N_2 - N_1}{N_1} \quad (5-1)$$

where N_1 represents the number of grains without considering twin boundaries as grain boundaries, and N_2 represents the number of grains by considering twin boundaries as grain boundaries. The number of coherent twin boundaries per grain increases as the recrystallization fraction increases, and it increases from about 0.2 to 0.5 during the 200°C/s rapid heating at 1150°C. Both coherent and incoherent twin density increases as the recrystallization fraction increases, but the increasing rate drops between about 42%-78% recrystallization. This is contrary to the previous studies in FCC materials where the annealing twin density increases as recrystallization fraction increases in an exponential relationship[80, 102]. This can be explained by the dynamic process of induction rapid heating, and figure 38 clearly shows the dynamic property of the process by showing the GOS distribution of various holding times of samples heat treated at 200°C/s at 1150°C.

In figure 38, the curve for 6min has a large spread from 1°-6° in GOS value, indicating that most of the areas are not under recrystallization. The curve for 12min shifts to the left compared with the 6min curve, indicating the increasing fraction of recrystallization. The 24min curve contains lower area fraction at low GOS value and it spreads the GOS value range again, suggesting that part of the sample become under strain again due to the thermal stress, which proves the dynamic property of induction rapid heating process. The curve of 48min holding time narrows the spread in GOS value to a range of 0-3°, which means most of the areas are under recrystallization. However, the small peaks between 3-5° show that the sample is still under the load of thermal stress.

Since the induction rapid heating is a dynamic process, it is less likely to relate the annealing twin density to recrystallization fraction in a simple way. The formation of annealing twin boundaries needs to be further studied.

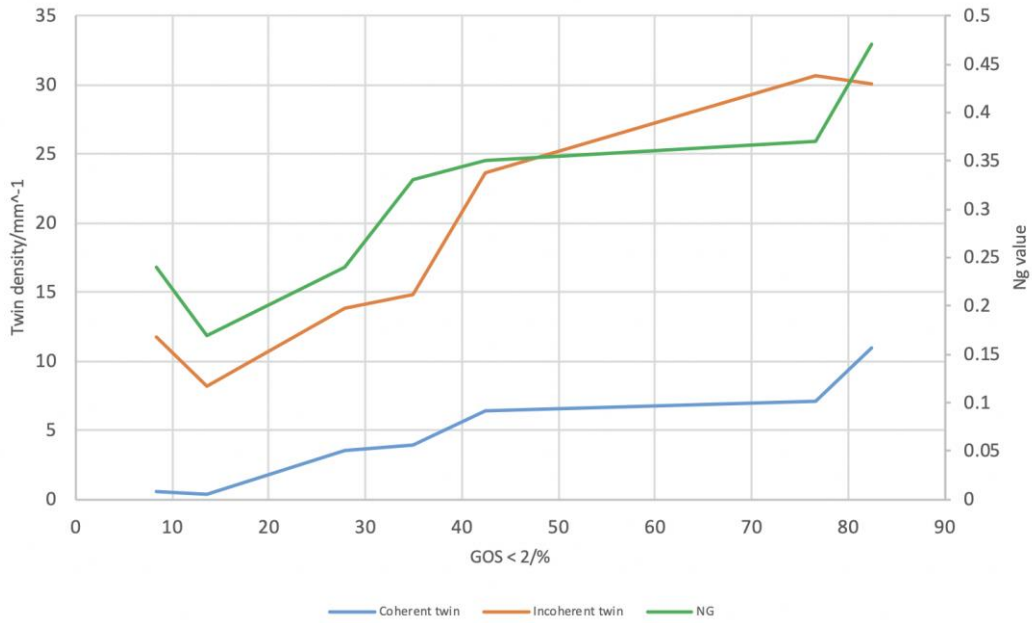


Figure 37. The relationship between recrystallization fraction and twin density at 1150°C, 200°C/s heating rate

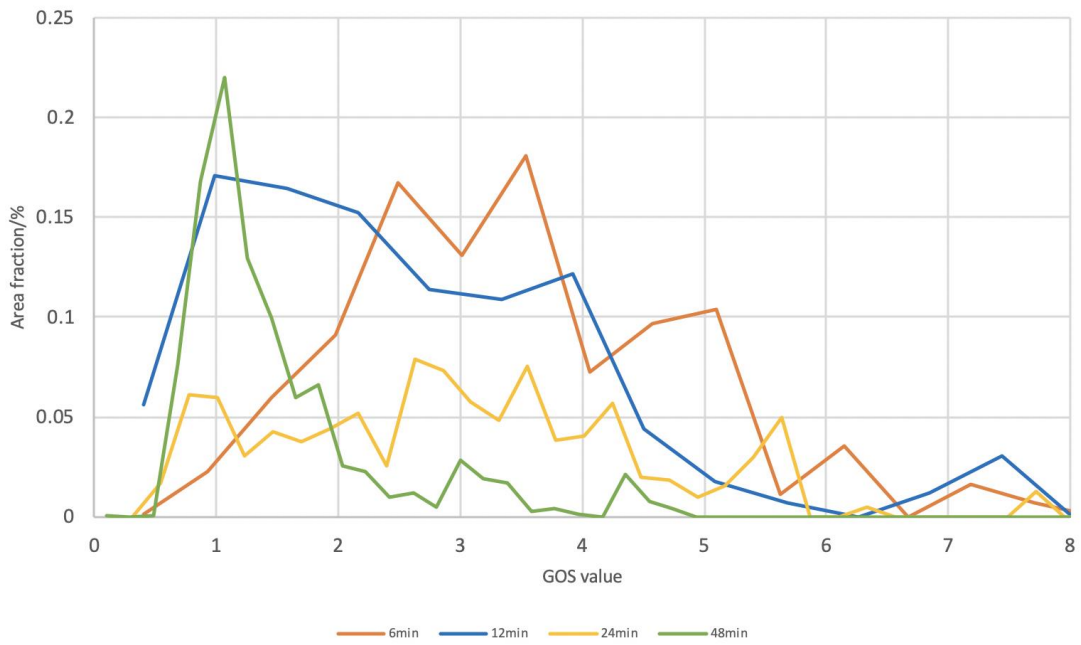


Figure 38. GOS distribution for samples heat treated at 200°C/s at 1150°C for 6, 12, 24 and 48min

Figure 39 shows how the annealing twin density and length fractions of low angle grain boundaries (LAGBs) and high angle grain boundaries (HAGBs) change with holding time for

200°C/s rapid heating at 1150°C. In this study, grain boundaries with misorientation angle $< 15^\circ$ are defined as LAGBs and those with misorientation angle $> 15^\circ$ are defined as HAGBs. Since the investigating object of this study is annealing twin boundaries, all $\Sigma 3$ boundaries have been excluded from HAGBs. Recalling from figure 20 in section 4.2.1, there are two steps of annealing twin density increasing during the rapid heating process. The curves in figure 39 shows that the first increasing step of annealing twin density is along with a decreasing in fraction of LAGBs and a small increasing in fraction of HAGBs, indicating that LAGBs change to annealing twin boundaries and HAGBs at the early stage of rapid heating process. This trend suggests that sub-grain growth may occur at the beginning of the heat treatment, and part of the LAGBs become HAGBs during sub-grain boundary migration. The annealing twin boundaries can then be formed from the migration of HAGBs during this period. Figure 33 in section 4.3 shows that the grain size slightly increases at the early stage, indicating that HAGB migration takes place, which supports the possibility of annealing twin formation due to migration of HAGBs.

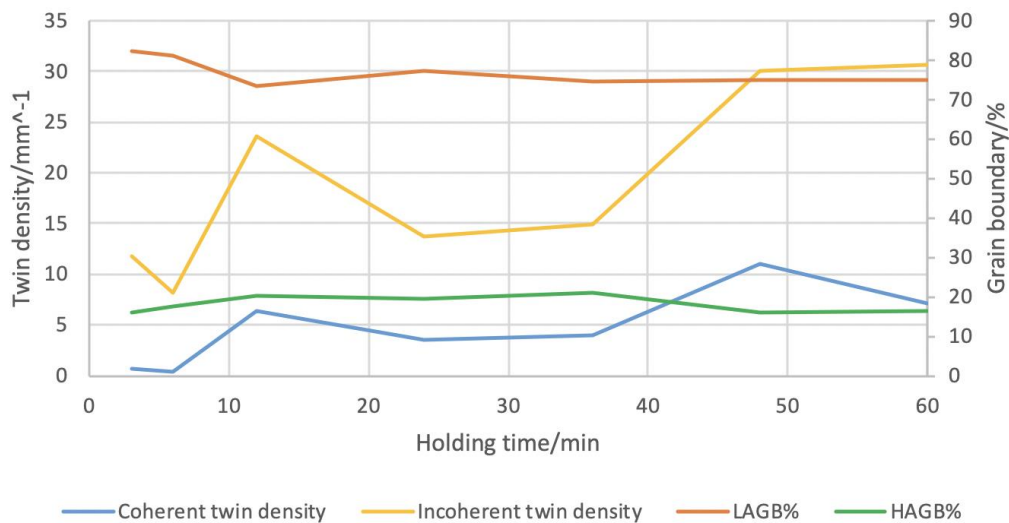


Figure 39. Annealing twin density and length fractions of LAGBs and HAGBs vs. holding time for 200°C/s rapid heating at 1150°C

Figure 40 shows the geometrically necessary dislocation (GND) density distribution map with highlighted total $\Sigma 3$ boundaries and coherent twin boundaries for 200°C/s rapid heating treatment at 1150°C holding from 3-12min. The GND density is calculated from the local misorientations according to D.P. Field and colleagues[103]. Standard preset sets of slip systems are entered according to the crystal structure, and the calculation considers both edge and screw dislocations. This approach does not consider misorientations larger than 15° in the calculation of GND. The GND density can be regarded as the lower bound of the statistically stored dislocation density in the sample, and the value is inversely proportional to the step size during acquisition. The relationship between the GND density and the real dislocation density is illustrated in A.C. Leff's work[104]. It can be assumed that the GND density is approximately proportional to the statistically stored dislocation density. In figure 40, the white-to-red background color represents the GND density from low to high, and the maximum value of the GND density is $10^{15}/\text{m}^2$. The black line highlights HAGBs, while the green and blue lines highlight $\Sigma 3$ boundaries and coherent twin boundaries, respectively. At the early stage of rapid heating process, the incoherent $\Sigma 3$ annealing twin boundaries (the green lines not overlapping the blue lines) form inside grains or from HAGBs. The formation inside grains can be resulted from sub-grain rotation and growth, and the formation from HAGBs could be due to HAGB migration. Being different from incoherent twin boundaries, most of the coherent twin boundaries (blue lines) form from HAGBs at areas with high GND density, and there are loss of dislocations in those grains where the coherent twin boundaries form. This is consistent with Y. Jin and colleagues' research[79] that annealing twin boundaries form at boundaries migrating into strained regions. According to some other researches done in similar FCC materials such as Cu and Ni based alloy[105, 106], this annealing twin

formation mechanism could be explained by the growth accident model which is described in Chapter 2.

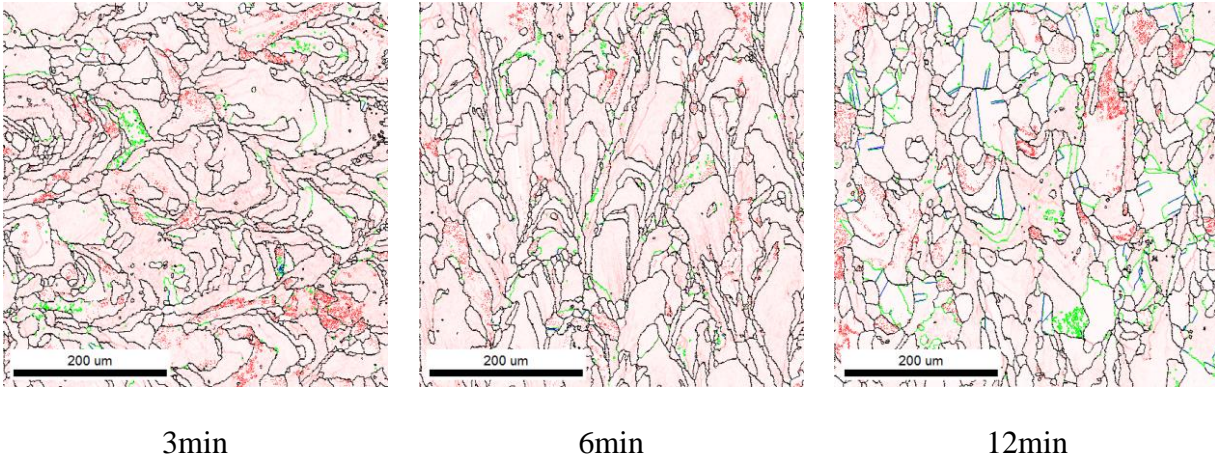


Figure 40. GND density distribution map with highlighted twin boundaries for samples heat treated at 200°C/s at 1150°C holding from 3-12min

Figure 41 shows the GND density map with highlighted annealing twin boundaries at 200°C/s rapid heating at 1150°C holding for 24min, 36min and 48min, the legends on this figure are the same as in figure 40. The areas highlighted with a red circle in samples after holding for 24min and 36min represent annealing twin formation due to grain boundary dissociation. Based on this observation, a grain boundary with high energy, i.e. HAGB decomposes into a coherent twin boundary, an incoherent twin boundary, and a newly formed grain boundary with lower energy. This agrees with the grain boundary dissociation model of annealing twin formation by Meyers and Murr[72]. A simple illustration of this mechanism is shown in figure 42. With two adjacent grains A and B, the grain boundary AB (the black boundary) decompose into a coherent twin boundary (the green boundary), an incoherent twin boundary (the red boundary) and a lower energy grain boundary BC (the blue boundary) by the formation of a new grain C twinned to grain

A. This type of annealing twin formation happens when the interfacial energy γ of each boundary satisfies the following condition:

$$\gamma_{CTB} + \gamma_{ITB} + \gamma_{BC} < \gamma_{AB} \quad (5-2)$$

Thus, it cannot happen between random adjacent grains with random grain boundaries. The relative orientation of grain A and B should be in some range that the newly formed boundary BC which contains lower interfacial energy than boundary AB. The annealing twin formation in this mechanism does not require the migration of the high energy grain boundary AB. This is the reason why this mechanism of slow grain growth is observed in samples after holding for 24min and 36min, shown in figure 33. The driving force for this type of annealing twin formation should be the reduction of the interfacial energy of the system. This is in good agreement with several authors.[107-109].

The highlighted red circle areas in the sample after holding for 48min presented in figure 41 show another type of annealing twin formation due to HAGB migration. In this case, coherent twin boundaries form on the back of HAGBs migrating to a higher strained region, and the formed twin grains contain much lower GND density. This indicates the formation of annealing twin boundaries from migrating HAGBs, thus there is a reduction of the stored energy of the system by consuming the dislocation density where twin formation takes place. Recalling figure 33, the grain size increases at holding times of 36min to 48min compared to 24min to 36min, indicating a more active grain boundary migration during this period. This observation is again consistent with the growth accident model [71] which is based on grain boundary migration. Areas with higher GND density can still be observed in grains which have already formed annealing twin boundaries, and

this suggests that the induction rapid heating process is a dynamic process due to the continuous load caused by the thermal stress between the surrounded environment and the heated sample.

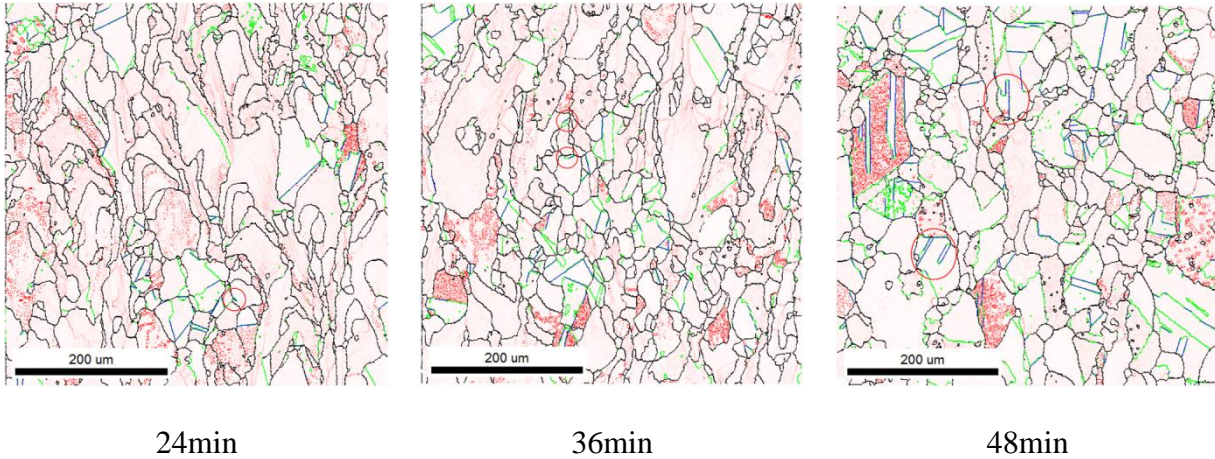


Figure 41. GND density distribution map with highlighted annealing twin boundaries at 200°C/s rapid heating at 1150°C holding for 24-48min

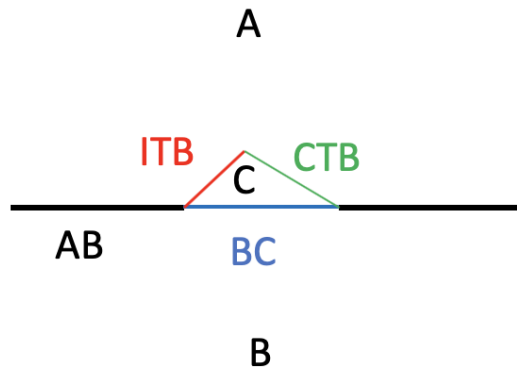


Figure 42. Illustration of grain boundary dissociation model, the thickness of each boundary represents its interfacial energy. Figure reproduced from Meyers' research[72]

The observation via TEM gives a clearer idea about the change of microstructure and the formation of annealing twin boundary during induction rapid heating process. Figure 43 shows a series of TEM images of as-fabricated sample (labelled as AF) and samples heat treated at 200°C/s rapid heating at 1150°C. The as-fabricated sample from SLM process shows a cellular

microstructure with high dislocation density. The dislocations are present in a network form generating on the boundaries of cells, which should be due to the development of internal stress and localized strain during rapid solidification in SLM process. When heated to 1150°C and held for 5 seconds, the cellular structure starts to disappear and dislocation density starts to decrease. Stacking faults are observed to take place both inside a grain and on a grain boundary. After holding for 3min, more stacking faults associate to grain boundaries. After holding for 6min, stacking faults start to grow from grain boundaries. Since in FCC crystals a stacking fault can be regarded as a very small twin boundary with a thickness of one atom layer, the accumulation of stacking faults growing from grain boundaries indicates the initiation of twin boundary formation. The 12min holding time sample shows another example of annealing twin initiation at a grain boundary and then propagates into the grain in the left image. The right image after 12min holding time shows a formed twin boundary with lower amount of dislocations in the newly formed twinned grain, supporting the observation in EBSD that the formation of annealing twin boundaries decreases the stored energy of the system by consuming dislocations. After holding for 48min, more stable annealing twin boundaries have formed, but associations of dislocations and stacking faults onto grain boundaries can still be observed. This is probably due to the induction heating process and the lower thermal conductivity of the system. That is, rapid induction heating is dynamic process, in which the sample continuously experiences the thermal stress caused by the temperature difference between the environment (at room temperature) and the sample itself (at the heat treatment temperature).

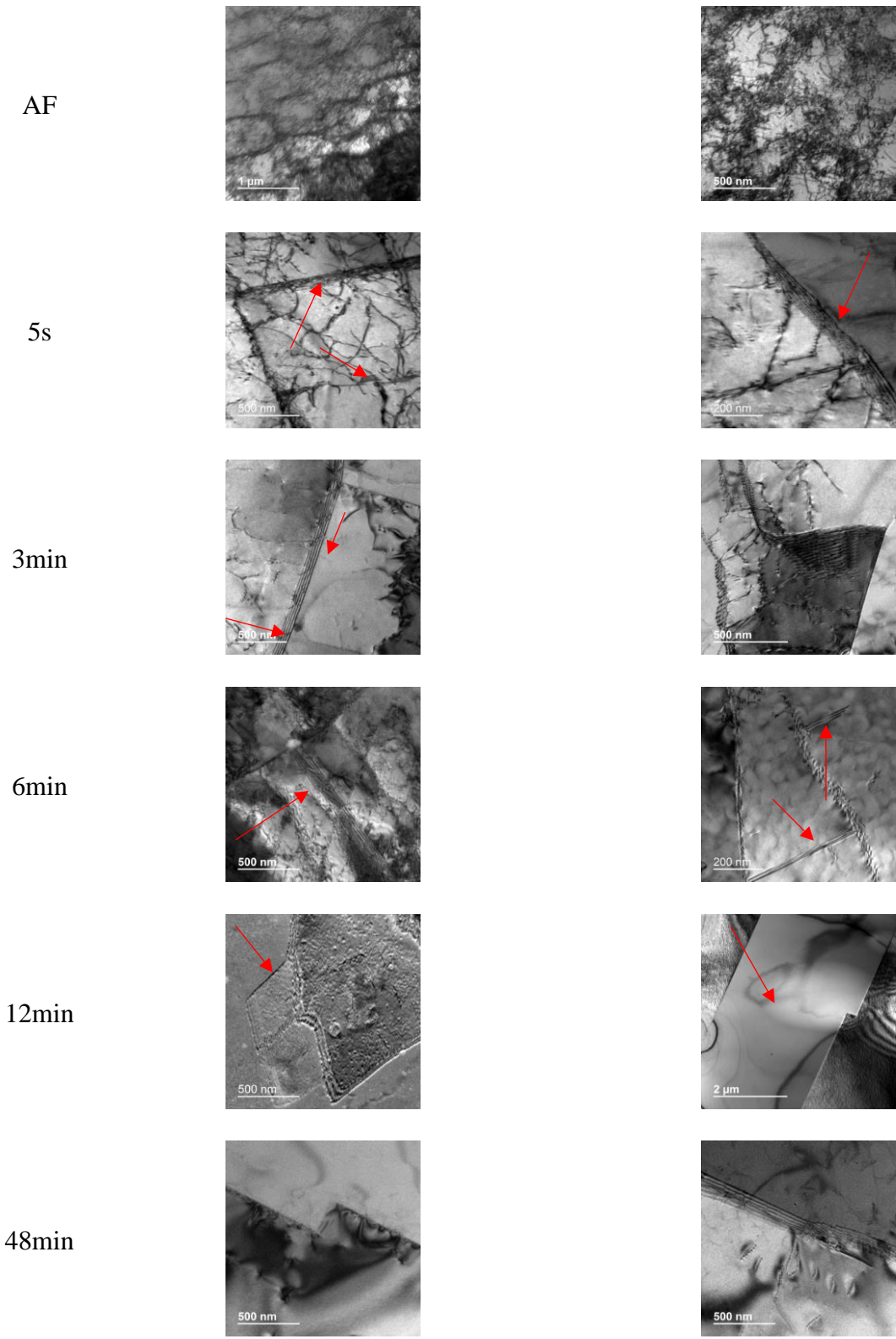


Figure 43. TEM images showing the change of microstructure of as-fabricated samples and samples heated at 200°C/s rapid heating at 1150°C

In summary, two types of annealing twin formation mechanisms are observed during the rapid heating process. The growth accident mechanism takes place when grain boundaries show higher mobility. The phenomenon of grain boundary dissociation takes place in lower energy grain boundaries which will exhibit less mobility. The annealing twin density increases as the recrystallization fraction increases. However, the relationship between them does not exactly matches the previous studies about annealing twins in other FCC materials. This difference in behavior is most likely due to the impact of the induction heating process used in this study.

5.1.2 Comparison with Classical Models

In the previous section, annealing twin boundaries formed via the growth accident model and grain boundary dissociation model were observed. In this section, the experimental data from this study will be compared to these models, this should provide an idea about which mechanism is dominant during the rapid induction heating process.

According to the growth accident model first provided by Gleiter[71] as described in equation (2-7) in chapter 2, the coherent annealing twin density, ρ_c' , should be proportional to the possibility of formation of a coherent twin boundary, R . Since Gleiter measured the coherent twin density via line intersect method, the coherent twin density measured by EBSD in this study, ρ_c , should multiply $2/\pi$ to convert to the coherent twin density, ρ_c' , according to the quantitative stereology method[110]. Gleiter applied $\Delta G=2\delta/r=4\delta/d$ according to W. Charnock's work[111], where δ is the energy of grain boundary, r is the radius of the grain, and d is the grain size. Thus, equation (2-7) can be re-written in the form of equation (5-3) and then simplified to equation (5-4):

$$\rho'_c = c * \exp \left\{ \frac{1}{a} \ln \left(e^{-Q/kT} \frac{4\delta}{dkT} \right) \right\} \quad (5-3)$$

$$\ln \rho'_c = \frac{-Q}{akT} + \frac{1}{a} \ln \left(\frac{4\delta}{kT} \right) - \frac{1}{a} \ln d + \ln c \quad (5-4)$$

where c is a ratio constant, and a is a constant related to the material's property by equation (5-5):

$$a = \frac{\pi \varepsilon^2 h^2}{Q \gamma_t} - 1 \quad (5-5)$$

Therefore, the plot of $\ln \rho'_c$ vs. $\ln d$ should give a straight line with a slope equal to $-1/a$, which should be independent of temperature. To verify this model, corresponding material constants of SS316L has been searched from the literature: the Boltzmann's constant $k = 1.38 \cdot 10^{-23} \text{J/K}$; the activation enthalpy for SS316L $Q = 177.52 \text{kJ/mol} = 2.95 \cdot 10^{-19} \text{J/atom}$ [112]; the average energy of HAGB in SS316L $\delta = 0.6 \text{J/m}^2$ [113], the lattice constant $a_0 = 0.3594 \text{nm}$, thus the height of the nucleus $h = d_{111} = 0.2075 \text{nm}$ [114]; as described before $\Delta G = 4\delta/d$, where d is the grain size; the energy of step $\varepsilon = \delta/2 = 0.3 \text{J/m}^2$; the surface energy of a coherent twin boundary $\gamma_t = \gamma_{\text{SFE}}/2 = 0.032 \text{J/m}^2$ [115], and the stacking fault energy $\gamma_{\text{SFE}} = 64 \text{mJ/mm}^2 = 0.064 \text{J/m}^2$ [116]. By converting the units of all the constants to international system of units (SI), the value of a (eqn. 16) can be calculated approximately as 0.2890, thus the slope of the curve $\ln \rho'_c$ vs. $\ln d$ should be -3.4608.

Figure 44 shows the scatter points of $\ln \rho'_c$ vs. $\ln d$ at various heating rates and temperatures used in this study. The dash line represents the slope that Gleiter's model predicted for SS316L. The data points in this study deviate far away from Gleiter's model. At the early stage, the coherent twin density increases as the overall grain size increases; this is contrary to the prediction of Gleiter's model. That is coherent twin density should decrease as the grain size increases. This makes sense since the annealing twin boundaries start forming at the early stage, while the model

relation between the coherent twin density ρ_c' and the grain size d as shown in the following equation:

$$\frac{\rho_c'}{\rho_0} = \frac{d_0}{d} \ln \left(\frac{d}{d_0} \right) \quad (5-6)$$

where ρ_0 is a constant of scaling factor proportional to the ratio of average grain boundary to twin boundary energy, and d_0 is another constant of scaling factor meaning the critical grain size before which the average number of coherent twin boundaries inside a grain is zero.

Figure 45 shows the results of curve fitting to Pande's model based on the experimental data from all series of induction rapid heating. Pande's model fits the data points better than Gleiter's model. The curve agrees with the change of coherent twin density in response to the average change of grain size. For the fitting curve, the constants are calculated as followed: $\rho_0=16.75\text{mm}^{-1}$ and $d_0=43.24\mu\text{m}$. The result suggests that the critical grain size after which the growth accident mechanism starts to take place for twin boundary formation is $43.24\mu\text{m}$. The successful fitting for the trend of experimental data supports that the growth accident mechanism is the dominant mechanism for annealing twin formation, while the imperfect points away from the curve show the occurrence of the grain boundary dissociation to form annealing twin boundaries according to previous EBSD observation, and the propagation of formed twin boundaries.

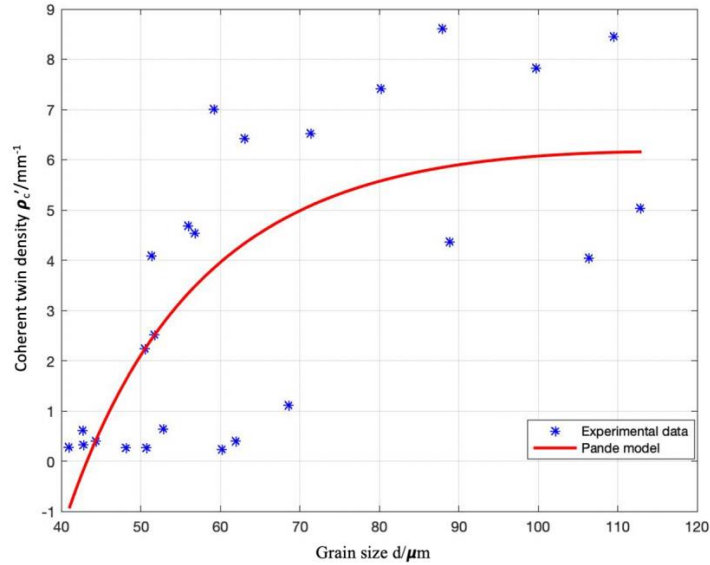
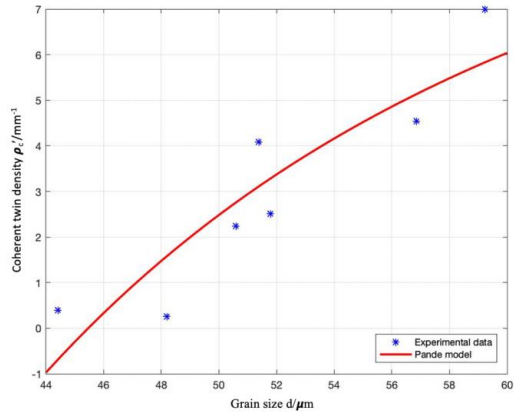


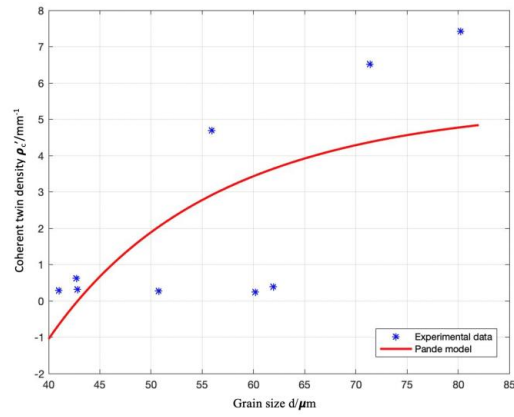
Figure 45. Relationship between coherent twin density and grain size in induction rapid heating

It should also be noticed that the deviation of the data points to the curve is small when grains start to grow, and then increases as the grain size increases, and finally decreases as the grains become coarser when abnormal grain growth occurs. Figure 46 shows the results of curve fitting to Pande's model by separating the experimental data according to temperature. The results indicate that the annealing twin density behavior varies at different temperatures. Figure 46(a) shows that Pande's model fits well with the experimental data at 1150°C, with constants $\rho_0=28.72\text{mm}^{-1}$ and $d_0=45.46\mu\text{m}$. It suggests that the growth accident mechanism is dominant of annealing twin formation at this temperature, and the deviation of experimental data to the model is probably due to the grain boundary dissociation which can also form new annealing twin boundaries, and the propagation of formed annealing twin boundaries. Figure 46(b) shows that the Pande's model is less applicable to experimental data at 1200°C than it is at 1150°C. At this temperature the model can still show relatively good agreement with the experimental data with the constants $\rho_0=14.26\text{mm}^{-1}$ and $d_0=42.84\mu\text{m}$, but deviation between the experimental data and the model starts to increase as grain size increases. This is probably due to the increasing rate of

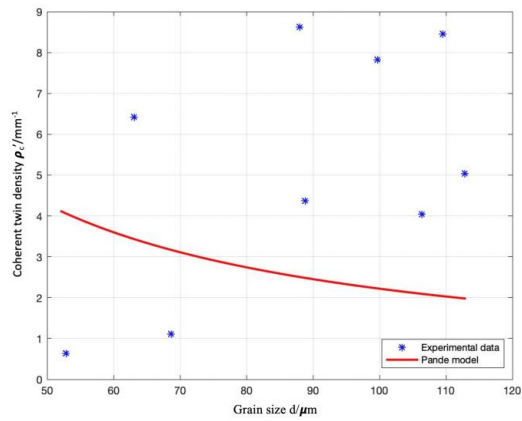
annealing twin boundary propagation and extension as the recrystallized grains grow at elevated temperature, which makes a stronger contribution to the annealing twin density at 1200°C. Figure 46(c) shows a series of more dispersive experimental data at 1250°C than those at 1200°C, which Pande's model fails to predict. From the microstructure shown in the previous EBSD results, grain coarsening starts to occur at 1250°C. The formed annealing twin boundaries propagate and extend in the grains faster than at 1200°C, which further minimizes the contribution of the growth accident mechanism to annealing twin density. During grain coarsening, large grains consume small grains and their annealing twin boundaries without producing more twin boundaries, and this is energetically favorable since it decreases the amount of interfaces in the system. However, the presence of local thermal stresses in the specimens continuously provides the driving force for new annealing twin formation during grain growth and coarsening. Such factors make positive and negative contributions to coherent twin density at 1250°C, making the experimental data dispersive and decreasing the influence from growth accident theory. The influence of grain coarsening is also shown in the final decreasing in relationship between annealing twin density and recrystallization fraction as the dash curves show in figure 47.



(a)



(b)



(c)

Figure 46. Curve fitting to Pande's model at different temperatures: (a)1150°C, (b)1200°C, (c)1250°C

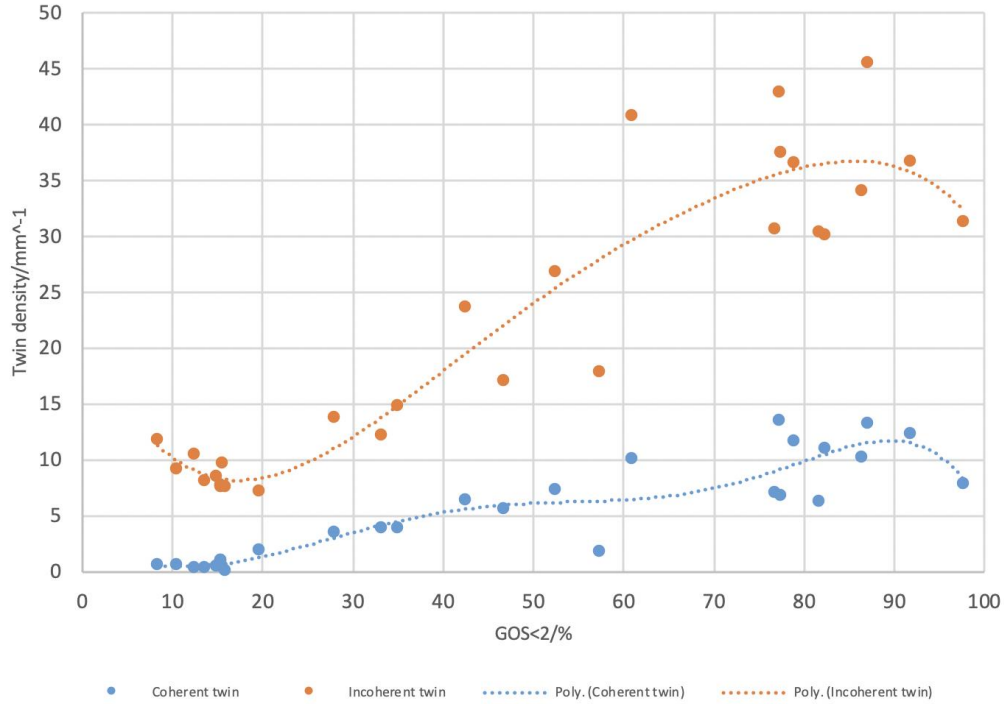


Figure 47. Relationship between recrystallization fraction and twin density of experimental data at all temperatures and heating rates in induction rapid heating

5.1.3 Summary

Rapid induction heating is a dynamic process, the annealing twin density increases as the recrystallization fraction increases, and slightly decreases as grain coarsening starts to occur. There are two steps of twin density increasing during the rapid heating process. The first step of annealing twin density increasing is due to sub-grain boundary migration and the second step of increasing is due to HAGB migration.

The formation mechanisms of annealing twin boundaries are observed to be growth accident and grain boundary dissociation. Growth accident is the dominant mechanism of annealing twin formation depending on grain boundary migration, that HAGBs migrate into strained regions and twin boundaries form at these HAGBs forming a twinned new grain with

much lower dislocation density. Grain boundary dissociation also takes place when a high energy grain boundary decomposes to a coherent twin boundary, an incoherent twin boundary and a grain boundary with lower energy, this mechanism does not require grain boundary migration.

The experimental data generated in this study was compared with classic models of growth accident mechanism for annealing twin formation. Gleiter's model is not able to predict the relationship between the coherent twin density and grain size and temperature, and it probably has couple reasons. Gleiter's model was derived only considering steady heat treatment of a deformed material, and the influence of grain boundary migration, without considering the propagation and extension of the formed twin boundaries.

Compared to Gleiter's model, Pande's model seems to make more sense explaining the experimental data, which supports that the growth accident theory is the dominant mechanism of annealing twin formation. However, the different fittings between the experimental data separated by temperature indicate that the annealing twin density behavior does change with temperature, which is contrary to Pande's conclusion that annealing twin density should be uniquely dependent on grain size. This is probably due to the increasing influence from twin boundary propagation and grain coarsening as temperature increases.

5.2 The Recrystallization Kinetics Analysis

According to the presented results, the recrystallization behavior seems to be strongly related to some processing parameters and the thermal conductivity of stainless steel 316L. Hence, the analysis of the kinetics of recrystallization in all conditions of heat treatments was examined to show the effect of processing and thermal conductivity. Classically, the recrystallization kinetics

can be analyzed using the Johnson-Mehl-Avrami-Kolmogorov (JMAK) model. This model was built by Kolmogorov In 1937[117], Johnson and Mehl in 1939[118], and Avrami in 1939[119]. The JMAK model assumes the nucleation sites to be randomly distributed and formed at a rate \dot{N} , and grains grow into the deformed material at a linear rate \dot{G} . Based on this assumption, the model provides a relationship between the fraction of recrystallized material X_V and time t described in equation (5-7):

$$X_V = 1 - \exp(-Bt^n) \quad (5-7)$$

Where $B = f\dot{N}\dot{G}^3/4$, and f is a shape factor (for example $4\pi/3$ for spheres). Equation 11 is also well-known as JMAK equation. This equation indicates that the plot of $\ln\{\ln[1/(1-X_V)]\}$ against $\ln t$ should be a straight line with a slope equal to the exponent n , and n should be equal to 3 or 4.

5.2.1 Recrystallization Kinetics at Different Processing Conditions

Figure 48 shows the plot of recrystallization kinetics analysis for samples heat treated at 1150°C using JMAK equation. The blue curve of conventional low heating rate shows a static recrystallization rate with an average JMAK slope of 1.52. Such a low value of exponent compared to the value 3 or 4 of an ideal JMAK slope can be due to the inhomogeneity of the as-fabricated microstructure, resulting in non-random distribution of nucleation sites and variations in stored energy. The influence of starting inhomogeneous microstructure on decreasing the n value have been reported in some studies in different types of materials[120-123]. This further leads to the variation of growth rate, since the driving force of boundary mobility would vary due to the inhomogeneity of microstructure. Being different from the conventional low heating rate, the orange curve of induction rapid heating rate (200°C/s) shows a dynamic behavior in change of

recrystallization rate against time. The average recrystallization rate of rapid heating is similar as it of conventional slow heating in 60 minutes at 1150°C. The curve shows two peaks of fast recrystallization kinetics, with n value of 1.93 at the first peak and that of 4.83 at the second peak. Obviously, rapid heating rate can provide faster recrystallization rate due to the additional energy input and local thermal stresses promoting boundary migration. This faster recrystallization rate results in faster nucleation rate and growth rate. The faster nucleation rate means that more nucleation sites are formed per unit time, leading to smaller grain size after recrystallization. The faster growth rate indicates a potential risk of faster grain coarsening if the holding time is too long. Thus, holding time is also a key parameter in rapid heating treatment of 3D printed 316L stainless steel. The drop between the two peaks can be the result of local thermal stresses associated to the poor thermal conductivity of 316L stainless steels.

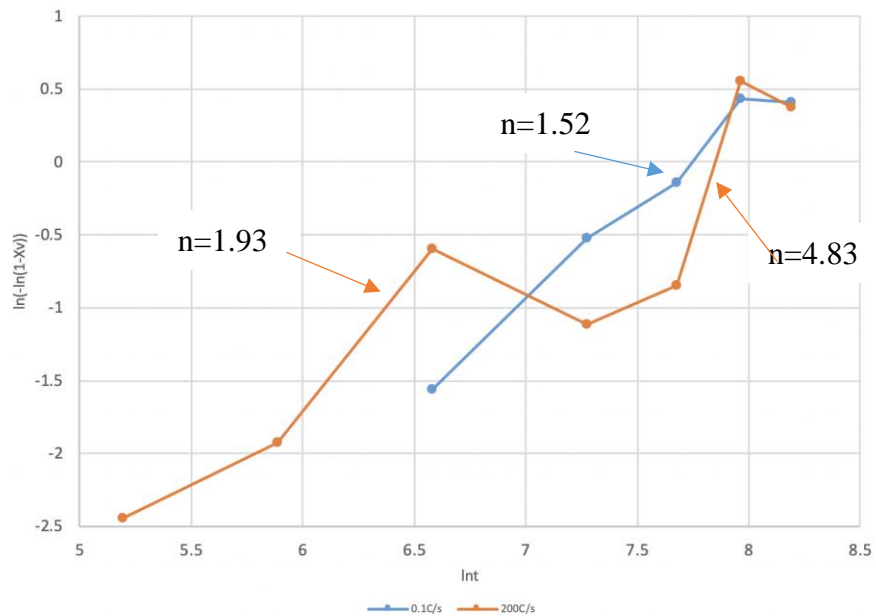


Figure 48. JMAK recrystallization kinetics analysis for samples heat treated at 1150°C

Figure 49 shows the JMAK plot of samples heat treated at 1200°C holding from 3-12min. The blue, orange and green curves show the recrystallization behavior against holding time of

10°C/s, 100°C/s, 200°C/s heating rates, with n values of 2.17, 3.25 and 3.65, respectively. High heating rates (100°C/s and 200°C/s) provide faster recrystallization rates than low heating rate (10°C/s), and this is consistent with the results observed at 1150°C. However, the recrystallization rates of 100°C/s and 200°C/s do not show as large difference as it did between 10°C/s and 100°C/s, indicating that the benefit of increasing heating rate has a limitation. Compare the curve of 200°C/s at 1150°C in the same holding time area (first peak of the orange curve in figure 48), all three heating rates at 1200°C show faster recrystallization kinetics. This indicates as expected, that the reheating temperature also plays an important role in determining the recrystallization rate.

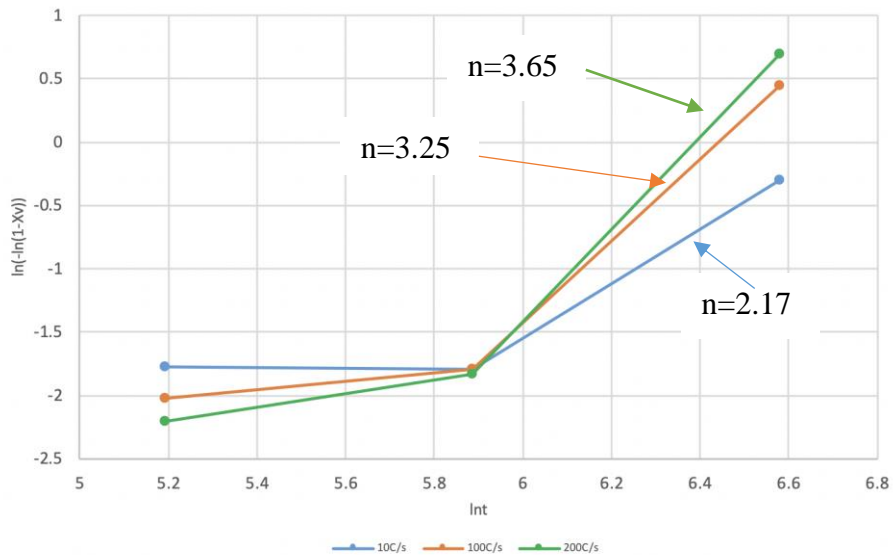


Figure 49. JMAK recrystallization kinetics analysis for samples heat treated at 1200°C

Figure 50 shows the JMAK plot of samples heat treated at 1250°C holding from 3-12min. The curves of 10°C/s and 100°C/s are flat, since these samples are at the last stage of recrystallization (as shown in corresponding GOS map in figure 30). The n values cannot be obtained through these two curves. However, by comparing the X_v values of 10°C/s and 100°C/s at 1200°C and 1250°C, it is obvious that the recrystallization fraction has reached similar values

in 3min at 1250°C, while it takes 12min at 1200°C for both heating rates. Thus, the recrystallization rates of 10°C/s and 100°C/s at 1250°C should be much faster than that at 1200°C. Being different from the curves at 1150°C and 1200°C, there is an obvious delay in recrystallization of 200°C/s series samples at 1250°C, and the recrystallization kinetics analysis shows an n value of 2.47, which is lower than the same heating rate at 1200°C. This can be due to the low thermal conductivity of 316L stainless steel that the temperature homogeneity takes longer for samples subjected to higher heating rates.

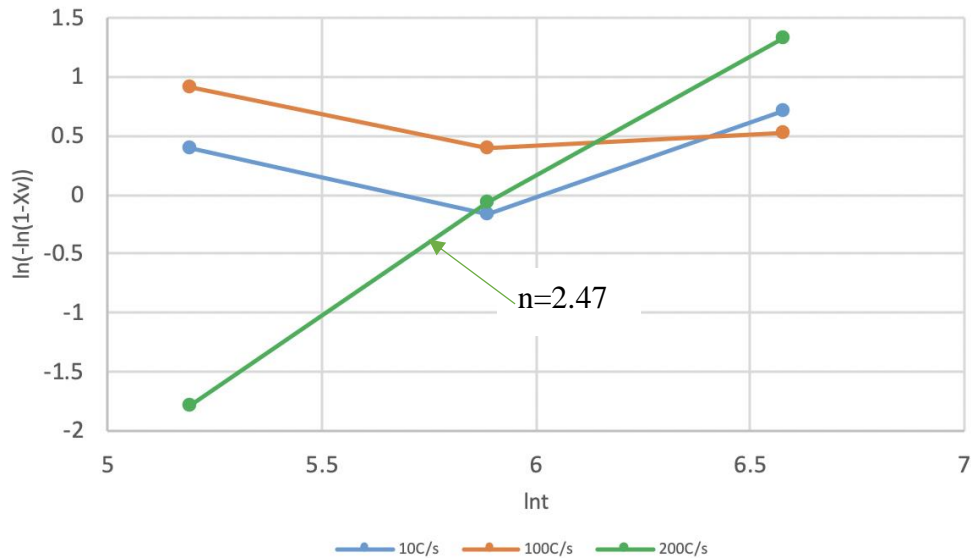


Figure 50. JMAK recrystallization kinetics analysis for samples heat treated at 1250°C

Figure 51 shows the change of the increase amount of twin density ($\Delta\rho$) against the recrystallization rate (the time exponent n) before grain coarsening after rapid induction heating process. The n value is the response of the evolution of microstructure to isothermal holding time. It represents the combination influence of the reheating temperature and heating rate, thus the processing parameters are not separately considered in figure 51. The increase of coherent twin density and incoherent twin density first increase as the recrystallization rate (n value) increases,

and then decrease as the recrystallization rate further increases. This is reasonable because the recrystallization rate consists of nucleation rate and growth rate. When the recrystallization rate initially increases, the increase in nucleation rate and growth rate contribute to grain boundary migration to the strained areas. This is beneficial to the formation of annealing twin boundaries as a result of the growth accident mechanism. However, as the recrystallization further increases, the increase of growth rate will lead to grain coarsening, and hence decrease the annealing twin density. In general, figure 51 shows the ability of recrystallization rate to ‘create’ new annealing twin boundaries. According to the curves in figure 51, the optimal n value would be around 2.5-3.5.

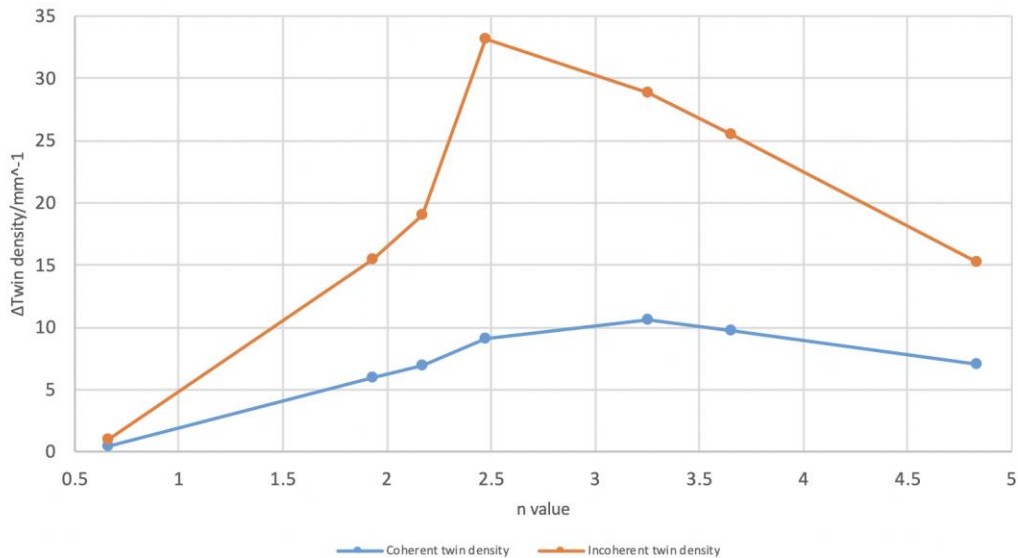


Figure 51. Relationship between twin density increase and recrystallization rate (n value)

Table 8 shows the typical n values at the best processing conditions summarized in table 7. Conditions 3 and 7 have n values close to the range 2.5-3.5. Condition 1 is a little far away from this range, but it was operated at a long holding time (48min) and a relatively lower temperature (1150°C), which provides a larger initial twin density.

Table 8. The n values of best processing conditions in chapter 4

Condition No.	n value
1	4.83
3	3.65
7	2.47

5.2.2 Summary

In this section, the recrystallization kinetics were analyzed at all processing conditions in induction rapid heating process using the JMAK equation. As a conclusion, the recrystallization rate increases as heating rate increases before grain coarsening starts to take place. A delay in recrystallization was observed at 1250°C when heating rate was increased to 200°C/s. This is probably due to the poor thermal conductivity of SS316L. The optimal processing conditions to obtain large annealing twin density are the processing conditions which bring the recrystallization time exponent n between a range of 2.5-3.5.

5.3 The Effect of Heating Rate

Based on the presented and discussed results in chapter 4, it has been shown that different heating rates result in different recrystallization rates and annealing twin densities. Various heating rates and reheating temperatures lead to different recrystallization kinetics (different n values), and this could be attributed to the inhomogeneous temperature distribution during induction heating.

To further understand the influence of heating rate, the heat transfer during induction heating needs to be analyzed.

5.3.1 The Principle of Induction Heating

Induction heating is a combination process of electromagnetic and heat transfer that generates heat on an electrically conductive object by eddy currents from an alternating current through a coil. The advantage of induction heating is that the heat is generated inside the sample itself, hence the sample can be heated rapidly, and no external heat source or contact is necessary.

The relative magnetic permeability μ_r of the material is significant in induction heating. According to the value of μ_r the materials can be divided into three types. The materials with $\mu_r < 1$ are called diamagnetic materials, and those with $\mu_r > 1$ (slightly larger than 1) are called paramagnetic materials. Since the difference of μ_r for diamagnetic and paramagnetic materials is small, they are also called nonmagnetic materials in induction heating process. Such materials include copper, aluminum, titanium, etc. The materials with $\mu_r \gg 1$ are called ferromagnetic materials, such as iron and nickel. The ferromagnetic property of a material is related to the temperature, and the temperature at which a ferromagnetic material becomes nonmagnetic is called the Curie temperature (Curie point)[124]. Stainless steel 316L has a μ_r value around 1.01[125], and it belongs to nonmagnetic material in induction heating.

During induction heating, the current distribution is not uniform in the specimen, and therefore the temperature in the specimen is not uniform, either. This is caused by some electromagnetic effects, including skin effect, proximity effect, ring effect, end and edge effects.

Skin effect is a phenomenon that the maximum current density will be on the surface of a conductor when applying an alternating current. Hence, the current density of the sample decreases from its surface to its center during induction heating. Since the eddy current generated on the sample is circumferential, the current flow at the center of the sample should be zero. Thus, approximately 86% of the power will be concentrated in the surface layer of the sample, and this layer is called the penetration layer, with a current penetration depth δ (m) expressed in the following equation:

$$\delta = \sqrt{\frac{\rho_r}{\pi\mu_0\mu_r f}} \quad (5-8)$$

Where ρ_r is the resistivity of the material in $\Omega\cdot\text{m}$; $\mu_0 = 4\pi*10^{-7}\text{H/m}$ is the permeability of vacuum space; f is the frequency of alternating current in Hz[126]. In this study, skin effect should be the major reason for local thermal stresses within the fast heated samples.

Proximity effect is the influence from the magnetic fields of other electrically conductive parts located close to the sample. The magnetic fields from these parts will interact with each other and therefore distort the current density distribution in the sample during heat treatment. In this study, the samples were supported by non-electrically conductive aluminum oxide ceramic pieces, and there was nothing else inside the coil zone. Hence, the proximity effect can be neglected.

Ring effect is the situation in which the heated sample is bent or it is a ring shape, and therefore its current density distribution changes. In this case, the magnetic fields will be higher inside the ring and disperse outside of the ring. Thus, the generated current will flow in the inside surface layer of the ring. This is a positive effect when the heated sample locates inside the coil during induction heating, because the coil current is generated in the inside surface of the coil shortening the coil-sample coupling. Hence, the coil efficiency increases, and vice versa. In this

study, samples were located inside the coil, and the ring effect played a positive role. All samples are in bar-shape and small compared to the size of the coil, thus it is not necessary to consider the ring effect to the samples.

End and edge effect is the magnetic field distortion and corresponding current distribution in an induction heated sample due to the distortion of electromagnetic field in its end and edge areas. This leads to non-uniform temperature profile in the sample. In this study, all samples were characterized in the center area, edge areas were not highly focused.

5.3.2 Analysis of Local Thermal Stresses during Rapid Induction Heating

In induction heating, heat is transferred by conduction from the high temperature surface layer of the sample to the low temperature center region, and it can be described by Fourier's Law[127]:

$$q_{cond} = -\lambda(T) \cdot grad T \quad (5-9)$$

Where q_{cond} is the conduction heat flux, $\lambda(T)$ is thermal conductivity in $W/(m^{\circ}C)$, and T is temperature. Considering the temperature distribution in a sample in three dimensional, the temperature T should be a function of time t and position x , y and z , such as:

$$T = f(x, y, z, t) \quad (5-10)$$

By considering the Fourier's Law and the Law of Conservation of Energy, the temperature distribution can be written as a differential equation:

$$\frac{\partial T}{\partial t} = \frac{\lambda}{c_p \rho} \left(\frac{\partial^2 T}{\partial x^2} + \frac{\partial^2 T}{\partial y^2} + \frac{\partial^2 T}{\partial z^2} \right) \quad (5-11)$$

Where c_p is the specific heat in J/kg*K, ρ is the density in kg/m³. The left side of equation (5-11) is the heating rate, and it is obvious that a higher heating rate will lead to a larger temperature gradient along the distance from the surface to the center. Equation (5-11) can be simplified by considering one dimension in the thinnest dimension of a sample in this study (~5mm), as shown below:

$$\frac{\partial T}{\partial t} = \frac{\lambda}{c_p \rho} \frac{\partial^2 T}{\partial x^2} \quad (5-12)$$

Thus, it is clear that the higher the heating rate, the higher the temperature gradient during heating process. Moreover, it can be seen in equation (5-12) that the low thermal conductivity also results in higher temperature gradient. A higher heating rate would require a higher frequency in induction heating, and this will lead to a thinner penetration depth, as described in the skin effect in equation (5-8). This leads to a decrease in the depth of high temperature layer, and therefore a longer distance for heat conduction and a larger temperature difference between the surface and center.

During isothermal holding period, the system holds the temperature of the surface at the target temperature, and the temperature of current penetration layer can be regarded stable at the target temperature T_{reheat} . In this period, heat is transferred into the center with a boundary condition that $T_{\text{surface}} = T_{\text{reheat}}$. As discussed before, a higher heating rate will result in a thinner high temperature zone and a larger temperature difference between the surface layer and the center. This will lead to a larger thermal stress, which promotes the recrystallization by increasing the recrystallization rate, and it can explain the results at 1150°C and 1200°C that higher heating rates lead to faster recrystallization kinetics and higher annealing twin density. It will also lead to a longer period of temperature homogeneity through the sample, which can explain the delay of recrystallization process and annealing twin density increase at 1250°C at 200°C/s.

The consideration of local thermal stress also leads to similar conclusions. For a rigid body, thermal stress is the result from restricted thermal expansion caused by the difference in temperature. During rapid induction heating, there is a temperature difference between the surface and the center of the heated sample due to the skin effect, as discussed before. The surface layer at high temperature wants to expand and push the center area at low temperature, and the restraint from the rigid body prevents the expansion and creates local thermal stresses in the sample. It can be considered in one dimension to simplify the analysis. From the stress-strain relationship in uniaxial loading condition, it can be obtained that:

$$\sigma = \frac{F}{A} = E\varepsilon \quad (5-13)$$

Where σ is the normal stress, F is the applied force, A is the loading area, E is the Young's modulus and ε is the strain.

Considering linear thermal expansion (one dimension in consistent with discussions before), the thermal strain can be obtained that:

$$\varepsilon = \frac{\Delta l}{l_0} = \alpha\Delta T \quad (5-14)$$

Where $\Delta l/l_0$ is the potential change in length caused by thermal expansion, α is the coefficient of thermal expansion, and ΔT is the difference in temperature. Combining equation (5-13) and equation (5-14), the thermal stress can be calculated by:

$$\sigma = E\alpha\Delta T \quad (5-15)$$

Suppose that the sample is just heated to the target temperature T_0 during induction heating. Since the infrared temperature detector measures the temperature on the surface T_s , at this moment

$T_s = T_0$. Assuming the temperature at the center is T_c and the distance from the surface penetration layer to the center is x_0 . At this moment, the system stops heating the sample, and it can be obtained that:

$$\frac{\partial T}{\partial t} = 0 \quad (5-16)$$

And combining with equation (5-12), we can get:

$$\frac{\partial^2 T}{\partial x^2} = 0 \quad (5-17)$$

Integrate equation (5-17), we can get:

$$T = C_1 x + C_2 \quad (5-18)$$

Where C_1 and C_2 are constants and can be obtained by boundary conditions:

$$x = 0, T = T_0 \quad (5-19)$$

$$x = x_0, T = T_c \quad (5-20)$$

Substitute the boundary conditions into equation (5-18), the constants can then be obtained:

$$C_1 = \frac{T_c - T_0}{x_0} \quad (5-21)$$

$$C_2 = T_0 \quad (5-22)$$

Thus, the temperature distribution along the direction from surface to center can be written as a function of position as follows:

$$T = \frac{T_c - T_0}{x_0} x + T_0 \quad (5-23)$$

Hence, it can be obtained that:

$$\Delta T = T_0 - T = \frac{T_0 - T_c}{x_0} x \quad (5-24)$$

Substitute into equation (5-15), the thermal stress at position x can be written as follows:

$$\sigma = E\alpha \frac{T_0 - T_c}{x_0} x \quad (5-25)$$

And we know that x_0 should be equal to half of the thickness minus the penetration depth, in this case, which is:

$$x_0 = 0.0025 - \sqrt{\frac{\rho r}{\pi \mu_0 \mu_r f}} \quad (5-26)$$

Substitute into equation (5-25), the thermal stress σ at position x can be written as:

$$\sigma = E\alpha x k \quad (5-27)$$

Where the coefficient k can be written as:

$$k = \frac{T_0 - T_c}{0.0025 - \sqrt{\frac{\rho r}{\pi \mu_0 \mu_r f}}} \quad (5-28)$$

Now the relationship between local thermal stress σ and heating rate has been built. At a specific reheating temperature T_0 , there are two parameters that changes with heating rate. As the heating rate increases, the frequency f increases in order to provide the necessary heating rate. Meanwhile, the temperature at the center of the sample T_c decreases, since the surface layer reaches the target temperature faster, and the time for conduction is less. As shown in the expression of k value, the increase of frequency will decrease k and the decrease of T_c will increase

k. Thus, the increase of heating rate may not always lead to the increase of local thermal stress, which further promotes the recrystallization and annealing twin boundaries formation. This can explain the different behaviors of the results at various temperatures. At 1150°C holding for 12min, the annealing twin density increases as heating rate increases. However, at 1200°C and 1250°C, the annealing twin density and recrystallization rate is not monotonically increase as the heating rate increases. The criteria whether the local thermal stress increases with the heating rate is the k value in equation (5-28). At a certain reheating temperature, if the increase of heating rate results in an increase of k value, the local thermal stress would increase, and the annealing twin density should increase. If the increase of heating rate results in a decrease of k value, the local thermal stress would decrease, leading to a decrease in annealing twin density.

5.3.3 Summary

According to the annealing twin boundary formation mechanism described in section 5.1, the local strain caused by local thermal stresses in the rapid heated samples is highly related to the annealing twin boundary formation. Thus, the local thermal stresses are analyzed. The analysis is applied in one dimension for simplification.

During induction heating, skin effect is the major factor causing the temperature gradient and therefore local thermal stresses in the sample. The heat transfer equation is derived using the Law of Conservation of Energy and the Fourier's Law. The local thermal stress at position x in the sample is derived through the restraint of thermal expansion. By combining these two conditions, the local thermal stress σ can be expressed as a function of reheating temperature T_0 , the temperature of the sample's center T_c , and the frequency f. The k value expressed in equation (5-28) can be applied as a one-dimensional simplified criteria of the effect of heating rate. If the

increase of heating rate leads to the increase of k value, the heating rate will play a positive role because the local thermal stress would increase, leading to the increase of recrystallization kinetics and annealing twin density. And vice versa. This can explain the non-monotonically increasing behavior of annealing twin density with the increase of heating rate.

5.4 Verification of Hypothesis

This section is a brief summary of the discussions by revisiting the hypothesis raised in Chapter 1. It was assumed that higher heating rates would lead to higher annealing twin density due to the increase of energy input and local thermal stresses. More specifically, 4 questions were raised in Chapter 1: 1) at what point in the post heat treatment will the AM specimens be able to form annealing twin boundaries? 2) Is this mechanism similar to conventional polycrystalline recrystallization and grain growth behavior? 3) Is there any preference of the annealing twin boundary formation to some specific grain boundaries? 4) How will the annealing twin density be related to the processing parameters of the post heat treatment?

For question 1, it can be seen from the set of samples heat treated at 1150°C using 200°C/s holding from 3-60min that the annealing twin boundaries form as recrystallization starts to take place. This is due to grain boundary migration and grain boundary dissociation.

For question 2, the mechanism is not similar as the recrystallization and grain growth behavior of conventional furnace heat treatment. The conventional heat treatment has a low heating rate and a stable environment, thus the temperature distribution in the heat treated sample is homogeneous and the recrystallization process is steady. In contrast, the induction rapid heating has a fast heating rate. During induction heating, only the sample would be heated to high

temperature, while the surrounded environment is at room temperature. This results in a non-steady process in combination of recrystallization and load from local thermal stresses. The recrystallization kinetics of induction heating is much faster than that of conventional furnace heating, while the grain growth is restricted compared to conventional furnace heating at the same reheating temperature.

For question 3, two formation mechanism of annealing twin boundaries were observed. Growth accident is the dominant mechanism, in which the annealing twin boundaries form at HAGBs migrating into strained areas. Grain boundary dissociation is a minor mechanism, in which the annealing twin boundaries form at decomposed high energy boundaries.

For question 4, the annealing twin density cannot be simply related to processing parameters. Before grain coarsening starts to occur, the annealing twin density increases as temperature, heating rate and holding time increases. When grain coarsening takes place, the annealing twin density will decrease as grains grow further. The increase amount of annealing twin density is found to first increase and then decrease as the recrystallization rate increases. The reheating temperature is a major factor influencing the recrystallization kinetics. In general, the increase of reheating temperature will increase the recrystallization rate. However, the recrystallization behavior might be delayed and restricted when fast heating rate is also applied due to the poor thermal conductivity of 316L stainless steel. The increase of heating rate at 1150°C and 1200°C plays a positive role in this study. However, fast heating rate may not always bring positive effect to annealing twin boundary formation, since the increase of heating rate may not lead to the increase of local thermal stresses. This is due to the combination of the poor thermal conductivity and the skin effect during induction heating. Thus, the primary hypothesis, which

assumes fast heating rate will lead to high annealing twin density, is only correct at relatively lower temperatures where grain coarsening is restricted, with a heating rate no higher than 200°C/s.

6.0 Conclusions

This study has investigated the behavior of annealing twin boundaries formation and their area density evolution via induction rapid heating of SLM fabricated 316L stainless steel components. The processing parameters, i.e. reheating temperature, heating rate and holding time, are the major factors determining the annealing twin density and the change of microstructure. Based on the results presented before, several conclusions can be drawn:

1. The SS316L samples heat treated via induction rapid heating system at 1150°C showed faster recrystallization kinetics, similar microstructure, comparable annealing twin density, finer grain size and higher microhardness values than the samples processed using conventional heat treatments with low heating rate at the same reheating temperature. This comparison proves the feasibility of induction rapid heating process to control the grain size and improve the annealing twin density on SLM fabricated 316L stainless steel samples. The benefit of induction rapid heating process is the ability to achieve similar microstructure with comparable annealing twin density and finer grain size at shorter processing times.

2. The annealing twin boundaries form during recrystallization. The mechanism of annealing twin boundaries formation of SLM fabricated SS316L during induction rapid heating is a combination of growth accident and grain boundary dissociation. For growth accident, the grain boundaries was observed to migrate to local strained zones and the annealing twin boundaries formed as a result of the formation of stacking faults during this boundary migration. For grain boundary dissociation, some high energy grain boundaries were observed to decompose into a coherent twin boundary and an incoherent twin boundary, and this decreased the total energy of the system. Growth accident is the dominant mechanism of the formation of annealing twin

boundaries based on the observation of microstructure via EBSD analysis. Gleiter's model and Pande's model were applied to check the annealing twin density behavior. Gleiter's model does not fit with the experimental data. Pande's model shows good fitting with experimental data at low reheating temperatures where the grain growth is restricted, and fails to properly predict as temperature increases due to grain coarsening.

3. The annealing twin density is significantly related to the recrystallization fraction and the processing conditions. The reheating temperature and heating rate are related to the annealing twin density by influencing the recrystallization rate. The recrystallization rate increases as the reheating temperature increases. At a higher reheating temperature, it takes much less time to achieve similar recrystallization fraction and annealing twin density than that at a lower reheating temperature. Based on the results from the experiments, a faster heating rate (within the range 0-200°C/s) also leads to a faster recrystallization rate, and therefore a higher annealing twin density at the same reheating temperature before grain coarsening occurs. In this study, several optimum processing conditions with high annealing twin density and high microhardness were found: reheating at 1150°C and holding for 48min with a heating rate of 200°C/s, reheating at 1200°C and holding for 12min with a heating rate of 200°C/s, reheating at 1250°C and holding for 6min with a heating rate of 200°C/s.

4. The increase of annealing twin density first increases and then decreases as the recrystallization rate increases. The increase at the beginning is due to the increase in the nucleation rate with a limited growth rate. This promotes the formation of stacking faults during grain boundary migration in early recrystallization. The following decrease is a result of much faster growth rate, which leads to grain coarsening and the consumption of formed annealing twin boundaries. It means that the increase of recrystallization rate may lead to an increase in annealing

twin density, but the marginal benefit actually decreases. The optimum n value of recrystallization kinetics is in the approximate range of 2.5-3.5.

5. Based on the understanding of annealing twin boundaries formation mechanism, the local strained areas promote the formation of annealing twin boundaries. This is the result of local thermal stresses due to the skin effect during induction rapid heating. The local thermal stresses are related to the heating rate, reheating temperature and the properties of the material. Based on theoretical calculations of the thermal stresses, the increase of heating rate may not always lead to an increase of thermal stress. Thus, the effect of heating rate is complex, since the heating rate relates to both the local thermal stresses and the recrystallization rate. In this study, the increase of heating rate results in an increase in annealing twin density within a 0-200°C/s range. However, continuous increases in the heating rate may not produce a continuous increase in the annealing twin density. The poor thermal conductivity of 316L stainless steel increases the thermal stress by increasing the temperature difference between the surface and the center due to skin effect.

7.0 Future Works

This study has investigated the feasibility of induction rapid heating process to modify the initial microstructure of 316L stainless steel after SLM fabrication. The formation of annealing twin boundaries was discussed. The relationship between annealing twin density and important processing parameters, i.e. reheating temperature, heating rate and holding time, was studied. The effect of heating rate was further analyzed. For future directions, there are several suggestions:

1. The samples used in this study were from the same set of SLM processing, which means the initial condition of the as-fabricated samples are the same. However, the level of initial strain after SLM fabrication may also influence the annealing twin density behavior. Thus, the influence of initial strain of as-fabricated sample and the relationship between the SLM processing parameters and the annealing twin density response during the post heat treatments need further study.

2. To simplify the investigation in this study, the samples applied in this study have the same simple geometry and the applied coil during induction rapid heating is the same. However, in real additive manufacturing, the fabricated components are expected to have complex shapes. Thus, the design of induction coil to achieve best current distribution and therefore the optimum heating rate is also important and needs further investigation.

Bibliography

- [1] T. DebRoy, H. Wei, J. Zuback, T. Mukherjee, J. Elmer, J. Milewski, A.M. Beese, A. Wilson-Heid, A. De, W. Zhang, Additive manufacturing of metallic components—process, structure and properties, *Progress in Materials Science* 92 (2018) 112-224.
- [2] A. Standard, F2792, Standard terminology for additive manufacturing technologies', ASTM F2792-12a (2012).
- [3] J.J. Dunkley, Metal Powder Atomisation Methods for Modern Manufacturing, *Johnson Matthey Technology Review* 63(3) (2019) 226-232.
- [4] R.M. German, Powder metallurgy of iron and steel, John! Wiley & Sons, Inc, 605 Third Ave, New York, NY 10016, USA, 1998. 496 (1998).
- [5] E. Klar, P.K. Samal, Powder metallurgy stainless steels: processing, microstructures, and properties, ASM international 2007.
- [6] P. Suri, R.P. Koseski, R.M. German, Microstructural evolution of injection molded gas-and water-atomized 316L stainless steel powder during sintering, *Materials Science and Engineering: A* 402(1-2) (2005) 341-348.
- [7] P.K. Gokuldoss, S. Kolla, J. Eckert, Additive manufacturing processes: Selective laser melting, electron beam melting and binder jetting—Selection guidelines, *Materials* 10(6) (2017) 672.
- [8] Y. Bai, G. Wagner, C.B. Williams, Effect of particle size distribution on powder packing and sintering in binder jetting additive manufacturing of metals, *Journal of Manufacturing Science and Engineering* 139(8) (2017) 081019.
- [9] H. Miyajiri, N. Momenzadeh, L. Yang, Effect of printing speed on quality of printed parts in Binder Jetting Process, *Additive Manufacturing* 20 (2018) 1-10.
- [10] T. Do, P. Kwon, C.S. Shin, Process development toward full-density stainless steel parts with binder jetting printing, *International Journal of Machine Tools and Manufacture* 121 (2017) 50-60.
- [11] B. Verlee, T. Dormal, J. Lecomte-Beckers, Density and porosity control of sintered 316L stainless steel parts produced by additive manufacturing, *Powder Metallurgy* 55(4) (2012) 260-267.
- [12] P. Nandwana, A.M. Elliott, D. Siddel, A. Merriman, W.H. Peter, S.S. Babu, Powder bed binder jet 3D printing of Inconel 718: Densification, microstructural evolution and challenges ☆, *Current Opinion in Solid State and Materials Science* 21(4) (2017) 207-218.

- [13] D. Hong, D.-T. Chou, O.I. Velikokhatnyi, A. Roy, B. Lee, I. Swink, I. Issaev, H.A. Kuhn, P.N. Kumta, Binder-jetting 3D printing and alloy development of new biodegradable Fe-Mn-Ca/Mg alloys, *Acta biomaterialia* 45 (2016) 375-386.
- [14] M. Doyle, K. Agarwal, W. Sealy, K. Schull, Effect of layer thickness and orientation on mechanical behavior of binder jet stainless steel 420+ bronze parts, *Procedia Manufacturing* 1 (2015) 251-262.
- [15] J. Gonzalez, J. Mireles, Y. Lin, R.B. Wicker, Characterization of ceramic components fabricated using binder jetting additive manufacturing technology, *Ceramics International* 42(9) (2016) 10559-10564.
- [16] L. Rabinskiy, A. Ripetskiy, S. Sitnikov, Y. Solyaev, R. Kahramanov, Fabrication of porous silicon nitride ceramics using binder jetting technology, *IOP Conference Series: Materials Science and Engineering*, IOP Publishing, 2016, p. 012023.
- [17] L.N. Rabinskiy, S.A. Sitnikov, V.A. Pogodin, A.A. Ripetskiy, Y.O. Solyaev, Binder jetting of Si₃N₄ ceramics with different porosity, *Solid State Phenomena*, Trans Tech Publ, 2017, pp. 37-50.
- [18] A.Y. Kumar, Y. Bai, A. Eklund, C.B. Williams, The effects of Hot Isostatic Pressing on parts fabricated by binder jetting additive manufacturing, *Additive Manufacturing* 24 (2018) 115-124.
- [19] E. Louvis, P. Fox, C.J. Sutcliffe, Selective laser melting of aluminium components, *Journal of Materials Processing Technology* 211(2) (2011) 275-284.
- [20] D. Buchbinder, H. Schleifenbaum, S. Heidrich, W. Meiners, J. Bültmann, High power selective laser melting (HP SLM) of aluminum parts, *Physics Procedia* 12 (2011) 271-278.
- [21] K. Guan, Z. Wang, M. Gao, X. Li, X. Zeng, Effects of processing parameters on tensile properties of selective laser melted 304 stainless steel, *Materials & Design* 50 (2013) 581-586.
- [22] K. Kempen, E. Yasa, L. Thijs, J.-P. Kruth, J. Van Humbeeck, Microstructure and mechanical properties of Selective Laser Melted 18Ni-300 steel, *Physics Procedia* 12 (2011) 255-263.
- [23] L. Thijs, F. Verhaeghe, T. Craeghs, J. Van Humbeeck, J.-P. Kruth, A study of the microstructural evolution during selective laser melting of Ti-6Al-4V, *Acta materialia* 58(9) (2010) 3303-3312.
- [24] W. Xu, M. Brandt, S. Sun, J. Elambasseril, Q. Liu, K. Latham, K. Xia, M. Qian, Additive manufacturing of strong and ductile Ti-6Al-4V by selective laser melting via in situ martensite decomposition, *Acta Materialia* 85 (2015) 74-84.

- [25] K. Amato, S. Gaytan, L. Murr, E. Martinez, P. Shindo, J. Hernandez, S. Collins, F. Medina, Microstructures and mechanical behavior of Inconel 718 fabricated by selective laser melting, *Acta Materialia* 60(5) (2012) 2229-2239.
- [26] S. Li, Q. Wei, Y. Shi, Z. Zhu, D. Zhang, Microstructure characteristics of Inconel 625 superalloy manufactured by selective laser melting, *Journal of Materials Science & Technology* 31(9) (2015) 946-952.
- [27] S.M. Yusuf, N. Gao, Influence of energy density on metallurgy and properties in metal additive manufacturing, *Materials Science and Technology* 33(11) (2017) 1269-1289.
- [28] M. Shiomi, K. Osakada, K. Nakamura, T. Yamashita, F. Abe, Residual stress within metallic model made by selective laser melting process, *CIRP Annals* 53(1) (2004) 195-198.
- [29] Y. Liu, Y. Yang, D. Wang, A study on the residual stress during selective laser melting (SLM) of metallic powder, *The International Journal of Advanced Manufacturing Technology* 87(1-4) (2016) 647-656.
- [30] I. Yadroitsev, I. Yadroitsava, Evaluation of residual stress in stainless steel 316L and Ti6Al4V samples produced by selective laser melting, *Virtual and Physical Prototyping* 10(2) (2015) 67-76.
- [31] J.-P. Kruth, J. Deckers, E. Yasa, R. Wauthlé, Assessing and comparing influencing factors of residual stresses in selective laser melting using a novel analysis method, *Proceedings of the institution of mechanical engineers, Part B: Journal of Engineering Manufacture* 226(6) (2012) 980-991.
- [32] C. Casavola, S. Campanelli, C. Pappalettere, Experimental analysis of residual stresses in the selective laser melting process, *Proceedings of the XIth International Congress and Exposition, Orlando, Florida, USA, 2008*.
- [33] C. Casavola, S. Campanelli, C. Pappalettere, Preliminary investigation on distribution of residual stress generated by the selective laser melting process, *The Journal of Strain Analysis for Engineering Design* 44(1) (2009) 93-104.
- [34] I. Yadroitsava, S. Grewar, D. Hattingh, I. Yadroitsev, Residual stress in SLM Ti6Al4V alloy specimens, *Materials Science Forum, Trans Tech Publ, 2015*, pp. 305-310.
- [35] W.M. Tucho, V.H. Lysne, H. Austbø, A. Sjolyst-Kverneland, V. Hansen, Investigation of effects of process parameters on microstructure and hardness of SLM manufactured SS316L, *Journal of Alloys and Compounds* 740 (2018) 910-925.
- [36] L. Nastac, J. Valencia, M. Tims, F. Dax, Advances in the Solidification of IN718 and RS5 Alloys, *Superalloys 718 (2001)* 625-706.

- [37] W.J. Sames, F. List, S. Pannala, R.R. Dehoff, S.S. Babu, The metallurgy and processing science of metal additive manufacturing, *International Materials Reviews* 61(5) (2016) 315-360.
- [38] K. Prashanth, J. Eckert, Formation of metastable cellular microstructures in selective laser melted alloys, *Journal of Alloys and Compounds* 707 (2017) 27-34.
- [39] C. Qiu, M. Al Kindi, A.S. Aladawi, I. Al Hatmi, A comprehensive study on microstructure and tensile behaviour of a selectively laser melted stainless steel, *Scientific reports* 8(1) (2018) 7785.
- [40] Y.-D. Im, K.-H. Kim, K.-H. Jung, Y.-K. Lee, K.-H. Song, Anisotropic Mechanical Behavior of Additive Manufactured AISI 316L Steel, *Metallurgical and Materials Transactions A* 50(4) (2019) 2014-2021.
- [41] V. Cain, L. Thijs, J. Van Humbeeck, B. Van Hooreweder, R. Knutsen, Crack propagation and fracture toughness of Ti6Al4V alloy produced by selective laser melting, *Additive Manufacturing* 5 (2015) 68-76.
- [42] H. Rafi, N. Karthik, H. Gong, T.L. Starr, B.E. Stucker, Microstructures and mechanical properties of Ti6Al4V parts fabricated by selective laser melting and electron beam melting, *Journal of materials engineering and performance* 22(12) (2013) 3872-3883.
- [43] T. Vilaro, C. Colin, J.-D. Bartout, As-fabricated and heat-treated microstructures of the Ti-6Al-4V alloy processed by selective laser melting, *Metallurgical and materials transactions A* 42(10) (2011) 3190-3199.
- [44] J. Strößner, M. Terock, U. Glatzel, Mechanical and Microstructural Investigation of Nickel-Based Superalloy IN718 Manufactured by Selective Laser Melting (SLM), *Advanced Engineering Materials* 17(8) (2015) 1099-1105.
- [45] I. Rosenthal, A. Stern, N. Frage, Microstructure and mechanical properties of AlSi10Mg parts produced by the laser beam additive manufacturing (AM) technology, *Metallography, Microstructure, and Analysis* 3(6) (2014) 448-453.
- [46] M. Shamsujjoha, S.R. Agnew, J.M. Fitz-Gerald, W.R. Moore, T.A. Newman, High Strength and Ductility of Additively Manufactured 316L Stainless Steel Explained, *Metallurgical and Materials Transactions A* 49(7) (2018) 3011-3027.
- [47] C. Herrera, R.L. Plaut, A.F. Padilha, Microstructural refinement during annealing of plastically deformed austenitic stainless steels, *Materials Science Forum*, Trans Tech Publ, 2007, pp. 423-428.
- [48] F. Yan, W. Xiong, E. Faierson, Grain structure control of additively manufactured metallic materials, *Materials* 10(11) (2017) 1260.

- [49] K. Saeidi, X. Gao, F. Lofaj, L. Kvetková, Z.J. Shen, Transformation of austenite to duplex austenite-ferrite assembly in annealed stainless steel 316L consolidated by laser melting, *Journal of Alloys and Compounds* 633 (2015) 463-469.
- [50] L. Priester, *Grain boundaries: from theory to engineering*, Springer Science & Business Media 2012.
- [51] W.T. Read, W. Shockley, Dislocation models of crystal grain boundaries, *Physical review* 78(3) (1950) 275.
- [52] D. Wolf, A Read-Shockley model for high-angle grain boundaries, *Scripta metallurgica* 23(10) (1989) 1713-1718.
- [53] A.P. Sutton, R.W. Balluffi, A. Sutton, *Interfaces in crystalline materials*, (1995).
- [54] W. Bollmann, *Crystal Defects and crystalline interfaces* [9] HIRTH, J. P., BALLUFFI, R. W, *Acta Metall* 21 (1973) 929.
- [55] H. Grimmer, W.t. Bollmann, D. Warrington, Coincidence-site lattices and complete pattern-shift in cubic crystals, *Acta Crystallographica Section A: Crystal Physics, Diffraction, Theoretical and General Crystallography* 30(2) (1974) 197-207.
- [56] W. Bollmann, *Crystal lattices, interfaces, matrices: an extension of crystallography*, Bollmann 1982.
- [57] A. Hu, *The Nature and Behavior of Grain Boundaries: A Symposium Held at the TMS-AIME Fall Meeting in Detroit, Michigan, October 18–19, 1971*, Springer Science & Business Media 2012.
- [58] H.C.H. Carpenter, S. Tamura, Experiments on the production of large copper crystals, *Proceedings of the Royal Society of London. Series A, Containing Papers of a Mathematical and Physical Character* 113(763) (1926) 28-43.
- [59] T. Blewitt, R. Coltman, J. Redman, Low-temperature deformation of copper single crystals, *Journal of Applied Physics* 28(6) (1957) 651-660.
- [60] J. Venables, Deformation twinning in face-centred cubic metals, *Philosophical magazine* 6(63) (1961) 379-396.
- [61] S. Mahajan, G. Chin, Formation of deformation twins in fcc crystals, *Acta metallurgica* 21(10) (1973) 1353-1363.
- [62] R. Armstrong, R. Reed-Hill, J. Hirth, H. Rogers, *Deformation Twinning*, by RE Reed-Hill, JP Hirth and HC Rogers (1964) 356.
- [63] M. Niewczas, G. Saada, A physics of condensed matter structure defects and mechanical properties, *Philos. Mag. A* 82 (2002) 167-191.

- [64] K. Lagerlöf, J. Castaing, P. Pirouz, A. Heuer, Nucleation and growth of deformation twins: a perspective based on the double-cross-slip mechanism of deformation twinning, *Philosophical Magazine A* 82(15) (2002) 2841-2854.
- [65] T.-H. Lee, C.-S. Oh, S.-J. Kim, S. Takaki, Deformation twinning in high-nitrogen austenitic stainless steel, *Acta materialia* 55(11) (2007) 3649-3662.
- [66] P. Gu, M. Dao, Y. Zhu, Strengthening at nanoscaled coherent twin boundary in fcc metals, *Philosophical Magazine* 94(11) (2014) 1249-1262.
- [67] J. Wang, Z. Zeng, C.R. Weinberger, Z. Zhang, T. Zhu, S.X. Mao, In situ atomic-scale observation of twinning-dominated deformation in nanoscale body-centred cubic tungsten, *Nature materials* 14(6) (2015) 594.
- [68] S.-H. Joo, H. Kato, M. Jang, J. Moon, C. Tsai, J. Yeh, H. Kim, Tensile deformation behavior and deformation twinning of an equimolar CoCrFeMnNi high-entropy alloy, *Materials Science and Engineering: A* 689 (2017) 122-133.
- [69] S. Mandal, P. Sivaprasad, B. Raj, V.S. Sarma, Grain boundary microstructural control through thermomechanical processing in a titanium-modified austenitic stainless steel, *Metallurgical and Materials Transactions A* 39(13) (2008) 3298-3307.
- [70] S. Sinha, D.-I. Kim, E. Fleury, S. Suwas, Effect of grain boundary engineering on the microstructure and mechanical properties of copper containing austenitic stainless steel, *Materials Science and Engineering: A* 626 (2015) 175-185.
- [71] H. Gleiter, The formation of annealing twins, *Acta metallurgica* 17(12) (1969) 1421-1428.
- [72] M.A. Meyers, L.E. Murr, A model for the formation of annealing twins in FCC metals and alloys, *Acta metallurgica* 26(6) (1978) 951-962.
- [73] S. Mahajan, C. Pande, M. Imam, B. Rath, Formation of annealing twins in fcc crystals, *Acta materialia* 45(6) (1997) 2633-2638.
- [74] C. Pande, M. Imam, B. Rath, Study of annealing twins in FCC metals and alloys, *Metallurgical transactions A* 21(11) (1990) 2891-2896.
- [75] R. Fullman, J. Fisher, Formation of annealing twins during grain growth, *Journal of Applied Physics* 22(11) (1951) 1350-1355.
- [76] V. Randle, P. Rios, Y. Hu, Grain growth and twinning in nickel, *Scripta Materialia* 58(2) (2008) 130-133.
- [77] K.-H. Song, Y.B. Chun, S.-K. Hwang, Direct observation of annealing twin formation in a Pb-base alloy, *Materials Science and Engineering: A* 454 (2007) 629-636.

- [78] S. Mandal, A. Bhaduri, V.S. Sarma, Studies on twinning and grain boundary character distribution during anomalous grain growth in a Ti-modified austenitic stainless steel, *Materials Science and Engineering: A* 515(1-2) (2009) 134-140.
- [79] Y. Jin, B. Lin, M. Bernacki, G.S. Rohrer, A. Rollett, N. Bozzolo, Annealing twin development during recrystallization and grain growth in pure nickel, *Materials Science and Engineering: A* 597 (2014) 295-303.
- [80] B. Lin, Y. Jin, C.M. Hefferan, S.F. Li, J. Lind, R.M. Suter, M. Bernacki, N. Bozzolo, A.D. Rollett, G.S. Rohrer, Observation of annealing twin nucleation at triple lines in nickel during grain growth, *Acta Materialia* 99 (2015) 63-68.
- [81] J. Simmons, Overview: high-nitrogen alloying of stainless steels, *Materials Science and Engineering: A* 207(2) (1996) 159-169.
- [82] S. Wang, K. Yang, Y. Shan, L. Li, Plastic deformation and fracture behaviors of nitrogen-alloyed austenitic stainless steels, *Materials Science and Engineering: A* 490(1-2) (2008) 95-104.
- [83] Y.S. Han, S.H. Hong, The effect of Al on mechanical properties and microstructures of Fe-32Mn-12Cr-xAl-0.4 C cryogenic alloys, *Materials Science and Engineering: A* 222(1) (1997) 76-83.
- [84] B. Huang, X. Wang, L. Wang, Y. Rong, Effect of nitrogen on stacking fault formation probability and mechanical properties of twinning-induced plasticity steels, *Metallurgical and Materials Transactions A* 39(4) (2008) 717-724.
- [85] D. Douglass, G. Thomas, W. Roser, Ordering, stacking faults and stress corrosion cracking in austenitic alloys, *Corrosion* 20(1) (1964) 15t-28t.
- [86] P. Brofman, G. Ansell, On the effect of carbon on the stacking fault energy of austenitic stainless steels, *Metallurgical and Materials Transactions A* 9(6) (1978) 879-880.
- [87] Q. Dai, X. Cheng, X. Luo, Y. Zhao, Structural parameters of the martensite transformation for austenitic steels, *Materials characterization* 49(4) (2002) 367-371.
- [88] R. Schramm, R. Reed, Stacking fault energies of seven commercial austenitic stainless steels, *Metallurgical Transactions A* 6(7) (1975) 1345.
- [89] C.G. Rhodes, A.W. Thompson, The composition dependence of stacking fault energy in austenitic stainless steels, *Metallurgical Transactions A* 8(12) (1977) 1901-1906.
- [90] F. Pickering, In *Stainless Steels*, GL Dunlop (London, UK: The Institute of Metals, 1985) (1985) 12.

- [91] B. Vynokur, Influence of alloying on the free energy of austenitic grain boundaries in steel, *Materials Science* 32(2) (1996) 144-157.
- [92] A. Norma, E92-82 (1997) E3 Standard Test Method for Vickers Hardness of Metallic Materials, Philadelphia (EE. UU.): American Society for Testing and Materials (1997).
- [93] A. Simchi, H. Pohl, Effects of laser sintering processing parameters on the microstructure and densification of iron powder, *Materials Science and Engineering: A* 359(1-2) (2003) 119-128.
- [94] X. Chen, J. Li, X. Cheng, H. Wang, Z. Huang, Effect of heat treatment on microstructure, mechanical and corrosion properties of austenitic stainless steel 316L using arc additive manufacturing, *Materials Science and Engineering: A* 715 (2018) 307-314.
- [95] J. Yan, Y. Zhou, R. Gu, X. Zhang, W.-M. Quach, M. Yan, A Comprehensive Study of Steel Powders (316L, H13, P20 and 18Ni300) for Their Selective Laser Melting Additive Manufacturing, *Metals* 9(1) (2019) 86.
- [96] K. Saeidi, Stainless steels fabricated by laser melting: Scaled-down structural hierarchies and microstructural heterogeneities, Department of Materials and Environmental Chemistry (MMK), Stockholm University, 2016.
- [97] D. Brandon, The structure of high-angle grain boundaries, *Acta metallurgica* 14(11) (1966) 1479-1484.
- [98] V. Randle, A methodology for grain boundary plane assessment by single-section trace analysis, *Scripta materialia* 44(12) (2001) 2789-2794.
- [99] A. Hadadzadeh, F. Mokdad, M. Wells, D. Chen, A new grain orientation spread approach to analyze the dynamic recrystallization behavior of a cast-homogenized Mg-Zn-Zr alloy using electron backscattered diffraction, *Materials Science and Engineering: A* 709 (2018) 285-289.
- [100] S. Mandal, A. Bhaduri, V.S. Sarma, A study on microstructural evolution and dynamic recrystallization during isothermal deformation of a Ti-modified austenitic stainless steel, *Metallurgical and Materials Transactions A* 42(4) (2011) 1062-1072.
- [101] W.F. Smith, J. Hashemi, F. Presuel-Moreno, *Foundations of materials science and engineering*, McGraw-Hill Publishing 2006.
- [102] B. Lin, Investigating annealing twin formation mechanisms in face-centered cubic nickel, Carnegie Mellon University, 2015.
- [103] D. Field, P. Trivedi, S. Wright, M. Kumar, Analysis of local orientation gradients in deformed single crystals, *Ultramicroscopy* 103(1) (2005) 33-39.
- [104] A.C. Leff, Dislocation Density Effects on Annealing Twin Nucleation and Recrystallization Mechanism Activation, Drexel University 2017.

- [105] W. Wang, S. Lartigue-Korinek, F. Brisset, A. Helbert, J. Bourgon, T. Baudin, Formation of annealing twins during primary recrystallization of two low stacking fault energy Ni-based alloys, *Journal of materials science* 50(5) (2015) 2167-2177.
- [106] J. Brons, G. Thompson, A comparison of grain boundary evolution during grain growth in fcc metals, *Acta materialia* 61(11) (2013) 3936-3944.
- [107] X. Fang, K. Zhang, H. Guo, W. Wang, B. Zhou, Twin-induced grain boundary engineering in 304 stainless steel, *Materials Science and Engineering: A* 487(1-2) (2008) 7-13.
- [108] X. Fang, W. Wang, Z. Cai, C. Qin, B. Zhou, The evolution of cluster of grains with $\sum 3n$ relationship in austenitic stainless steel, *Materials science and engineering: a* 527(6) (2010) 1571-1576.
- [109] J. Bair, S. Hatch, D. Field, Formation of annealing twin boundaries in nickel, *Scripta Materialia* 81 (2014) 52-55.
- [110] E.E. Underwood, *Quantitative stereology*, Reading, MA (1970) 5.
- [111] W. Charnock, J. Nutting, The effect of carbon and nickel upon the stacking-fault energy of iron, *Metal Science Journal* 1(1) (1967) 123-127.
- [112] R.A. Varin, Grain boundary diffusion and free energy during the recrystallization of type 316 stainless steel, *Materials Science and Engineering* 66(1) (1984) 97-105.
- [113] C.M. Barr, G.A. Vetterick, K.A. Unocic, K. Hattar, X.-M. Bai, M.L. Taheri, Anisotropic radiation-induced segregation in 316L austenitic stainless steel with grain boundary character, *Acta Materialia* 67 (2014) 145-155.
- [114] T. Xi, M.B. Shahzad, D. Xu, Z. Sun, J. Zhao, C. Yang, M. Qi, K. Yang, Effect of copper addition on mechanical properties, corrosion resistance and antibacterial property of 316L stainless steel, *Materials Science and Engineering: C* 71 (2017) 1079-1085.
- [115] J. Cahoon, Q. Li, N. Richards, Microstructural and processing factors influencing the formation of annealing twins, *Materials science and engineering: a* 526(1-2) (2009) 56-61.
- [116] B.R. Kumar, B. Mahato, N. Bandyopadhyay, D.K. Bhattacharya, Comparison of rolling texture in low and medium stacking fault energy austenitic stainless steels, *Materials Science and Engineering: A* 394(1-2) (2005) 296-301.
- [117] A.N. Kolmogorov, A. Kolmogorov, *A statistical theory for the recrystallization of metals*, (1937).
- [118] B. Johnson, R. Mehl, *Trans, AIME*, 1939, p. 416.

- [119] M. Avrami, Kinetics of phase change. I General theory, *The Journal of chemical physics* 7(12) (1939) 1103-1112.
- [120] P. Gordon, R. Vandermeer, Mechanism of boundary migration in recrystallization, *TRANSACTIONS OF THE METALLURGICAL SOCIETY OF AIME* 224(5) (1962) 917-&.
- [121] N. Hansen, T. Leffers, J. Kjems, Recrystallization kinetics in copper investigated by in situ texture measurements by neutron diffraction, *Acta Metallurgica* 29(8) (1981) 1523-1533.
- [122] J. Michalak, W. Hibbard, Effect of rolling procedure on the kinetics of recrystallization of cold-rolled iron, *Trans. ASM* 53 (1961) 331-348.
- [123] A. Rosen, M. Burton, G. Smith, Recrystallization of high-purity iron, *Transactions of the Metallurgical Society of AIME* 230(1) (1964) 205-&.
- [124] J. Davies, P. Simpson, *Induction heating handbook*, McGraw-Hill London 1979.
- [125] N. Wilson, P. Bunch, *Magnetic permeability of stainless steel for use in accelerator beam transport systems*, Los Alamos National Lab., NM (USA), 1991.
- [126] S. Semiatin, *Elements of induction heating: design, control, and applications*, ASM International 1988.
- [127] F. Kreith, W.Z. Black, *Basic heat transfer*, Harper & Row New York 1980.